

**Highly Efficient Domain Wall Motion
in Ferrimagnetic Bi-layer Systems at the
Angular Momentum Compensation Temperature**

Dissertation

zur Erlangung des
Doktorgrades der Naturwissenschaften
(Dr. rer. nat.)

der

Naturwissenschaftlichen Fakultät II
Chemie, Physik und Mathematik

der Martin-Luther-Universität
Halle-Wittenberg

vorgelegt von

Herrn Robin Bläsing
geb. am 09.01.1990 in Haan.

Gutachter:

Prof. Dr. Stuart S. P. Parkin
Prof. Dr. Gernot Güntherodt
Prof. Dr. Jamal Berakdar

Tag der öffentlichen Verteidigung:
20.12.2019

Acknowledgments

I would like to express my deepest appreciation to the supervisor of the present thesis, Prof. Dr. STUART S. P. PARKIN. He has supported my research since my master program, in which I joined his research group at the IBM ALMADEN RESEARCH CENTER in SAN JOSE, CALIFORNIA, USA. I have got to know him as a highly motivated and creatively minded person who spreads his enthusiasm to the whole research community. His extensive knowledge in the field of spintronics and his open manner have been of great value to me.

I am extremely grateful for the continuous mentorship of Prof. Dr. GERNOT GÜNTHERODT. He has supervised my academic career since my undergraduate studies. His unwavering guidance and constructive advice were key for the completion of this thesis.

I would also like to extend my deepest gratitude to Dr. SEE-HUN YANG for his ingenious suggestions and advice in countless discussions. Due to his relentless support since my master thesis, I was able to understand the mechanisms of domain wall motion in the minutest detail. He has been a valuable conversationalist for me and it has always been a joy to talk to him.

Special thanks should also go to TIANPING MA and CHIRAG GARG with those I discussed many results of the experiments related to this thesis. It has been a great pleasure to work with them.

Furthermore, I gratefully acknowledge the effort of DAVID GATZKA, TOM LICHTENBERG and TOBIAS SPENS, who served as interns at the MAX PLANCK INSTITUTE OF MICROSTRUCTURE PHYSICS. I hope to have passed on my knowledge about programming, simulating and performing experiments and enlightened their spark and curiosity for science.

I would like to thank all colleagues and employees of the MAX PLANCK INSTITUTE OF MICROSTRUCTURE PHYSICS who gave me practical suggestions for experiments or theoretical models or who provided me assistance with administrative tasks.

Last but not least, I am deeply indebted to my girlfriend JENNIFER DI GANGI and my parents. They played a decisive role by providing me with encouragement and patience throughout the entire duration of my studies.

Zusammenfassung

Im letzten Jahrzehnt wurde die Effizienz strominduzierter Bewegung magnetischer Domänenwände (DWs) enorm gesteigert, indem in synthetischen Antiferromagneten der Drehmomentübertrag durch die antiferromagnetische Wechselwirkung (ECT) genutzt wurde. In dieser Arbeit wird der ECT in einer ferrimagnetischen Doppelschicht untersucht, in der die magnetischen Momente einer Co und einer Gd-Schicht ebenfalls antiferromagnetisch koppeln. Die DWs werden durch nanosekundenlange Strompulse bewegt und deren Geschwindigkeit mittels KERR-Mikroskopie bei verschiedenen Temperaturen ermittelt. In der Co/Gd-Doppelschicht bewegen sich die DWs bereits bei einem sehr geringen Schwellstrom. Die Bewegung ist bei einer Temperatur T_A am effizientesten, bei der sich die Drehimpulse der beiden Schichten kompensieren. Die Berücksichtigung der JOULSCHEN Wärme ist bei der Bestimmung von T_A von besonderer Wichtigkeit. Die hier gewonnenen Erkenntnisse zur Entwicklung neuartige Speichermedien genutzt werden.

Abstract

Within the last decade, the efficiency of current-induced motion of magnetic domain walls (DWs) has been enhanced tremendously by utilizing the exchange coupling torque (ECT) in synthetic antiferromagnetic structures. In the present study this ECT mechanism is explored in a ferrimagnetic bi-layers consisting of a Co and a Gd layer which couple antiferromagnetically. The DWs are moved by nanosecond-long current pulses and their velocity is determined by using KERR microscopy at various temperatures. Only a low threshold current density is required to move DWs in this Co/Gd bi-layer. It is shown that the motion is most efficient at a certain temperature T_A at which the angular momenta of both layers compensate each other. Since the device temperature is significantly increased by the current pulses, taking into account JOULE heating is of major importance when determining T_A . The results of this thesis can be used for the development of novel storage devices and improving their efficiency.

Contents

1. Introduction	1
2. Theoretical foundations	5
2.1. Ferromagnetism in thin films	5
2.1.1. HEISENBERG exchange model	5
2.1.2. LANDÉ g-factor	6
2.1.3. Saturation magnetization and CURIE temperature	7
2.1.4. Magnetic anisotropy	8
2.1.4.1. Magnetocrystalline anisotropy	9
2.1.4.2. Shape anisotropy	10
2.1.4.3. Effective anisotropy	11
2.1.5. Magnetic multilayers	11
2.1.5.1. RUDERMAN–KITTEL–KASUYA–YOSIDA interaction	12
2.1.5.2. Magnetic moment and angular momentum compensation	12
2.2. Domain walls in ferrimagnetic bi-layers	13
2.2.1. One-dimensional model	14
2.2.2. Domain wall profile	15
2.2.3. Domain wall energy density	16
2.2.3.1. Intra-layer exchange energy density	17
2.2.3.2. Anisotropy energy density	17
2.2.3.3. DZVALOSHINSKII-MORIYA interaction	18
2.2.3.4. Exchange-coupled domain walls	20
2.2.3.5. Total domain wall energy of antiferromagnetic bi-layer	21
2.2.4. Domain wall width	22
2.3. Domain wall dynamics in ferrimagnetic bi-layer	23
2.3.1. LANDAU–LIFSHITZ–GILBERT equation	23
2.3.2. RAYLEIGH–LAGRANGE equation	24
2.3.3. Static solutions for ferrimagnetic bi-layer	26
2.3.3.1. Total angular momentum	27
2.3.3.2. Steady state motion	27
2.3.4. Field-driven domain wall motion	28
2.3.5. Current-induced domain wall motion	30
2.3.5.1. Spin transfer torque	30
2.3.5.2. Spin HALL effect	33
2.3.5.3. Dynamic solutions	35
2.3.5.4. Domain wall mobility	36

2.3.6.	Exchange coupling torque	37
2.3.7.	Influence of H_x on current-induced domain wall motion	39
2.3.7.1.	Upper and lower bound for H_x independence	40
2.3.7.2.	Optimal ratio A^U/A^L for H_x independence	42
2.3.8.	Dry friction	44
2.3.8.1.	Threshold field	46
2.3.8.2.	Threshold current	46
2.3.8.3.	Motion efficiency	47
3.	Experimental setup and methods	49
3.1.	Sample preparation	49
3.1.1.	Sputtering	49
3.1.2.	Lithography	50
3.2.	Measurement of domain wall motion	50
3.2.1.	Differential KERR microscopy	51
3.2.2.	Experimental setup	53
3.2.3.	Method to determine domain wall velocity	53
3.2.4.	Method to determine JOULE heating	55
3.3.	Additional measurement methods	57
3.3.1.	Threshold field	57
3.3.2.	SQUID magnetometer	57
3.3.3.	XMCD	58
4.	Results	59
4.1.	Ferromagnetic thin film	59
4.1.1.	Temperature dependence of magnetization	59
4.1.2.	Temperature dependence of current-induced domain wall motion	60
4.1.3.	Temperature dependence of threshold current	61
4.2.	Synthetic antiferromagnet	64
4.2.1.	Temperature dependence of current-induced domain wall motion	64
4.2.2.	Temperature dependence of threshold current	64
4.2.3.	Influence of temperature on H_x dependence of current-induced domain wall motion	66
4.3.	Ferrimagnetic Co/Gd bi-layer	66
4.3.1.	Temperature dependence of magnetic properties	67
4.3.2.	Influence of temperature on H_x dependence of current-induced domain wall motion	69
4.3.3.	JOULE heating	71
4.3.4.	Temperature dependence of current-induced domain wall motion	72
4.3.5.	Temperature dependence of threshold current density	74

5. Discussion	77
5.1. Determination of T_M and T_A	77
5.1.1. Field-driven domain wall motion	77
5.1.1.1. Temperature dependence of threshold field	78
5.1.1.2. Temperature dependence of WALKER breakdown	78
5.1.2. H_x dependence of current-induced domain wall motion	79
5.1.2.1. Temperature dependence of DZHALOSHINSKII-MORIYA interaction field in ferrimagnetic bi-layer	79
5.1.2.2. Temperature dependence of slope	80
5.2. JOULE heating	81
5.3. Dependence of threshold current density on temperature	83
5.3.1. Comparison of threshold current in studied samples	83
5.3.2. Origin of threshold current	84
5.3.2.1. Dry friction model	85
5.3.2.2. Current pulse length dependence	86
5.4. Dependence of domain wall mobility on temperature	87
5.4.1. Comparison of SAF and ferromagnetic Co/Ni/Co structure	87
5.4.2. Ferrimagnetic Co/Gd bi-layer	90
5.5. Exchange coupling torque	91
5.5.1. Torque contributions to domain wall velocity	91
5.5.2. Maximum domain wall velocity at angular momentum compensation temperature at high current densities	92
6. Conclusion and outlook	95
Bibliography	97
Appendix	109
A. Mathematical supplement	109
A.1. Properties of domain wall profile	109
A.2. Effective quantities approach	110
A.3. Tilting of DW in ferrimagnetic bi-layer	111
B. Modeling of JOULE heating	114
B.1. Numerical modeling of Joule heating in racetrack	114
B.2. DW dynamics for time-varying moments	116
C. Supplementary figures	118
C.1. Micromagnetic simulations	118
C.2. Ferromagnetic Co/Ni/Co structure	120
C.3. SAF structure	121
C.4. Ferrimagnetic Co/Gd bi-layer	123

List of Figures

1.1. Sketch of racetrack memory	1
2.1. Orientation of magnetization in thin film	10
2.2. Domain wall profile and coordinate system	14
2.3. NÉEL and BLOCH domain wall	15
2.4. Domain wall in antiferromagnetically coupled bi-layer	16
2.5. Energy contributions to domain wall energy of upper and lower magnetic layer	17
2.6. Illustration of DZYALOSHINSKII-MORIYA interaction	19
2.7. Chirality conservation of successive domain walls by DZYALOSHINSKII-MORIYA interaction	20
2.8. Exchange-coupled domain wall in Co/Gd bi-layer	21
2.9. Illustration of spin transfer torque driven domain wall motion	31
2.10. Spin HALL effect creating torque in magnetic moments in bi-layer	34
2.11. Illustration of exchange coupling torque	38
2.12. Illustration of torque created by H_x in ferrimagnetic bi-layer	41
3.1. Sample after sputtering and lithography	51
3.2. Exemplary KERR microscope image of magnetic domain inside nanowire	52
3.3. Exemplary differential KERR microscopy images	52
3.4. Image of experimental setup	54
3.5. Sketch of experimental setup close to sample	55
4.1. Temperature dependence of magnetic properties of ferromagnetic thin film	60
4.2. Temperature dependence of resistance of ferromagnetic device	61
4.3. Domain wall velocity dependence on current density at various temperatures in ferromagnetic structure	62
4.4. Domain wall velocity dependence on temperature at various current densities in ferromagnetic structure	63
4.5. Temperature dependence of threshold current in ferromagnetic structure	63
4.6. Domain wall velocity dependence on current density at various temperatures in SAF structure	65
4.7. Temperature dependence of threshold current at various pulse lengths in SAF structure	65
4.8. Influence of temperature on H_x dependence of domain wall velocity in SAF structure	66
4.9. Coercive field and change of magnetic moments in Co and Gd layer with temperature measured by XMCD	67

List of Figures

4.10. Threshold field as a function of temperature in ferrimagnetic Co/Gd bi-layer . . .	68
4.11. Influence of H_x on current-induced domain wall motion at various temperatures in ferrimagnetic Co/Gd bi-layer	70
4.12. Slope of DW velocity dependence on H_x as a function of temperature of ferrimagnetic Co/Gd bi-layer	72
4.13. Cryostat temperatures at which no H_x dependence exists as a function of current density of ferrimagnetic Co/Gd bi-layer	73
4.14. Domain wall velocity dependence on device temperature for various current densities in ferrimagnetic Co/Gd bi-layer	74
4.15. Temperature dependence of threshold current density of ferrimagnetic Co/Gd bi-layer	75
5.1. Analytical results of torque contributions to DW velocity depending on H_x . . .	80
5.2. JOULE heating as a function of applied current density for 10, 20, 40, and 100 ns-long pulses	82
5.3. Comparison of threshold current density for ferromagnetic layer, SAF and ferrimagnetic bi-layer structure	84
5.4. Scaling of threshold current compared with temperature dependence of magnetization and magnetocrystalline surface anisotropy	86
5.5. Domain wall mobility as a function of temperature	88
5.6. Mobility of DW in ferrimagnetic bi-layer	90
5.7. Contributions to total domain wall velocity by CST and ECT as a function of $m^{\text{Gd}}/m^{\text{Co}}$	92
5.8. Analytic model results of domain wall velocity as a function of $m^{\text{Gd}}/m^{\text{Co}}$	93
B.1. COMSOL simulations of JOULE heating in nanowire	115
C.1. Micromagnetic simulations by LLG SIMULATOR of velocity dependence on H_x in ferrimagnetic bi-layer	118
C.2. Micromagnetic simulations by LLG SIMULATOR modeling magnetic pinning defects in ferromagnetic layer	119
C.3. In-plane hysteresis loops of ferromagnetic Co/Ni/Co sample measured by SQUID	120
C.4. Polar Kerr data of SAF structure at room temperature	121
C.5. Domain wall velocity in SAF structure as a function of current density at various cryostat temperatures	121
C.6. Increase of domain wall velocity with temperature as a function of current density in SAF structure	122
C.7. Asymmetry in XMCD spectrum of Co at L_2 and L_3 edge	123
C.8. Asymmetry in XMCD spectrum of Gd at M_4 and M_5 edge	123
C.9. Temperature dependent hysteresis loops of Gd measured by XMCD	124
C.10. Out-of-plane hysteresis loops of ferrimagnetic Co/Gd sample measured by SQUID	124

C.11. Resistance of device of ferrimagnetic sample 125

C.12. Domain velocity dependence of H_z at magnetic moment compensation
temperature using current pulses 125

C.13. Domain wall velocity in ferrimagnetic Co/Gd bi-layer as a function of current
density at various cryostat temperatures 126

C.14. Temperature at which $\uparrow\downarrow$ and $\downarrow\uparrow$ DWs move with same velocity in curved wire . 127

List of Tables

2.1. Literature values for LANDÉ g-factor	7
2.2. Literature values for saturation magnetization and CURIE temperature	8
4.1. Values used for analytical model of ferrimagnetic Co/Gd bi-layer	71

Acronyms

TM transition metal

HM heavy metal

RE rare earth

SAF synthetic antiferromagnet

DW domain wall

PMA perpendicular magnetic anisotropy

RKKY RUDERMAN-KITTEL-KASUYA-YOSIDA

DMI DZVALOSHINSKII-MORIYA interaction

SHE spin HALL effect

STT spin transfer torque

ECT exchange coupling torque

CST chiral spin torque

FDDWM field-driven domain wall motion

CIDWM current-induced domain wall motion

MOKE magneto-optical KERR effect

XMCD X-ray magnetic circular dichroism

1. Introduction

The need for higher storage density is a ubiquitous challenge in the computer industry of the present time. To date, all mass storage devices are built in a two-dimensional architecture, limiting the storage density significantly. A new kind of three-dimensional storage design has been proposed by STUART PARKIN - the racetrack memory [1, 2]. This device makes use of magnetic domain walls (DWs) as the carriers of information. In contrast to a hard disk drive, the bits shall not be moved by a mechanical rotation but by an electrical current flowing inside a magnetic nanowire. This allows to build U-shaped structures of the nanowires which can bend vertically. Hence, the information can be sent into a third dimension as shown in the sketch in Figure 1.1. This design allows a much higher packing density per feature size compared to existing memory devices and could find application in various memory subsystems in a computer [3].

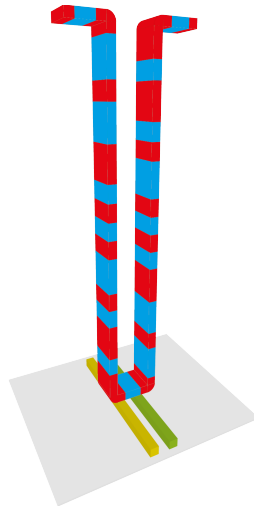


Figure 1.1.: Sketch of racetrack memory. Information is stored in a three-dimensional space by sending magnetic bits vertically using current pulses. Information can be read and written at the bottom of the device. Sketch similar to [2].

The idea of the racetrack memory led to the rise of research focused on current-induced domain wall motion (CIDWM). Earlier studies have already shown that magnetic DWs can be moved by sending an electrical current through the magnetic layer (e.g. [4, 5]). This kind of mechanism became known as the volume spin transfer torque (STT) in which the DWs are moved into electron flow direction. In order to make the racetrack memory more efficient, many research groups have been working on finding better DW driving mechanisms which lead to higher DW velocities. A breakthrough was achieved by using a thin film consisting of a heavy metal (HM) layer (like Pt) adjacent to a transition metal (TM) layer (like Co) in which the magnetic moments exhibit a perpendicular magnetic anisotropy (PMA) [6]. While the DWs in the TM are subject

1. Introduction

to the DZHALOSHINSKII-MORIYA interaction (DMI) which leads to chiral DWs, the electrons in the HM experience a spin HALL effect (SHE) which results in a spin-polarized current flowing perpendicularly into the TM. When the spin current interacts with the magnetic moments in the TM, a so-called chiral spin torque (CST) can move the chiral DWs into current flow direction [7, 8]. A few years later, YANG ET AL. found that an even more efficient driving mechanism than the CST exists in so-called synthetic antiferromagnet (SAF) structures [9]. In these SAF structures, two ferromagnetic layers are exchange-coupled through a spacer layer via the RUDERMAN-KITTEL-KASUYA-YOSIDA (RKKY) interaction [10–12]. This exchange coupling together with the spin HALL current arising from the HM underlayer can create an exchange coupling torque (ECT). The DWs can be moved by the ECT at almost 1000 ms^{-1} [13].

Many recent studies [14–24] focused on CIDWM in ferrimagnetic systems which are also the scope of the study at hand. Ferrimagnetic systems consist of distinct materials, like a TM and a rare earth (RE) metal, with different magnetic properties. There is considerable debate whether the CST or the ECT is the underlying mechanism for driving DWs in these systems.¹ Most studies consider ferrimagnetic systems as a whole and explain the experimental data only by a total magnetization of the system [17–20, 25–27]. Some other studies use an “effective quantity approach” to account for distinct material parameters by merging these into one effective quantity [18, 23, 24]. Although this approach is appropriate in the limit of large exchange coupling, an important drawback is that the underlying mechanisms are concealed. This becomes especially relevant in case of weak exchange coupling like in SAF structures. In these, for example the velocity is largely affected by an H_x field and drops to positive as well as to negative fields [9]. Furthermore, the effect of the so-called chiral drag can only be observed in weakly coupled systems [28].

Through experimental results and supported by a comprehensive analytical model, the present study shows that indeed the ECT is the predominant DW driving mechanism in ferrimagnetic bi-layer systems. A clear distinction between the angular momentum and magnetic moment compensation of the ferrimagnetic bi-layer system is made which is only possible because of the thorough consideration of JOULE heating. This is identified to play a major role considering the current densities in use. It is shown that the ECT is maximized at the angular momentum temperature T_A which leads to highly efficient CIDWM. Moreover, it is demonstrated that there is no DW velocity dependence on H_x at T_A but at the magnetic moment compensation temperature T_M . This finding is of particular interest because recent studies are looking for a DMI field which is measured by H_x dependence and is supposed to diverge at T_M [17–19, 23, 24, 26].

Finally, by investigating three different samples, one ferromagnetic system, one SAF structure, and one ferrimagnetic bi-layer, the temperature dependence of the so-called threshold current density j_{th} is explored. j_{th} is the minimum current density required to move a DW. Since j_{th} is highly temperature-dependent, the thorough analysis yields more insights into the underlying

¹ Also other torque mechanisms like an interface torque have been proposed to explain the enhanced efficiency of DW in ferrimagnets [17].

mechanism resulting in j_{th} . By this, critical parameters for new materials can be identified to reduce j_{th} . In this way, novel storage devices based on CIDWM, like the racetrack memory, can be built with a much lower power consumption.

The thesis is structured as follows. First, the theoretical foundations for CIDWM in ferrimagnetic bi-layers are laid in chapter 2. The experimental setup and methods are explained in chapter 3. Afterwards in chapter 4, the experimental results are shown and compared to the results of the analytical model. Subsequently, the implications of this comparison are deduced in chapter 5. This discussion includes the determination of T_{M} and T_{A} , a quantification of JOULE heating, the temperature dependence of the threshold current, the efficiency of the DW motion at various temperatures and the role of the exchange coupling torque for ferrimagnetic systems. At the end, a conclusion of this study and an outlook for future experiments are provided in chapter 6.

2. Theoretical foundations

The theory of CIDWM is widely used but a detailed explanation of the underlying models is often omitted in publications. Therefore, this work aims for a deep theoretical dive into the fundamentals of CIDWM starting from the magnetism in magnetic thin films in section 2.1. Section 2.2 covers the theory behind magnetic DWs by taking all relevant energy terms for a ferrimagnetic bi-layer system into account. Finally in section 2.3, the equations of motion will be derived and implications for measurements discussed. This thesis extends the theoretical discussion of the supplementary information of my paper [21] and provides more detailed information about the derivation of the equations. Some parts of the theory are similar to that of ferromagnetic layers discussed in detail in my master thesis [29].

2.1. Ferromagnetism in thin films

Magnetism of atoms originates from quantum mechanics in which the electron spin and orbital momentum form a magnetic moment $\boldsymbol{\mu}$ which can interact with magnetic fields \boldsymbol{H} .² The theory was first described by DIRAC [31] and HEISENBERG [32] in 1926. Ferromagnetism describes the property of a material where the magnetic moments collectively point into the same direction [33].

2.1.1. Heisenberg exchange model

The HEISENBERG exchange model describes the coupling of the magnetic moments by a coupling of electron spin \boldsymbol{S}^i and \boldsymbol{S}^j of neighboring atoms. The exchange energy is given by

$$E_{\text{Heisenberg}} = -2 J_{\text{ex}}^{ij} \boldsymbol{S}^i \cdot \boldsymbol{S}^j \quad (2.1)$$

where J_{ex}^{ij} is the so-called exchange integral which describes the coupling strength and sign between \boldsymbol{S}^i and \boldsymbol{S}^j [33]. If the spins couple together, they create an exchange field experienced by the other moments - this is the so-called mean field approximation [33]. Depending on the crystal lattice of a material, the exchange interaction can also be described by the exchange stiffness A_{ex} . A_{ex}^i can be calculated by J_{ex}^{ii} and S^i for an exchange interaction within the same material i .

The coupling of the spins within RE metals or TMs as well as the coupling between RE metal spins and TM spins has been investigated for example in [34] and [35]. Within this model, it was found that $S^{\text{Co}} = 0.59$, $S^{\text{Ni}} = 0.24$, and $S^{\text{Gd}} = 3.5$ as well as $J_{\text{ex}}^{\text{Co,Co}} = 3.53 \times 10^{-21}$ J,

² Commonly (cf. [30]), \boldsymbol{H} denotes the magnetic field strength or magnetizing force. The unit would be A m^{-1} . However, in the literature, often “magnetic field” \boldsymbol{H} is used but the magnetic flux density is meant, also known as magnetic induction, which would correctly be denoted by \boldsymbol{B} . The unit of \boldsymbol{B} is T. To be consistent with recent works, in this thesis $[\boldsymbol{H}] = \text{T}$.

2. Theoretical foundations

$J_{\text{ex}}^{\text{Co,Ni}} = 1.32 \times 10^{-21}$ J, $J_{\text{ex}}^{\text{Ni,Ni}} = 1.04 \times 10^{-21}$ J, $J_{\text{ex}}^{\text{Ni,Gd}} = -1.00 \times 10^{-22}$ J, $J_{\text{ex}}^{\text{Gd,Gd}} = 2.70 \times 10^{-23}$ J, and $J_{\text{ex}}^{\text{Gd,Co}} = -1.46 \times 10^{-22}$ J [34].

On the one hand, it shows that the spins of the same material couple ferromagnetically with themselves. Likewise, spins between TMs like Co and Ni couple also ferromagnetically. In case of TMs, the HEISENBERG exchange model is only a rough model as it considers a localization of the spins which is not given because the conduction electrons are itinerant. Therefore, in case of TMs the STONER model is commonly more accepted [36].

On the other hand, it was shown experimentally that spins of RE metals couple to spins of TMs, like Co and Gd, antiferromagnetically (e.g. $J_{\text{ex}}^{\text{Gd,Co}} < 0$). In case of RE metals, the coupling mechanism can better be described by the RKKY exchange interaction because the $4f$ electrons do not interact directly with each other [33]. The RKKY interaction is discussed in more detail in section 2.1.5.1.

2.1.2. Landé g-factor

If a free atom or ion is considered, its magnetic moment is given by

$$\boldsymbol{\mu} = -|\gamma| \mathbf{J} = -g \frac{\mu_{\text{B}}}{\hbar} \mathbf{J} \quad (2.2)$$

with the gyromagnetic ratio γ , the reduced PLANCK constant \hbar , the BOHR magneton μ_{B} , the LANDÉ g-factor g , and the total angular momentum \mathbf{J} which is the sum of the spin and orbital angular momentum [33]. γ describes the ratio of the magnetic moment to the angular momentum and depends on the electronic configuration of the atom or ion. The sign of γ is not consistently treated in the literature. This work follows the recommended standard and uses γ as a positive constant.³

The LANDÉ g-factor, also called the spectroscopic splitting factor, can be calculated by the LANDÉ equation which takes the spin-orbit interaction of the valence electrons into account. It is given by

$$g = 1 + \frac{J(J+1) + S(S+1) - L(L+1)}{2J(J+1)}$$

where S is the spin angular momentum, L the orbital angular momentum and J the vector sum of both [39].⁴ Some LANDÉ g-factors for materials used in this study are given in Table 2.1. The consequence of the difference in the LANDÉ g-factor for different materials grown in magnetic multilayer thin films is one important focus of this work.

As the spin angular momentum in RE metals is deeply hidden in the $4f$ shell within the $5s$ and $5d$ shells, these magnetic $4f$ electrons have the same angular-momentum quantum number like

³ In old literature, for example, GILBERT used a negative sign [37] but the National Institute of Standards and Technology defines it to be positive [38]. As the sign of γ determines the rotation direction of the magnetization \mathbf{M} in presence of an external field \mathbf{H} , it is experimentally given that $\dot{\mathbf{M}} = -|\gamma| \mathbf{M} \times \mathbf{H}$.

⁴ The formula in [39] was corrected after the discovery of the quantum mechanical formula of the orbital angular momentum in 1925.

Material	g^i (exp.)	g^i (theo.)	g^i (used in present study)
Co	2.2 [40]	2.14 (fcc) [44]	2.2
	2.139 (fcc) [41]		
	2.145 (fcc) [42]		
	2.18 (hcp) [42]		
	2.148 [43]		
Ni	2.19-2.42 [40]	2.12 (fcc) [44]	2.2
	2.182 [41]		
	2.208 [43]		
Gd	1.99 [45]	2.0 [46]	2.0
Tb	1.493 [47]	1.5 [46]	1.5

Table 2.1.: Literature values for Landé g-factor. Experimental and theoretical values of the LANDÉ g-factor g^i of materials i . Some values are shown for different crystal structures - either fcc or hcp. Right column shows values used in the present study.

free ions [46]. In this case, the LANDÉ equation applies to calculate g which results in $g^{\text{Gd}} = 2$ and $g^{\text{Tb}} = 1.5$ [46] which is close to the experimental values (Table 2.1).

In contrast, in TMs the spin angular momentum arises from the electrons in the $3d$ shell which also form the conduction band. Therefore, the electrons experience a large electric field, the so-called crystal field, which influences the orbital angular momentum [33]. This is commonly known as quenching of the orbital angular momentum. This finally causes a deviation of the LANDÉ g-factors from the LANDÉ equation. Experimentally, various values of g^{Co} were found (Table 2.1) which can be attributed to film quality and crystal orientation.

The LANDÉ g-factor increases with decreasing thickness of the magnetic film as it was observed for Pt/Co [48] and Co/Ni multilayers [43]. In the present study, the thickness of the Co and Ni films is below 1 nm. Therefore, the upper bound values for g^{Co} and g^{Ni} are assumed. In the present study, $g^{\text{Co}} = 2.2$ and $g^{\text{Ni}} = 2.2$ as well as $g^{\text{Gd}} = 2.0$ are used.⁵ Further, note that g is considered not to vary significantly with temperature (cf. [45]).

2.1.3. Saturation magnetization and Curie temperature

The materials under investigation in this study are called ferromagnets. In contrast to para- and diamagnetism, ferromagnetism describes the property of a material in which the magnetic moments of the atoms in a crystal exhibit a spontaneous ordering which leads to a total magnetization M . It is given by the sum of the magnetic moments μ^i in the material

$$M = \frac{1}{V} \sum_i \mu_i$$

⁵ Experiments with samples consisting of Co/Tb/Co tri-layers were performed in the context of this thesis. However, the results were not useful as the compensation temperatures of the Co and Tb layers did not lie within the measured temperature range.

2. Theoretical foundations

where V is the volume of the material. Its absolute value is called the saturation magnetization M_s [33]. In the context of the thesis at hand, it will become useful to describe \mathbf{M} in spherical coordinates

$$\mathbf{M}(M_s, \theta, \phi) = M_s \begin{pmatrix} \cos \phi \sin \theta \\ \sin \phi \sin \theta \\ \cos \theta \end{pmatrix}$$

where θ is the polar and ϕ the azimuth angle. It can be possible that θ and ϕ vary locally in a thin film.

Thermal fluctuations reduce M_s . At $T = 0$ K the ordering of the magnetic moments is at maximum and decreases with increasing temperature until it disappears at a critical temperature T_C , the CURIE temperature. Above T_C the material changes into an disordered paramagnetic phase [33]. The temperature dependence of $M_s(T)$ can be expressed by

$$M_s(T) = M_{s,T=0} \left(1 - \frac{T}{T_C}\right)^\varepsilon \quad (2.3)$$

with the critical exponent ε which describes the curve between $T = 0$ and $T = T_C$. For $\varepsilon = \frac{3}{2}$ this temperature dependence is also called BLOCH's law in which only the HEISENBERG nearest-neighbor interaction (equation (2.1)) is considered [49].

T_C highly depends on the thickness of the magnetic layer [50] and its purity [51] as well as on the proximity of the layer to other materials [52]. For example, in multilayers with alternating ultra-thin layers of Tb and Co, Tb shows a magnetic order at room temperature [52].⁶ In Table 2.2, literature values for T_C and M_s of bulk samples of materials used in the present study are summarized.

Material	$M_{s,T=0}$ (kA m ⁻¹)	T_C (K)
Co	1446 [33]	1423 [53]
Ni	510 [33]	631 [51]
Gd	2060 [33]	293 [54]
Tb	2665 [55]	222 [56]

Table 2.2.: Literature values for saturation magnetization and Curie temperature. Bulk values of saturation magnetization M_s at $T = 0$ K and CURIE temperature T_C .

2.1.4. Magnetic anisotropy

The HEISENBERG exchange, discussed in section 2.1.1, is isotropic. This means that the magnetic moments only interact among each other but the magnetization has no favored direction. However, in crystals \mathbf{M} usually follows a certain direction. Thus, other energies must break the isotropy.

⁶ The layer thickness in which the magnetic moments of Tb couple to the magnetic moments of Co at room temperature is about 1.5 nm [52].

These are called magnetic anisotropy energies. Looking from a thermodynamic point of view, it is common to describe them by the GIBBS free energy density $G(\hat{\mathbf{M}})$, where $\hat{\mathbf{M}}$ denotes the direction of the magnetization.

Magnetic anisotropy energies are much smaller than the exchange energy described by equation (2.1). The direction of $\hat{\mathbf{M}}$ with respect to the preferred crystal axis where the energy is minimized is the easy axis. The directions perpendicular to the easy axis is the hard axis. The field to rotate the magnetization from the easy axis to the hard axis is of the order of 10 - 10 000 kA m⁻¹ [33]. Such fields can be produced for instance by commercial electromagnets and thus give rise to many applications for data storage.

Two effects play a role for the anisotropy energies of crystals: the relativistic spin-orbit coupling and the dipole-dipole interaction. The former is relevant for an orientation of the magnetization along a crystal axis and is therefore known as the crystalline or magnetocrystalline anisotropy. The latter is causing a reaction of the magnetization depending on the shape of the sample and is called shape- or demagnetization anisotropy. Thus, the GIBBS free energy density is the sum of both contributions: $G(\hat{\mathbf{M}}) = G_{\text{cryst}}(\hat{\mathbf{M}}) + G_{\text{shape}}(\hat{\mathbf{M}})$.

The nanowires, which are used for the experiments here, are etched out of thin films. These thin films are only a few nanometers thick. The magnetism is predominantly determined by a ferromagnetic layer, e.g. Co, which is grown on top of a Pt layer.

In the case of a thin film, the dimensions of the system are reduced. Hence, the symmetry conditions are different compared to a bulk material and surface effects become more important. This is leading to an additional contribution to the GIBBS free energy density, which is then given by $G(\hat{\mathbf{M}}) = \int_V dV G^V(\hat{\mathbf{M}}) + \int_S dS G^S(\hat{\mathbf{M}})$. $G^V(\hat{\mathbf{M}})$ is the GIBBS free energy density for the volume and $G^S(\hat{\mathbf{M}})$ is GIBBS free energy density for the surface. The surface anisotropy becomes more important as the thickness of the magnetic layer is reduced.

The GIBBS free energy density ends up with four terms: the contribution of the magnetocrystalline anisotropy of the volume $G_{\text{cryst}}^V(\hat{\mathbf{M}})$ and the surface $G_{\text{cryst}}^S(\hat{\mathbf{M}})$, as well as the shape anisotropy of the volume $G_{\text{shape}}^V(\hat{\mathbf{M}})$ and the surface $G_{\text{shape}}^S(\hat{\mathbf{M}})$. In the case of an infinitely extended thin film (thickness less than 1 nm), $G_{\text{cryst}}^S(\hat{\mathbf{M}})$ and $G_{\text{shape}}^V(\hat{\mathbf{M}})$ are most relevant.

2.1.4.1. Magnetocrystalline anisotropy

If a film with a film normal axis in z direction like in Figure 2.1 is considered, the surface contribution to the magnetocrystalline anisotropy is given by⁷

$$G_{\text{cryst}}^S(\hat{\mathbf{M}}) = K_{\text{cryst}}^S \sin^2 \theta.$$

K_{cryst}^S is the anisotropy constant, here, of the surface contribution to the magnetocrystalline anisotropy. $\theta \in [0, \pi]$ is the polar angle. $\hat{\boldsymbol{\theta}}$ denotes the unit vector of the polar angle θ in the following. K_{cryst}^S is positive so that the energy is minimized at $\theta = 0$ or π . Thus, due

⁷ Terms of higher order are neglected.

2. Theoretical foundations

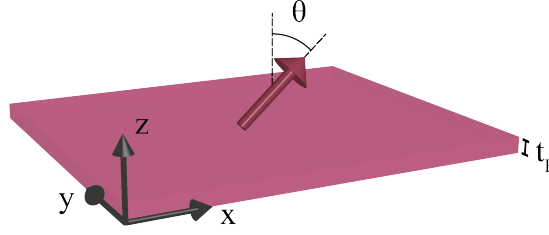


Figure 2.1.: Orientation of magnetization in thin film. Magnetic thin film with film normal axis in z direction. Colored arrow indicates direction of magnetization \mathbf{M} of magnetic thin film. Polar angle θ indicates how the magnetization is orientated with respect to film normal axis. Magnetization points usually either out-of-plane ($\theta = 0$ or π) or in-plane ($\theta = \frac{1}{2}\pi$ or $\frac{3}{2}\pi$) determined by anisotropy energies.

to the magnetocrystalline anisotropy, the magnetization is pointing out of the film plane. In the remainder of the thesis, the index S for surface will be omitted and K_{cryst} refers always to the surface contribution of the magnetocrystalline anisotropy. A typical value for K_{cryst} is, for example, 0.31 mJ m^{-2} for a Co/Ni multilayer [57], reflecting the anisotropy energy at a single interface.

2.1.4.2. Shape anisotropy

The volume contribution to the shape anisotropy is generally given by

$$G_{\text{shape}}^{\text{v}}(\hat{\mathbf{M}}) = \frac{\mu_0}{2} M_{\text{S}}^2 \hat{\mathbf{M}} \underline{\mathbf{N}} \hat{\mathbf{M}}$$

where μ_0 is the vacuum permeability given by $\mu_0 = 4\pi \times 10^{-7} \text{ N A}^{-2}$ and $\mathbf{M} = M_{\text{S}} \hat{\mathbf{M}}$ [58]. $\underline{\mathbf{N}}$ is a matrix which is determined by the shape. It is simplified for a uniformly magnetized ellipsoid to a diagonal matrix with the entries N_x , N_y and N_z , called the demagnetization factors. The indices denote the direction in x , y and z direction of a CARTESIAN coordinate system. The demagnetization factors are restricted to $N_x + N_y + N_z = 1$. In the case of the film in x - y -plane, $N_x = N_y = 0$ and $N_z = 1$. Therefore,

$$G_{\text{shape}}^{\text{v}}(\hat{\mathbf{M}}) = \frac{\mu_0}{2} M_{\text{S}}^2 \cos^2 \theta.$$

$G_{\text{shape}}^{\text{v}}(\hat{\mathbf{M}})$ is at minimum at $\theta = \frac{\pi}{2}$. Consequently, due to the shape anisotropy the magnetization is forced to lie in the film plane. The shape anisotropy can be associated with a demagnetization field \mathbf{H}_{d} inside the film which is given in general by $\mathbf{H}_{\text{d}} = -\mu_0 \underline{\mathbf{N}} \mathbf{M}$. Here, $\mathbf{H}_{\text{d}} = -\mu_0 M_{\text{S}} \hat{\mathbf{z}}$. Often, a shape anisotropy constant

$$K_{\text{shape}}^{\text{v}} = -\frac{\mu_0}{2} M_{\text{S}}^2$$

is used which is in competition with the magnetocrystalline surface anisotropy. In the remainder of the paper, the index V for volume will be omitted and K_{shape} always refers to the volume contribution of the shape anisotropy.

2.1.4.3. Effective anisotropy

In a system like a Co thin film, the volume shape and surface magnetocrystalline anisotropy are competing and, depending on the thickness of the ferromagnetic material denoted by t_{F} , the orientation of the magnetization is determined. The observed behavior in multilayers can be described by the effective anisotropy [59–61]

$$K_{\text{eff}} = K_{\text{shape}} + 2 \frac{K_{\text{cryst}}}{t_{\text{F}}}. \quad (2.4)$$

Note that the factor of 2 arises from the two interfaces of the magnetic layer in a multilayer of the same two materials like [Pd/Co] [60].

If $K_{\text{eff}} > 0$, the magnetization is out-of-plane and if $K_{\text{eff}} < 0$, the magnetization is in-plane. Below a critical thickness $t_{\text{F}}^0 = -2 K_{\text{cryst}}/K_{\text{shape}}$, the material has an out-of-plane magnetization and therefore is said to have a perpendicular magnetic anisotropy (PMA). It is found that this PMA is, for example, created at a Pt/Co interface [62] where it is caused by the interfacial hybridization of orbital moments in Pt [63]. The minimal applied field $\mathbf{H}_{\text{eff,S}}$ to drive the whole (out-of-plane) magnetization from the easy axis into the hard axis (in-plane) is given by

$$\mathbf{H}_{\text{eff,S}} = \frac{2 K_{\text{eff}}}{M_{\text{S}}} \hat{\mathbf{r}}_{\text{in-plane}}. \quad (2.5)$$

2.1.5. Magnetic multilayers

The films studied in the context of this thesis consist of magnetic multilayers. Each magnetic layer i is treated separately in terms of its magnetic moment.⁸ All layers have the same lateral size in x and y direction but could be of a different thickness t^i . Note that the index F is neglected in the remainder if another index referring to the layer is present (t_{F} needs to be distinguishable from the time variable t). Each layer exhibits a magnetization \mathbf{M}^i . To calibrate the total magnetic moment of each layer, the quantity

$$\mathbf{m}^i(T) \stackrel{\text{def}}{=} t^i \mathbf{M}^i(T) = t^i M_{\text{S}}^i(T) \hat{\mathbf{M}}^i$$

will be used in the remainder of the manuscript with the unit $[m^i] = \text{A}$. Note that it could be possible that the thickness of the ferromagnetic state of a layer could be temperature-dependent as well. For example if $T > T_{\text{C}}^i$, an adjacent magnetic layer j for which $T < T_{\text{C}}^j$ could induce a magnetization in layer i at the interface. Such kind of effects will be implicitly included in $m^i(T)$.

⁸ The magnetization of a ferromagnetic Co/Ni/Co sample is treated as a whole because the DW motion is not influenced by this simplification in this case.

2. Theoretical foundations

2.1.5.1. Ruderman–Kittel–Kasuya–Yosida interaction

The RKKY exchange interaction describes the indirect exchange of localized magnetic moments of atoms in a metal [10–12]. The spins of the conduction electrons act as intermediaries between the magnetic moments. The theory is based on BLOCH wavefunctions and is therefore only applicable to crystalline systems. Due to the oscillatory behavior of the coupling mechanism, the coupling of the atoms' magnetic moments is either ferromagnetic or antiferromagnetic.

The RKKY exchange interaction becomes relevant in case of RE metals but also in case of TMs thin films which are separated by a spacer layer. J_{ex} denotes the interlayer exchange coupling strength. In SAFs structures, the coupling oscillates between a ferromagnetic and antiferromagnetic state depending on the spacer layer thickness [64].⁹ The coupling strength thereby decreases with increasing spacer layer thickness.

The exchange energy density ω_J between the two magnetic layers grown on top of each other is - similar to equation (2.1) - given by [65, 66]

$$\omega_J = -J_{\text{ex}} \hat{\mathbf{m}}^{\text{L}} \cdot \hat{\mathbf{m}}^{\text{U}} \quad (2.6)$$

where $\hat{\mathbf{m}}^{\text{L}}$ and $\hat{\mathbf{m}}^{\text{U}}$ are the unit vectors of the magnetization of the lower and upper layer, respectively. If $J_{\text{ex}} < 0$, the coupling is antiferromagnetic. If $J_{\text{ex}} > 0$, the coupling ferromagnetic.

2.1.5.2. Magnetic moment and angular momentum compensation

In case of ultra-thin layers of two TMs, like Co and Ni, the magnetic moments couple ferromagnetically [67] so that the magnetic moments are adding up to a net magnetic moment $m_{\text{net}}(T)$. In this case of ferromagnetic coupling, the layers can be treated as one single magnetic layer where the net magnetic moment is given by $m^{\text{F}} \stackrel{\text{def}}{=} m_{\text{net}} = m^i + m^j$.

In contrast, as discussed in section 2.1.1, the coupling of the magnetic moments of a RE and a TM, for example Gd and Co, is antiferromagnetic. Therefore, the magnetic moments of RE metal and TM ultra-thin films and alloys¹⁰ couple antiferromagnetically as well [52, 68, 69]. Consequently, in this case $m_{\text{net}}(T)$ is the difference $m_{\text{net}} = |m^i - m^j|$.

Generally, the net magnetic moment can be expressed by

$$\mathbf{m}_{\text{net}}(T) = \mathbf{m}^i(T) + \mathbf{m}^j(T).$$

If \mathbf{m}^i is parallel or antiparallel to \mathbf{m}^j , $m_{\text{net}}(T) = |m^i(T) + \text{sgn}(J_{\text{ex}}) m^j(T)|$ where the function $\text{sgn}(J_{\text{ex}})$ returns the sign of J_{ex} .

Due to the distinct temperature dependence of the materials (section 2.1.3) generally $\frac{dm^i(T)}{dT} \neq \frac{dm^j(T)}{dT}$. Hence, $m_{\text{net}}(T)$ is temperature-dependent and a magnetic moment compensation

⁹ For example, the oscillation period is about 12 Å in Ni₈₀Co₂₀ layers separated by Ru spacer layers [64].

¹⁰ For Co/Tb multilayers it has been shown that if the thickness of each layers is less than 1 nm, the multilayer behaves like an alloy [52].

temperature

$$T_M \stackrel{\text{def}}{=} T \Big|_{m_{\text{net}} = 0}$$

can be found where $m_{\text{net}}(T_M) = 0$.

When it comes to ferrimagnetic multilayers, another important quantity is the total angular momentum¹¹ of a layer i

$$\mathbf{A}^i(T) \stackrel{\text{def}}{=} \frac{\mathbf{m}^i(T)}{\gamma^i}.$$

\mathbf{A}^i plays a crucial role for the domain wall motion dynamics. As the LANDÉ g-factors of the materials are distinct, γ^i is material-dependent. Hence, also a net angular momentum

$$\mathbf{A}_{\text{net}}(T) = \mathbf{A}^i(T) + \mathbf{A}^j(T)$$

can be defined. As a consequence and due to the temperature dependence of $\mathbf{m}^i(T)$, there is another temperature

$$T_A \stackrel{\text{def}}{=} T \Big|_{A_{\text{net}} = 0} \tag{2.7}$$

where the angular momenta compensate.

Note that in SAF structures, consisting of two ferromagnetic layers coupled through a spacer layer via the RKKY interaction, $\frac{dm^i(T)}{dT} \approx \frac{dm^j(T)}{dT}$. Thus, there is almost no temperature dependence of m_{net} . Since both layers are of the same material, γ is the same and A_{net} is temperature-independent as well. If the magnetic moments of both layers are equal, the SAF structure is at angular momentum and magnetic moment compensation at all temperatures.

2.2. Domain walls in ferrimagnetic bi-layers

In the preceding section, it has been assumed that all magnetic moments in a magnetic thin film are orientated in the same direction which can be described by θ . However, it is possible that inside the film, regions exist that are magnetized in opposite directions. These regions are called magnetic domains. Magnetic domains are commonly used as bits in storage memories like hard disk drives. The region between two magnetic domains is called magnetic domain wall (DW). Within the DW the magnetic moments rotate laterally in θ from one to the other domain direction. Anisotropy energies determine the size of the region of rotation measured by the DW width Δ . In order to mathematically deduce the rotation in θ , a common concept of the description of DWs is to look at the rotation of the magnetic moments along a line in a certain direction within the thin film plane. This so-called one-dimensional model is especially applicable if a magnetic strip is considered which is etched out of a thin film. Such magnetic strips are relevant for the racetrack memory described in the introduction.

¹¹ $\mathbf{A} = \frac{t_F}{V} \sum_i \mathbf{J}_i$ where the total angular momentum \mathbf{J}_i is defined in equation (2.2).

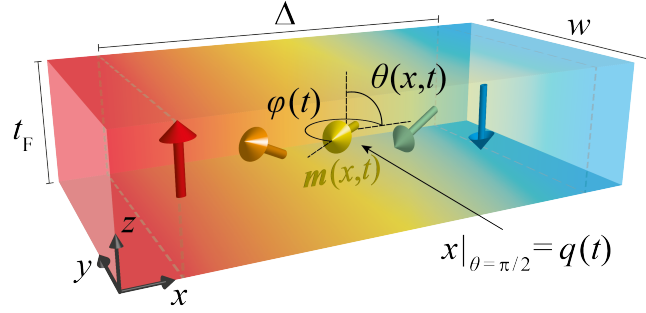


Figure 2.2.: Domain wall profile and coordinate system. Domain wall of width Δ in a magnetic nanowire of width w and height t_F . Magnetic moments $\mathbf{m}(x, t)$ rotate time-dependently (denoted by t) in $\theta(x, t)$ from an up (\uparrow) to a down (\downarrow) state in x direction. The center of the domain wall is denoted by $x = q(t)$ where $\theta = \pi/2$. Magnetic moments can all be rotated by an azimuth angle $\phi(t)$.

2.2.1. One-dimensional model

Within this one-dimensional model, it is assumed that the film is confined in one direction so that a wire or a very thin strip with a width w and thickness t_F is created where $w \gg \Delta$. The situation is depicted in Figure 2.2. Without loss of generality, it is supposed here that the wire is along x direction and the spatial confinement in y direction. Furthermore, the film is very thin and the material is exhibiting an out-of-plane anisotropy. It is assumed that one end of the wire is magnetized in z (equivalent to $\theta = 0$), also denoted by \uparrow , and the other end in $-z$ (equivalent to $\theta = \pi$), or \downarrow , direction. The DW configuration is denoted as $\uparrow\downarrow$ or $\downarrow\uparrow$ if the change is from a \uparrow to a \downarrow domain or from a \downarrow to a \uparrow domain following positive x direction, respectively. Within the DW, the magnetization rotates gradually with θ from the orientation of one domain to the orientation of the other domain. The position center of the DW is given at $x|_{\theta=\pi/2} = q$. The notation $x|_{\theta=\pi/2}$ shall denote: x evaluated at $\theta = \pi/2$. The DW center position is time-dependent: $q = q(t)$.

Note that this one-dimensional model can describe, in a simple manner, most behaviors relevant to this work. However, it is important to realize that the assumption to reduce the DW in such kind of strip with finite width w to a one-dimensional object leads to inaccuracies. For example, the DW velocity in a curved nanowire highly depends on the radius and w as shown in [70].¹²

The aim of the remainder of this section is to derive the total energy density ω_{DW} of the DW. Since magnetic moments vary in x direction, this energy density is dependent on x such that $\omega_{\text{DW}}(x)$. In order to obtain the total DW energy σ_{DW} , the final step is to integrate $\omega_{\text{DW}}(x)$ over x .

¹² To explain such results, a quasi-two-dimensional model could to be used, as introduced in section A.3 in the appendix for a ferrimagnetic bi-layer system.

2.2.2. Domain wall profile

Within the one-dimensional model, the DW profile in spherical coordinates is commonly described by [71]

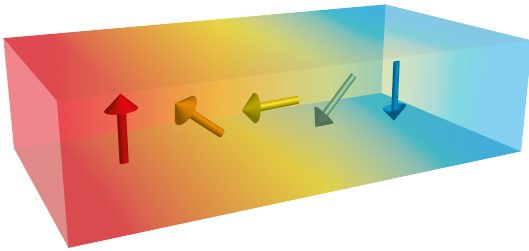
$$\theta(x, t) = 2 \tan^{-1} \left[\exp \left(\pm \frac{x - q(t)}{\Delta} \right) \right]. \quad (2.8)$$

From now on, if a \pm or \mp sign appears, the upper sign always describes a $\uparrow\downarrow$ and the lower sign a $\downarrow\uparrow$ DW. For example, in equation (2.8) the $+$ applies for a $\uparrow\downarrow$ and the $-$ for a $\downarrow\uparrow$ DW. In case of bi-layers, the DW configuration always applies to the lower magnetic layer. Note that the DW profile in equation (2.8) fulfills $\lim_{x \rightarrow \mp\infty} \theta = 0$ and $\lim_{x \rightarrow \pm\infty} \theta = \pi$. An important equality for the motion of the DW, described by the DW velocity \dot{q} , is

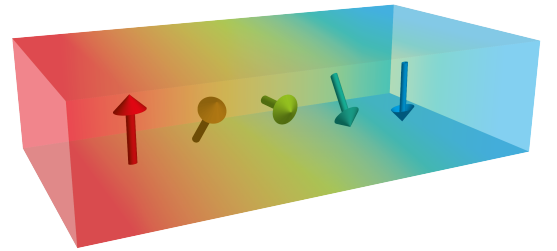
$$\dot{\theta} = \mp \frac{1}{\Delta} \sin \theta \dot{q}.$$

\dot{X} denotes the time derivative $\frac{dX}{dt}$ of a variable X . Additional mathematical properties of the function (2.8) can be found in section A.1 in the appendix.

Further, it is possible that the magnetic moments inside the wire rotate by an azimuth angle $\phi \in [0, 2\pi]$. This is also depicted in Figure 2.2. Depending on ϕ there are two major different kinds of DW types: The NÉEL DW, depicted in Figure 2.3a, is characterized by a rotation of the magnetization within the plane of the DW (with $\phi = 0$ or π) while the magnetization of a BLOCH DW, depicted in Figure 2.3b, rotates through the plane of the DW (with $\phi = \frac{1}{2}\pi$ or $\frac{3}{2}\pi$). Which type of DW is formed depends on the energies influencing the direction of rotation. Note that, within the one-dimensional model, ϕ is fixed for all moments within the nanowire along x direction, meaning $\frac{\partial\phi}{\partial x} = 0$. $\hat{\phi}$ denotes the unit vector of the azimuth angle ϕ which points into increasing ϕ direction in the $x - y$ plane.



(a) NÉEL domain wall with $\phi = \pi$.



(b) BLOCH domain wall with $\phi = \frac{3}{2}\pi$.

Figure 2.3.: Néel and Bloch domain wall. Domain wall types depending on ϕ .

Domain wall is NÉEL-type if $\phi = 0$ or π and BLOCH-type if $\phi = \frac{1}{2}\pi$ or $\frac{3}{2}\pi$.

Within the one-dimensional model which is used here, it is assumed that the magnetic moments of two magnetic layers interact independently but only couple through an interlayer exchange interaction like the RKKY interaction [9]. Due to this interlayer exchange interaction, if a $\uparrow\downarrow$ or $\downarrow\uparrow$ DW appears in one of the layers, the reversed DW ($\downarrow\uparrow$ or $\uparrow\downarrow$, respectively) is present in the other layer. This is depicted in Figure 2.4.

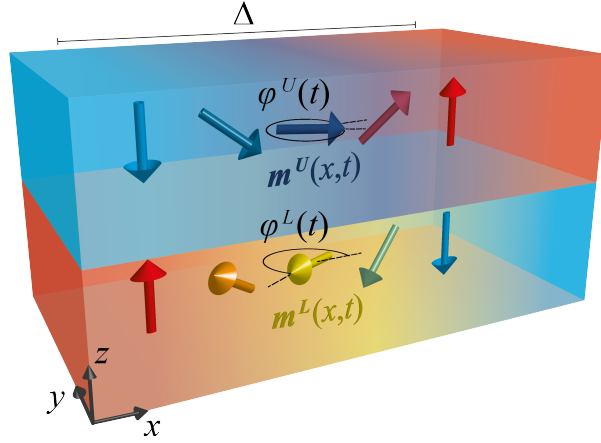


Figure 2.4.: Domain wall in antiferromagnetically coupled bi-layer. DW width Δ is assumed to be equal in both layers. Rotation of magnetic moments in lower layer \mathbf{m}^L and upper layer \mathbf{m}^U with ϕ^L and ϕ^U is possible, respectively. This DW is denoted as a $\uparrow\downarrow$ DW, based on the configuration of the moments along x in the lower layer.

It is assumed that the DW positions q in the upper and lower layer are identical also during motion due to the strong coupling.¹³ On the basis of the reason, it seems plausible to expect that $\Delta^L \approx \Delta^U$. Therefore, from now on, it is assumed that $\Delta \stackrel{\text{def}}{=} \Delta^L = \Delta^U$. In the context of bi-layers, \pm or \mp signs will always refer to the $\uparrow\downarrow$ or $\downarrow\uparrow$ DW configuration in the lower layer, respectively. Consequently, $\theta^U = 2 \tan^{-1} [\exp(\mp \frac{x-q}{\Delta})]$ or $\theta \stackrel{\text{def}}{=} \theta^L = \theta^U - \pi$. Note that therefore, $\sin \theta = \sin \theta^L = \sin \theta^U$ and $\cos \theta = \cos \theta^L = -\cos \theta^U$. Additionally, $\dot{\theta} = \dot{\theta}^L = -\dot{\theta}^U$ and $\dot{q} = \dot{q}^L = \dot{q}^U$.

In contrast to θ rotation, the magnetic moments in the upper and lower layer can independently rotate by the azimuth angles ϕ^U and ϕ^L , respectively. The DW position q (described by θ in equation (2.8)) as well as the azimuth angles ϕ^U and ϕ^L are the generalized coordinates of the systems used to derive the equation of DW motion in section 2.3.2.

2.2.3. Domain wall energy density

The focus of this thesis is to investigate antiferromagnetically exchange-coupled bi-layers. The energy terms relevant for this system are the intra-layer exchange interaction (by direct spin exchange interaction within a layer), the anisotropy energies, the DMI and the inter-layer exchange interaction. The contribution of the demagnetization field of the DW to the final DW energy is considered to be small and is therefore neglected.¹⁴ Since the intra-layer exchange interaction and the effective anisotropy are volume effects, these energy densities have to be

¹³ Note that a recent study of YANG ET AL. shows that this assumption may break down for a low coupling strength [28].

¹⁴ Especially for CIDWM the demagnetization field is not of major importance and is comparably small compared to other energy terms [72].

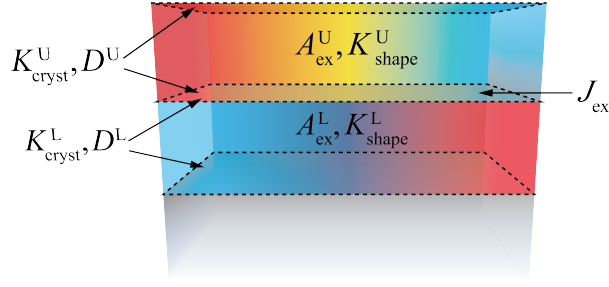


Figure 2.5.: Energy contributions to domain wall energy of upper and lower magnetic layer.

Magnetocrystalline surface anisotropy $K_{\text{cryst}}^{\text{L}}$ and $K_{\text{cryst}}^{\text{U}}$, DMI D^{L} and D^{U} and inter-layer exchange interaction J_{ex} are interface effects. D^i and K_{cryst}^i can have interface contributions at both interfaces. K_{cryst}^i and K_{shape}^i together create the effective anisotropy K_{eff}^i . Intra-layer exchange interaction A_{ex}^i and shape anisotropy K_{shape}^i are volume effects.

adjusted to the thickness t_{F} of each layer. In the following, it is discussed how these energy densities apply to DWs.

All contributions to the total DW energy density are depicted in Figure 2.5. Except for the interlayer exchange energy density, the energy terms are calculated for each layer individually.

2.2.3.1. Intra-layer exchange energy density

Due to the gradual rotation of the magnetization inside the domain wall, the HEISENBERG exchange energy comes into play which favors parallel alignment of the magnetic moments. Hence, this energy term tends to increase the domain wall width so that $\Delta \rightarrow \infty$. The intra-layer exchange energy of the DW in one layer is given by [73]

$$\omega_{\text{A}}^i = A_{\text{ex}}^i t^i (\nabla \hat{\mathbf{m}}^i)^2 = A_{\text{ex}}^i t^i \left(\frac{\partial \theta^i}{\partial x} \right)^2 = \frac{A_{\text{ex}}^i t^i}{\Delta^2} \sin^2 \theta \quad (2.9)$$

which is normalized to the layer thickness t^i .

It may be highlighted that this exchange interaction concerns the exchange between magnetic moments within one layer while the inter-layer exchange discussed in section 2.1.5 concerns the exchange between the two magnetic sublattices. These two exchange interactions can be distinguished by the exchange constants A_{ex}^i and J_{ex} in this thesis. A_{ex}^i refers to the intra-layer exchange. Its dimension is J m^{-1} . J_{ex} refers to the inter-layer exchange. Its unit is J m^{-2} .

2.2.3.2. Anisotropy energy density

As discussed in section 2.1.4, the effective anisotropy favors an out-of-plane magnetization in the systems studied in the present thesis. However, inside a DW the magnetization has to rotate in-plane in order to transform from a \uparrow to a \downarrow state. Consequently, the anisotropy energy density

2. Theoretical foundations

tends to reduce the DW width so that only a few magnetic moments point in-plane. The larger K_{eff} , the smaller Δ . The scaling of Δ with K_{eff} is derived in section 2.2.4.

The energy density related to the effective anisotropy is then given by

$$\omega_{K_{\text{eff}}}^i = t^i K_{\text{eff}}^i \sin^2 \theta. \quad (2.10)$$

where K_{eff}^i denotes the effective anisotropy of layer i .¹⁵

Note that the shape anisotropy of the DW (cf. for example [72]) is neglected in the thesis at hand because it plays a minor role in the ferrimagnetic bi-layer system near magnetic moment compensation. It would be more important if the DMI was not present in the sample. If only the magnetocrystalline and the shape anisotropy were present, the DW would be of the BLOCH-type but various studies [8, 72, 74, 75] showed that in Co thin films NÉEL DWs are formed if the Co layer has a Pt layer on top or underneath.

2.2.3.3. Dzyaloshinskii-Moriya interaction

A likely reason for the creation of NÉEL DWs in Co which is adjacent to a Pt layer is the presence of the DZYALOSHINSKII-MORIYA interaction (DMI) at the interface. This kind of interaction was postulated by DZYALOSHINSKII on the grounds of phenomenological considerations based on LANDAU theory [76]. The DMI is, like the magnetocrystalline anisotropy, a consequence of spin-orbit interactions as it was found by MORIYA [77]. The energy term describing the DMI in case of two coupled spins \mathbf{S}_1 and \mathbf{S}_2 , for example of two neighboring ions, is given by

$$E_{\text{DMI}} = \mathbf{D}_{12} \cdot (\mathbf{S}_1 \times \mathbf{S}_2)$$

where \mathbf{D}_{12} is a constant vector which reflects the strength and direction of the DMI. The magnetic interaction of the spins of the two ions, in this case, is transferred via a third ion (ligand) by a superexchange mechanism. Hence, in contrast to the HEISENBERG exchange (equation (2.1)), the DMI is an indirect exchange interaction. The arrangement of the three ions determines the orientation of the DMI vector \mathbf{D}_{12} . This is depicted in Figure 2.6. The DMI vector \mathbf{D}_{12} is proportional to $\mathbf{r}_{12} \times \mathbf{a}$, where \mathbf{r}_{12} is the connecting vector of the two ions and \mathbf{a} is perpendicular to \mathbf{r}_{12} and intersects at the position of the ligand [78, 79]. From a mathematical perspective, E_{DMI} is a pseudoscalar which implies that the exchange is antisymmetric.

In contrast to the HEISENBERG exchange (equation (2.1)) where the spins favor an antiparallel or parallel alignment to each other, the DMI favors a canting of the spins. The energy is at a minimum if \mathbf{S}_1 is orthogonal to \mathbf{S}_2 and the cross product $\mathbf{S}_1 \times \mathbf{S}_2$ is antiparallel to \mathbf{D}_{12} .

¹⁵ In equation (2.4) the same magnetocrystalline anisotropy at the upper and lower interface is assumed (hence the factor of 2). This equation was derived for multilayers of the same two materials. In contrast, here both interfaces of each layer are distinct: The lower interface of Co is Pt/Co and the upper Co/Gd while the lower interface of Gd is Co/Gd and the upper Gd/TaN (see section 3.1 for details about the growth). The total magnetocrystalline surface anisotropy of layer i is therefore $K_{\text{cryst}}^i = K_{\text{cryst,lower interface}}^i + K_{\text{cryst,upper interface}}^i$, the sum of the contributions at both interfaces, as it is illustrated in Figure 2.5.

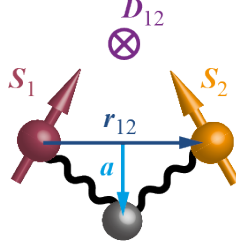


Figure 2.6.: Illustration of Dzyaloshinskii-Moriya interaction. Coupling of the spins of two ions S_1 and S_2 is transferred via a third ion (ligand) via superexchange mechanism. Geometry determines the direction of the DMI vector $\mathbf{D}_{12} \sim (\mathbf{r}_{12} \times \mathbf{a})$. \mathbf{r}_{12} connects ion with S_1 to ion with S_2 . \mathbf{a} is orthogonal to this connecting vector and intersects at the position of the ligand. Similar illustrations can be found in [78, 79].

In case of Pt/Co interfaces, the DMI arises from symmetry breaking at the interface [80]. Considering a DW in a nanowire (cf. Figure 2.2), the DMI exchange energy density in the continuum form is given by [7, 81]

$$\omega_{\text{DMI}} = \sum_l \mathbf{D}_l \cdot \left(\hat{\mathbf{m}} \times \frac{\partial \hat{\mathbf{m}}}{\partial r_l} \right). \quad (2.11)$$

The orientation of \mathbf{D}_l is here dependent on the orientation of the DW with respect to the crystal axis [81]. The index l labels two orthogonal spatial coordinates parallel to the surface plane. It is assumed that the DMI is isotropic. In case of $l = x$, $\mathbf{D}_x = D \hat{\mathbf{y}}$ and in case of $l = y$, $\mathbf{D}_y = D \hat{\mathbf{x}}$.¹⁶ In the one-dimensional model, $\frac{\partial \mathbf{m}}{\partial y} = 0$. This implies, looking at equation (2.11), that the only relevant component of \mathbf{D}_l is \mathbf{D}_x which is pointing in y direction. By inserting \mathbf{D}_x in equation (2.11) it can easily be shown that ω_{DMI} is minimized if $\mathbf{m} \times \frac{\partial \mathbf{m}}{\partial x}$ is antiparallel to \mathbf{D}_x . This can only be fulfilled in case of a NÉEL DW (Figure 2.3a).

One assumption in this thesis is that DMI mainly arises in the Co layer as there has been no DMI reported at a TM/RE (Co/Gd) interface. It may be noted that there is the possibility that DMI in the RE layer or a contribution to the DMI in the TM layer arises at the TM/RE interface.¹⁷ The DMI constant used for the Co layer is $D^{\text{Co}} = 0.2 \text{ pJ m}^{-1}$.

Using the DW profile (equation (2.8)), equation (2.11) can be rewritten as

$$\omega_{\text{DMI}}^i = \mathbf{D}_x^i \cdot \left(\hat{\mathbf{m}}^i \times \frac{\partial \hat{\mathbf{m}}^i}{\partial x} \right) = D^i \hat{\mathbf{y}} \cdot \left(\hat{\mathbf{m}}^i \times \frac{\partial \hat{\theta}^i}{\partial x} \hat{\theta} \right) = \pm \varsigma^i \frac{D^i}{\Delta} \cos \phi^i \sin \theta. \quad (2.12)$$

¹⁶ D can be positive or negative, depending on the material and the orientation to the crystal axis [81]. The experiments, which were performed here, always gave a positive value for D .

¹⁷ In [25] a Pt/Co/GdO_x system was studied. Different Gd thicknesses, which were oxidized, were studied. While it was expected that the Gd layers were oxidized, it remained unknown if the thickest Gd layer was thoroughly oxidized as well. Finally, a low D^{Co} value was reported for the thickest Gd layer. In case the layer was not thoroughly oxidized, the situation is very similar to the here studied system.

2. Theoretical foundations

where

$$\zeta^i \stackrel{\text{def}}{=} \begin{cases} +1 & \text{if } i = \text{L} \\ -1 & \text{if } i = \text{U}. \end{cases} \quad (2.13)$$

An important feature of the DMI is the conservation of chirality of successive DWs which is from a mathematical perspective resulting from the fact that ω_{DMI} is pseudoscalar. In the case of a nanowire, uniformly made of the same materials, \mathbf{D}_i is pointing always in the same direction over the whole wire. Therefore, the magnetization of successive DWs will always rotate in the same direction. In Figure 2.7, the aforementioned findings are depicted. The chirality can be either clockwise or counterclockwise. It can be read by aligning the thumb parallel to \mathbf{m} and following the magnetization from the left to the right. In Figure 2.7, both DWs are rotating counterclockwise. This situation was also observed in the experiments. The chirality conservation induced by the DMI is of particular importance for the current-induced DW motion discussed in section 2.3.5.

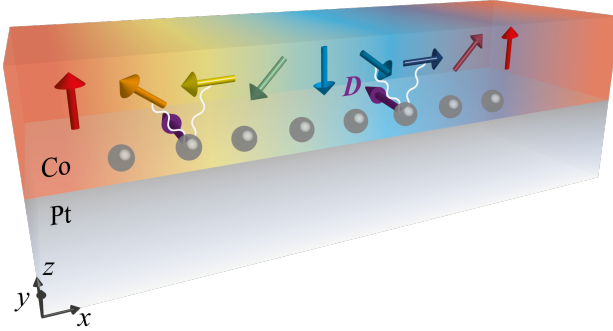


Figure 2.7.: Chirality conservation of successive domain walls by Dzyaloshinskii-Moriya interaction. Two successive DWs ($\uparrow\downarrow$ and $\downarrow\uparrow$) in a Co layer adjacent to Pt layer. Magnetic moments in Co layer experience DMI by superexchange through Pt atoms. Due to DMI, chirality of DWs is retained - both DWs rotate counterclockwise (following magnetization into \hat{x} direction). DMI vector \mathbf{D} denotes the direction of exchange (cf. Figure 2.6).

Furthermore, it needs to be highlighted that the chirality of a DW is induced by the exchange coupling for one to another layer. Therefore, even if the DMI in a Gd is low the chirality of DWs is also induced into an antiferromagnetically exchange-coupled Gd layer as depicted in Figure 2.8.

2.2.3.4. Exchange-coupled domain walls

In exchange-coupled systems, the exchange coupling for example between a Co and Gd layer has also be taken into account for the total DW energy density. Within the one-dimensional model, it can be assumed that the moments of one magnetic sub-lattice couple through a mean field with the magnetic moments of the other sub lattice. This coupling can either be through an indirect RKKY interaction with a spacer layer described in section 2.1.5 or through direct

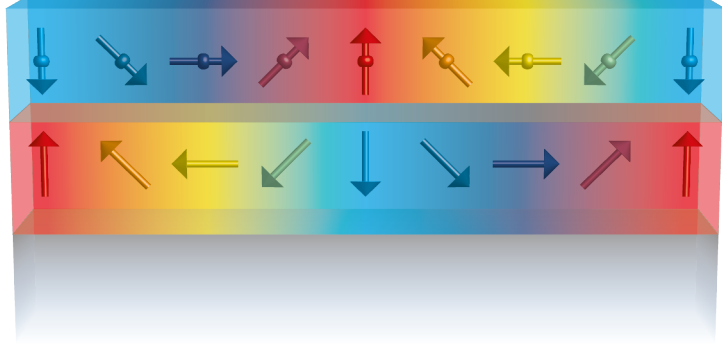


Figure 2.8.: Exchange-coupled domain wall in Co/Gd bi-layer. Chirality of domain wall induced from Co into Gd layer by (antiferromagnetic) exchange coupling. Different arrow style shall indicate distinct behavior of magnetic moments as discussed in section 2.1.5.2.

coupling like in Co-Gd systems. The exchange energy density for the DW given by equation (2.6) can be written as

$$\omega_J = -J_{\text{ex}} [\cos(\phi^L - \phi^U) \sin^2 \theta - \cos^2 \theta]. \quad (2.14)$$

2.2.3.5. Total domain wall energy of antiferromagnetic bi-layer

The two magnetic layers can be distinct in \mathbf{m}^L and \mathbf{m}^U . For each layer the temperature dependence can be different such that the variables $M_{S,T=0}^i$, T_C^i and ε^i defined in equation (2.3) can be different for each layer i . Furthermore, g^L and g^U could be distinct like it is the case for Co and Gd. Finally, also K_{cryst}^i and A_{ex}^i might be different for $i = U$ and L .

In order to calculate the DW energy, the energy densities acting on the DW will be integrated along x . Summing up the energies acting on the DW in one layer, the total DW energy density is given by

$$\omega_{\text{DW}} = \omega_A^L + \omega_A^U + \omega_{K_{\text{eff}}}^L + \omega_{K_{\text{eff}}}^U + \omega_{\text{DMI}}^L + \omega_{\text{DMI}}^U + \omega_J.$$

Inserting equations (2.9), (2.10), (2.12) and (2.14) yields

$$\begin{aligned} \omega_{\text{DW}} = & \frac{A_{\text{ex}}^L t^L}{\Delta^2} \sin^2 \theta + \frac{A_{\text{ex}}^U t^U}{\Delta^2} \sin^2 \theta \\ & + t^L K_{\text{eff}}^L \sin^2 \theta + t^U K_{\text{eff}}^U \sin^2 \theta \\ & \pm \frac{D^L}{\Delta} \cos \phi^L \sin \theta \mp \frac{D^U}{\Delta} \cos \phi^U \sin \theta \\ & - J_{\text{ex}} [\cos(\phi^L - \phi^U) \sin^2 \theta - \cos^2 \theta]. \end{aligned} \quad (2.15)$$

Since θ is a function of x , $\omega_{\text{DW}} = \omega_{\text{DW}}(x)$. To obtain the total DW energy of the bi-layer σ_{DW} , $\omega_{\text{DW}}(x)$ is integrated such that

$$\sigma_{\text{DW}} = \int_{-\infty}^{\infty} \omega_{\text{DW}}(x) dx.$$

Note that integrating $\omega_J(x)$ would yield a complicated analytical formula if $\Delta^L \neq \Delta^U$. However,

2. Theoretical foundations

due to the assumption $\Delta^L \approx \Delta^U$ the integral is simple.¹⁸ Utilizing the mathematical properties of the domain wall profile,¹⁹ σ_{DW} is given by

$$\begin{aligned}\sigma_{\text{DW}} &= \frac{2t^L}{\Delta} A_{\text{ex}}^L + \frac{2t^U}{\Delta} A_{\text{ex}}^U \\ &\quad + 2t^L \Delta K_{\text{eff}}^L + 2t^U \Delta K_{\text{eff}}^U \\ &\quad \pm \pi D^L \cos \phi^L \mp \pi D^U \cos \phi^U \\ &\quad - 2J_{\text{ex}} \Delta [1 + \cos(\phi^L - \phi^U)].\end{aligned}\tag{2.16}$$

Considering this static situation,²⁰ $\frac{d\sigma_{\text{DW}}}{d\phi^L} \stackrel{!}{=} 0$ and $\frac{d\sigma_{\text{DW}}}{d\phi^U} \stackrel{!}{=} 0$ results in

$$\phi^L \Big|_{\text{static}} = \begin{cases} \pi & \text{for } \uparrow\downarrow \text{ DW} \\ 0 & \text{for } \downarrow\uparrow \text{ DW} \end{cases} \quad \text{and} \quad \phi^U \Big|_{\text{static}} = \begin{cases} 0 & \text{for } \uparrow\downarrow \text{ DW} \\ \pi & \text{for } \downarrow\uparrow \text{ DW}. \end{cases}\tag{2.17}$$

Inserting these into equation (2.16) yields

$$\sigma_{\text{DW}} \Big|_{\text{static}} = \frac{2t^L}{\Delta} A_{\text{ex}}^L + \frac{2t^U}{\Delta} A_{\text{ex}}^U + 2t^L \Delta K_{\text{eff}}^L + 2t^U \Delta K_{\text{eff}}^U - \pi D^L - \pi D^U$$

for the total DW energy in the static case.

2.2.4. Domain wall width

In the section 2.2.2 the DW profile has been discussed. An important parameter of the DW profile, described by equation (2.8), is the DW width Δ . It reflects the length of the rotation of magnetization between two magnetic domains. Due to the strong coupling of the two magnetic layers, it is assumed that the DW width is the same in both layers $\Delta = \Delta^L = \Delta^U$. It can be calculated from equation (2.16) by $\frac{d\sigma_{\text{DW}}}{d\Delta} \stackrel{!}{=} 0$ which results in

$$\Delta = \sqrt{\frac{t^L A_{\text{ex}}^L + t^U A_{\text{ex}}^U}{t^L K_{\text{eff}}^L + t^U K_{\text{eff}}^U - J_{\text{ex}} [1 + \cos(\phi^L - \phi^U)]}}.$$

In the static case (equation (2.17)), the DW width is given by

$$\Delta \Big|_{\text{static}} = \sqrt{\frac{A_{\text{ex,bi-layer}}}{K_{\text{eff,bi-layer}}}}.\tag{2.18}$$

where $K_{\text{eff,bi-layer}} = \frac{t^L K_{\text{eff}}^L + t^U K_{\text{eff}}^U}{t^L + t^U}$ and $A_{\text{ex,bi-layer}} = \frac{t^L A_{\text{ex}}^L + t^U A_{\text{ex}}^U}{t^L + t^U}$. The intra-layer exchange and the effective anisotropy of both layers is added and normalized to the total layer thickness.

In the remainder of the present thesis formula (2.18) is used to describe the DW width also

¹⁸ If $\Delta^L \ll \Delta^U$ or $\Delta^L \gg \Delta^U$, $\int_{-\infty}^{\infty} \omega_J(x) dx = -\pi J_{\text{ex}} \cos(\phi^L - \phi^U) \min(\Delta^L, \Delta^U)$.

¹⁹ See section A.1 in appendix.

²⁰ Without any externally applied field or current and due to antiferromagnetic coupling ($J_{\text{ex}} < 0$).

for motion dynamics. The term $J_{\text{ex}} [1 + \cos(\phi^L - \phi^U)]$ does not contribute significantly and the dependence $\Delta(\phi^L, \phi^U)$ would result in complex dependencies which would make a theoretical discussion on an analytical basis complicated. This approach of using a static DW width is also used in the literature.²¹ Note that in [24] it was found that the DW width only varies slightly with temperature. Hence, $\Delta(T)$ is assumed to be constant.

2.3. Domain wall dynamics in ferrimagnetic bi-layer

In this section the equations of motion of a DW in a antiferromagnetically coupled bi-layer system are derived. First, the LANDAU–LIFSHITZ–GILBERT equation for a ferromagnetic layer is introduced. Afterwards, the RAYLEIGH-LAGRANGE equation is used to derive the equations of motion of a DW. Subsequently, the concept is extended to a ferrimagnetic bi-layer system. Finally, the DW motion is discussed in the context of temperature-dependent variation of the magnetization.

2.3.1. Landau–Lifshitz–Gilbert equation

In order to describe dynamics of magnetization in the presence of a magnetic field \mathbf{H} , it was early found that quantum theory leads to a macroscopic equation of motion given by²² [82–85]

$$\dot{\mathbf{m}} = -\gamma \mathbf{m} \times \mathbf{H} + \text{damping.}$$

This equation describes the observation that a magnetic moment \mathbf{m} would precess around a magnetic field \mathbf{H} by a frequency γ , and would eventually align along \mathbf{H} due to damping. The damping was expressed by LANDAU and LIFSHITZ [86] such that

$$\dot{\mathbf{m}} = -\gamma \mathbf{m} \times \mathbf{H} - \gamma \frac{\lambda}{m^2} \mathbf{m} \times (\mathbf{m} \times \mathbf{H}) \quad (2.19)$$

where λ is an adjustable damping parameter. This equation was finally expressed in a different way by GILBERT [37] who brought the equation to its most known form - the LANDAU–LIFSHITZ–GILBERT (LLG) equation²³

$$\dot{\mathbf{m}} = -\gamma \mathbf{m} \times \mathbf{H} + \frac{\alpha}{m} \mathbf{m} \times \dot{\mathbf{m}} \quad (2.20)$$

²¹ Cf. for example [9].

²² Note that \dot{X} is used as a short form of $\frac{dX}{dt}$.

²³ To transfer from equation (2.19) to equation (2.20), apply the cross product of \mathbf{m} to both sides which yields

$$\mathbf{m} \times \dot{\mathbf{m}} = -\gamma \mathbf{m} \times (\mathbf{m} \times \mathbf{H}) - \gamma \frac{\lambda}{m^2} \mathbf{m} \times [\mathbf{m} \times (\mathbf{m} \times \mathbf{H})].$$

This can be solved for $\mathbf{m} \times (\mathbf{m} \times \mathbf{H})$ which can finally be plugged into equation (2.19). λ is then substituted by $\lambda = \alpha m$ and terms in α^2 are neglected, as $\lambda \ll m$ [86].

2. Theoretical foundations

with the GILBERT damping parameter α . The literature is controversial about the temperature dependence of α but recent experiments on a GdFeCo layer show that the GILBERT damping parameter is temperature-independent around T_A [87]. Since this system is very similar to the Co/Gd bi-layer studied in the present thesis, α is assumed not to change with T .

Typically the spherical coordinates θ and ϕ are used to describe motion dynamics as it will be discussed in the next section 2.3.2. In these coordinate system the magnetization vector can be written as

$$\mathbf{m} = m \begin{pmatrix} \cos \phi \sin \theta \\ \sin \phi \sin \theta \\ \cos \theta \end{pmatrix}.$$

The time derivative is given by

$$\dot{\mathbf{m}} = \dot{m} \hat{\mathbf{m}} + m \dot{\theta} \hat{\boldsymbol{\theta}} + m \sin \theta \dot{\phi} \hat{\boldsymbol{\phi}}. \quad (2.21)$$

It is assumed that $\dot{m} = 0$. Hence the first term in equation (2.21) vanishes.

The LLG equation can also be applied to the energy terms discussed above as each energy term can be associated by an effective magnetic field

$$\mathbf{H}_{\text{eff}} = -\nabla_{\mathbf{m}} \omega = -\frac{1}{m} \frac{\partial \omega}{\partial \theta} \hat{\boldsymbol{\theta}} - \frac{1}{m} \frac{1}{\sin \theta} \frac{\partial \omega}{\partial \phi} \hat{\boldsymbol{\phi}}.$$

By inserting \mathbf{H}_{eff} into equation (2.20), the equations of motion of the magnetic moments - and subsequently also of the DW - could be derived. Here instead, the equations of motions of a DW will be deduce by a LAGRANGIAN approach [88] utilizing a RAYLEIGH dissipation function (see [89]) as it was originally proposed by GILBERT [37, 90].

2.3.2. Rayleigh-Lagrange equation

In order to obtain the equations of motion of a magnetic DW in a bi-layer system, the LAGRANGE equation of the second kind, given by

$$\frac{\partial L}{\partial X_i} - \frac{d}{dt} \frac{\partial L}{\partial \dot{X}_i} = 0,$$

is applied, where the generalized coordinates X_i include the degree of freedoms of the system [91]. In case of DW dynamics, X_i are given by the DW position q and magnetization's the azimuth angles ϕ^L and ϕ^U of the two magnetic layers. The LAGRANGIAN function L describes the difference of kinetic energy T and potential energy E of the system:

$$L = E - T.$$

While the potential energy E is given by the total DW energy σ_{DW}

$$E = \int_{-\infty}^{+\infty} \omega_{\text{DW}} dx = \sigma_{\text{DW}},$$

T is not uniquely determined [73].²⁴ In the scope of this thesis

$$T = - \int_{-\infty}^{+\infty} \frac{m}{\gamma} \sin \theta \dot{\theta} \phi dx = \pm 2 \frac{m}{\gamma} \phi \dot{\phi}$$

is used.

In case of non-conservative forces originating from damping (cf. equation (2.20)), RAYLEIGH added a dissipation function F . The RAYLEIGH-LAGRANGE equation is given by [89]:

$$\frac{\partial L}{\partial X_l} - \frac{d}{dt} \frac{\partial L}{\partial \dot{X}_l} - \frac{\partial F}{\partial \dot{X}_l} = 0. \quad (2.22)$$

To determine F , a dissipation potential P_{D} has to be found. Therefore, an analogous derivation to [73] is performed. The LLG equation (2.20) can be rewritten as

$$\dot{\mathbf{m}} = -\gamma \mathbf{m} \times \left(\mathbf{H}_{\text{eff}} - \underbrace{\frac{\alpha}{\gamma m} \dot{\mathbf{m}}}_{\mathbf{H}_{\text{D}}} \right) \quad (2.23)$$

where \mathbf{H}_{D} is a dissipation field. It is given by [73]

$$\mathbf{H}_{\text{D}} = \frac{\partial P_{\text{D}}}{\partial \dot{\mathbf{m}}}.$$

Consequently, P_{D} can be calculated by

$$P_{\text{D}} = \int \mathbf{H}_{\text{D}} d\dot{\mathbf{m}} = -\frac{\alpha}{2\gamma m} \dot{\mathbf{m}}^2 = -\frac{\alpha m}{2\gamma} \left(\dot{\phi}^2 \sin^2 \theta + \dot{\theta}^2 \right), \quad (2.24)$$

utilizing equation (2.21).

Lastly, the RAYLEIGH dissipation function F is given by

$$\begin{aligned} F &= \int_{-\infty}^{+\infty} P_{\text{D}} dx \\ &= - \int_{-\infty}^{+\infty} \frac{\alpha m}{2\gamma} \left(\dot{\phi}^2 \sin^2 \theta + \dot{\theta}^2 \right) dx \\ &= -\frac{\alpha m \Delta}{\gamma} \left(\dot{\phi}^2 + \frac{\dot{q}^2}{\Delta^2} \right). \end{aligned} \quad (2.25)$$

Inserting F and L into the RAYLEIGH-LAGRANGE equation (2.22) yields the equations of motion of a DW in a ferromagnetic layer. In the next section the here discussed concept is extended to a DW in a ferrimagnetic bi-layer.

²⁴ There are two possibilities: $T = - \int_{-\infty}^{+\infty} \frac{m}{\gamma} \cos \theta \dot{\phi} dx$ or $T = - \int_{-\infty}^{+\infty} \frac{m}{\gamma} \sin \theta \dot{\theta} \phi dx$ [73].

2. Theoretical foundations

Note that this derivation - equivalent to [73] - differs slightly to GILBERT's original version [90]. GILBERT did not use the dissipation potential P_D but simply squared $\dot{\mathbf{m}}$ and added a prefactor of $\frac{1}{2}$ (which is equivalent to RAYLEIGH's ansatz). He ended up at the same dissipation function (2.25). Therefore, the final results presented here and GILBERT's are equivalent. BOULLE ET AL. [92] extended GILBERT's approach to include effective driving terms. However, for adding effective driving terms or dry friction (discussed in sections 2.3.5 and 2.3.8, respectively) into F , simple squaring leads to incorrect solutions. The solutions can be verified by using the effective fields, instead of using the RAYLEIGH-LAGRANGE equation to obtain the equations of motion. It seems that the solutions of BOULLE ET AL. are only correct by chance. Note that using P_D to include effective driving terms and dry friction has no reference to any previous study.

2.3.3. Static solutions for ferrimagnetic bi-layer

As discussed in section 2.2.2, the DWs in the ferrimagnetic bi-layer system may act separately but only interact through their (strong) inter-layer exchange interaction. Hence, the kinetic energy is given by

$$\begin{aligned} T &= - \int_{-\infty}^{+\infty} \left(\frac{m^L}{\gamma^L} \phi^L + \frac{m^U}{\gamma^U} \phi^U \right) \dot{\theta} \sin \theta \, dx \\ &= \pm 2 \left(\frac{m^L}{\gamma^L} \phi^L - \frac{m^U}{\gamma^U} \phi^U \right) \dot{q}. \end{aligned}$$

The LAGRANGIAN function L for a ferrimagnetic bi-layer is

$$L = \sigma_{\text{DW}} \mp 2 \left(\frac{m^L}{\gamma^L} \phi^L - \frac{m^U}{\gamma^U} \phi^U \right) \dot{q}$$

with the total DW energy of the bi-layer system σ_{DW} as in equation (2.16). Equivalently, the RAYLEIGH dissipation function F for the bi-layer can be calculated:

$$\begin{aligned} F &= - \int_{-\infty}^{+\infty} \frac{\alpha^L m^L}{2\gamma^L} \left[(\dot{\phi}^L)^2 \sin^2 \theta + \dot{\theta}^2 \right] + \frac{\alpha^U m^U}{2\gamma^U} \left[(\dot{\phi}^U)^2 \sin^2 \theta + \dot{\theta}^2 \right] \, dx \\ &= - \frac{\alpha^L m^L \Delta}{\gamma^L} \left[(\dot{\phi}^L)^2 + \frac{\dot{q}^2}{\Delta^2} \right] - \frac{\alpha^U m^U \Delta}{\gamma^U} \left[(\dot{\phi}^U)^2 + \frac{\dot{q}^2}{\Delta^2} \right]. \end{aligned}$$

Plugging L and F into the RAYLEIGH-LAGRANGE equation (2.22) yields three motion equations

$X_l = q$:

$$\underbrace{0}_{\frac{\partial L}{\partial q}} \pm 2 \underbrace{\left(\frac{m^L}{\gamma^L} \dot{\phi}^L - \frac{m^U}{\gamma^U} \dot{\phi}^U \right)}_{-\frac{d}{dt} \frac{\partial L}{\partial \dot{q}}} + 2 \underbrace{\left(\frac{\alpha^L m^L}{\gamma^L} + \frac{\alpha^U m^U}{\gamma^U} \right) \frac{\dot{q}}{\Delta}}_{-\frac{\partial F}{\partial \dot{q}}} = 0 \quad (2.26a)$$

$X_l = \phi^L$:

$$\underbrace{\mp \pi D^L \sin \phi^L + 2 J_{\text{ex}} \Delta \sin(\phi^L - \phi^U)}_{\frac{\partial \sigma_{\text{DW}}}{\partial \phi^L}} \mp 2 \underbrace{\frac{m^L}{\gamma^L} \dot{q}}_{-\frac{\partial T}{\partial \phi^L}} + 0 \cdot \underbrace{\left(\frac{\alpha^L m^L \Delta}{\gamma^L} \dot{\phi}^L \right)}_{-\frac{\partial F}{\partial \phi^L}} = 0 \quad (2.26b)$$

$X_l = \phi^U$:

$$\underbrace{\pm \pi D^U \sin \phi^U - 2 J_{\text{ex}} \Delta \sin(\phi^L - \phi^U)}_{\frac{\partial \sigma_{\text{DW}}}{\partial \phi^U}} \pm 2 \underbrace{\frac{m^U}{\gamma^U} \dot{q}}_{-\frac{\partial T}{\partial \phi^U}} + 0 \cdot \underbrace{-\frac{d}{dt} \frac{\partial L}{\partial \dot{\phi}^U}}_{-\frac{d}{dt} \frac{\partial L}{\partial \dot{\phi}^U}} + 2 \underbrace{\frac{\alpha^U m^U \Delta}{\gamma^U} \dot{\phi}^U}_{-\frac{\partial F}{\partial \dot{\phi}^U}} = 0 \quad (2.26c)$$

where each is derived from one of the generalized coordinates q , ϕ^L and ϕ^U , respectively. In the remainder of this thesis, equations denoted by a, b or c shall indicate the corresponding equation of motion in respect to the generalized coordinates q , ϕ^L or ϕ^U .

2.3.3.1. Total angular momentum

As described in section 2.1.2, the gyromagnetic ratio γ^i is distinct for different materials. Consequently, also the dynamics of the magnetic moments described by the LLG equation (2.20) are different for each layer. The importance of the total angular momentum A^i of a layer i , instead of its magnetic moment m^i becomes visible by rewriting equations (2.26a), (2.26b), and (2.26c):

$X_l = q$:

$$\dot{q} = \frac{\Delta}{\alpha^L A^L + \alpha^U A^U} (\mp A^L \dot{\phi}^L \pm A^U \dot{\phi}^U)$$

$X_l = \phi^L$:

$$\dot{q} = \frac{\Delta}{A^L} \left[\pm \alpha^L A^L \dot{\phi}^L - J_{\text{DMI}}^L \sin \phi^L \pm J_{\text{ex}} \sin(\phi^L - \phi^U) \right]$$

$X_l = \phi^U$:

$$\dot{q} = \frac{\Delta}{A^U} \left[\mp \alpha^U A^U \dot{\phi}^U - J_{\text{DMI}}^U \sin \phi^U \pm J_{\text{ex}} \sin(\phi^L - \phi^U) \right]$$

where

$$J_{\text{DMI}}^i \stackrel{\text{def}}{=} \frac{\pi D^i}{2 \Delta}. \quad (2.28)$$

$J_{\text{DMI}} = J_{\text{DMI}}^L + J_{\text{DMI}}^U$ will be a useful quantity in case of large inter-layer exchange coupling ($J_{\text{ex}} \gg J_{\text{DMI}}$).

2.3.3.2. Steady state motion

Depending on the initial conditions, there will be motion of the magnetic moments. This motion is either in ϕ^i or q . For the given equations an equilibrium can be found for which $\dot{\phi}^L = \dot{\phi}^U = 0$. In the following, $\dot{\phi}^L = \dot{\phi}^U = 0$ is called steady state motion with a DW velocity \dot{q} . The velocity in the steady state regime is denoted by

$$v \stackrel{\text{def}}{=} \dot{q} \Big|_{\dot{\phi}^L = \dot{\phi}^U = 0} \quad (2.29)$$

2. Theoretical foundations

in the following, which will be later compared with the experimental data. That this comparison is valid, it needs to be assumed that $v = \frac{1}{t_p} \int_0^{t_p} \dot{q} dt$ where t_p is the pulse length of a current pulse to drive the DW. This assumption is valid if $\dot{\phi}^i$ converges to zero in a time much shorter than t_p . In analogy to [92], the settlement time of $\dot{\phi}^i$ in a ferrimagnetic bi-layer (with large inter-layer exchange coupling) can be calculated to be $t_\phi \approx \frac{A_{\text{net}}^2 + (\alpha^L A^L + \alpha^U A^U)^2}{(\alpha^L A^L + \alpha^U A^U) J_{\text{DMI}}}$. Hence, around angular momentum compensation, $t_\phi \approx \frac{\alpha^L A^L + \alpha^U A^U}{J_{\text{DMI}}}$. Inserting experimental values²⁵ yields $t_\phi \approx 1.5$ ps. In other words, the DW reaches the steady state regime within a few picoseconds. This is at least three orders of magnitude lower than the current pulse length of typically $t_p = 3 - 100$ ns.

For the given energy terms discussed so far (static solutions), the DW velocity in the steady state is

$$v \Big|_{\text{static}} = 0.$$

Consequently, the given energy terms do not lead to a continuous DW motion. Note that depending on the initial conditions of ϕ^L , ϕ^U , $\dot{\phi}^L$, $\dot{\phi}^U$, and \dot{q} , the DW could be displaced but will eventually stop moving.

Further, note that these equations converge to the stable state $\phi^L \Big|_{\text{static}} = \pi$ and $\phi^U \Big|_{\text{static}} = 0$ for a $\uparrow\downarrow$ DW and $\phi^L \Big|_{\text{static}} = 0$ and $\phi^U \Big|_{\text{static}} = \pi$ for a $\downarrow\uparrow$ DW. This shows that due to the DMI finally NÉEL DWs are formed. These results are in line with the results in equation (2.17).

There are several mechanisms to move a DW. In the following, it is discussed how the DW can be driven by an electrical current and by a magnetic field. While the field-driven case can be discussed using the same finding which were discussed so far, driving the DW by an electrical current needs an additional mechanisms which links the spins of the conduction electrons with the magnetic moments.

2.3.4. Field-driven domain wall motion

From a historical perspective the field-driven domain wall motion (FDDWM) was of major importance for example for the magnetic bubble memory [93]. Although this concept did not find any application, FDDWM is still of importance for example to understand the coercive field.

To achieve DW motion by an external magnetic field \mathbf{H}_{ext} , an additional energy term is needed. It is supposed to describe the reaction of the magnetic moments on an external field. This energy term is the ZEEMAN energy which is given by

$$\omega_{\text{Zeeman}}^i = -\mathbf{m}^i \cdot \mathbf{H}_{\text{ext}}.$$

The external magnetic field can be split into three components H_x , H_y and H_z . Thus,

$$\omega_{\text{Zeeman}}^i = -m^i (H_x \cos \phi^i \sin \theta + H_y \sin \phi^i \sin \theta + \zeta^i H_z \cos \theta).$$

where ζ^i is +1 or -1 for the lower or upper layer, respectively, as defined by equation (2.13).

²⁵ $D^{\text{Co}} = 0.2 \text{ pJ m}^{-1}$, $D^{\text{Gd}} = 0$, $\Delta = 2 \text{ nm}$, $\alpha^{\text{Co}} = \alpha^{\text{Gd}} = 0.1$ and $A^L = A^U = 2.3 \times 10^{-15} \text{ s J m}^{-2}$.

Adding ω_{Zeeman}^L and ω_{Zeeman}^U to ω_{DW} (equation (2.15)) then complements σ_{DW} to

$$\sigma_{\text{DW}} = -\Delta [H_x (m^L \cos \phi^L + m^U \cos \phi^U) \pi + H_y (m^L \sin \phi^L + m^U \sin \phi^U) \pi \mp (m^L - m^U) H_z q] + \text{terms of equation (2.16)}.$$

Solving the RAYLEIGH-LAGRANGE equation (2.22) including the ZEEMAN energy in L then leads to

$X_l = q$:

$$\dot{q} = \frac{\Delta}{\alpha^L A^L + \alpha^U A^U} \left[\mp A^L \dot{\phi}^L \pm A^U \dot{\phi}^U \pm (J_{H_z}^L - J_{H_z}^U) \right] \quad (2.30a)$$

$X_l = \phi^L$:

$$\dot{q} = \frac{\Delta}{A^L} \left[\pm \alpha^L A^L \dot{\phi}^L - J_{\text{DMI}}^L \sin \phi^L \pm J_{\text{ex}} \sin(\phi^L - \phi^U) \pm \left(J_{H_x}^L \sin \phi^L - J_{H_y}^L \cos \phi^L \right) \right] \quad (2.30b)$$

$X_l = \phi^U$:

$$\dot{q} = \frac{\Delta}{A^U} \left[\mp \alpha^U A^U \dot{\phi}^U - J_{\text{DMI}}^U \sin \phi^U \pm J_{\text{ex}} \sin(\phi^L - \phi^U) \mp \left(J_{H_x}^U \sin \phi^U - J_{H_y}^U \cos \phi^U \right) \right] \quad (2.30c)$$

with

$$\begin{aligned} J_{H_x}^i &\stackrel{\text{def}}{=} \frac{\pi}{2} m^i H_x \\ J_{H_y}^i &\stackrel{\text{def}}{=} \frac{\pi}{2} m^i H_y \\ J_{H_z}^i &\stackrel{\text{def}}{=} m^i H_z \end{aligned}$$

and J_{DMI}^i defined in equation (2.28).

The energy of J_{H_z} is directly transferred into DW motion as can be seen in equation (2.30a). The alignment of ϕ^i in steady state motion, where $\dot{\phi}^i = 0$, can be calculated by solving equations (2.30b) and (2.30c). For $H_x = H_y = 0$ and $J_{\text{ex}} \gg J_{\text{DMI}}$, there are solutions for ϕ^L and ϕ^U with $\dot{\phi}^L = \dot{\phi}^U = 0$ only if

$$H_z \leq H_W \stackrel{\text{def}}{=} \frac{\alpha^L A^L + \alpha^U A^U}{A_{\text{net}} m_{\text{net}}} J_{\text{DMI}} \quad (2.34)$$

where H_W is called the WALKER field for a ferrimagnetic bi-layer.²⁶ If $H_z > H_W$, the velocity starts to drop for increasing H_z because the energy, which is put into the system by the applied field, is not only transferred in the motion in x direction but also in a precession of the magnetization around ϕ^i . The drop of the velocity above the WALKER field is also known as the WALKER breakdown. To move the DW faster, the field needs to be much larger $H_z \gg H_W$. The fact that $H_W \sim 1/A_{\text{net}}$ can be used to determine T_A (defined in equation (2.7)), which is discussed in

²⁶ The WALKER field was first investigated for ferromagnetic structures [94].

2. Theoretical foundations

section 5.1.1 in more detail.

Applying an out-of-plane field $H_z \leq H_W$, leads to a DW velocity in the steady state regime

$$v = \pm \frac{\Delta (m^L - m^U)}{\alpha^L A^L + \alpha^U A^U} H_z. \quad (2.35)$$

In contrast, solely in-plane fields H_x and H_y will not lead to a steady state motion but could only displace the DW (very short distance). However, H_x and H_y can influence the DW velocity. The DW velocity dependence on H_x will be discussed in detail for current-induced domain wall motion later on as it turns out to be useful to determine the angular momentum compensation point in the experiments.

2.3.5. Current-induced domain wall motion

Current-induced domain wall motion (CIDWM) can be achieved by mainly two driving mechanisms. One is the volume spin transfer torque and the other is based on the spin HALL effect in an underlayer. Although the volume spin transfer torque has negligible influence on the final DW velocity compared to the spin HALL effect, spin transfer torque is also the underlying mechanism for the spin HALL effect driven domain wall motion. Therefore, it is discussed in the next section first.

2.3.5.1. Spin transfer torque

The spin transfer torque (STT) is an effect which is used in a lot of novel devices like the magnetic random access memory (MRAM) which has a high potential to become a commercial mass product. The basic concept of the MRAM is that a current flows through a (hard) magnetic layer, in which one kind of spins is dominant which makes the current spin polarized. Due to the STT the magnetization of a soft magnetic layer, whose magnetization can be switched easily, can be flipped by this spin polarized current. This special kind of torque is also called SLONCZEWSKI torque [95].

In general the STT describes the transfer of angular momentum from spins, which are transported by the electron current, to the magnetic moments of the magnetic layer [96]. The exchange interaction responsible for the coupling is the s - d exchange interaction which describes the interaction between the moving sp conduction electrons and the relatively localized $3d$ electrons [97, 98]. Due to STT also a DW in a nanowire can be moved.

There are two different kinds of torques which result from this spin current. On one hand the so-called adiabatic STT

$$\begin{aligned} \tau_{\text{aSTT}}^i &= -b_j^i \hat{\mathbf{m}}^i \times \hat{\mathbf{m}}^i \times (\mathbf{j}^i \cdot \nabla) \hat{\mathbf{m}}^i \\ &= b_j^i j^i \frac{\partial \hat{\mathbf{m}}^i}{\partial x} \\ &= \pm \zeta^i b_j^i j^i \frac{\sin \theta}{\Delta} \hat{\boldsymbol{\theta}}, \end{aligned}$$

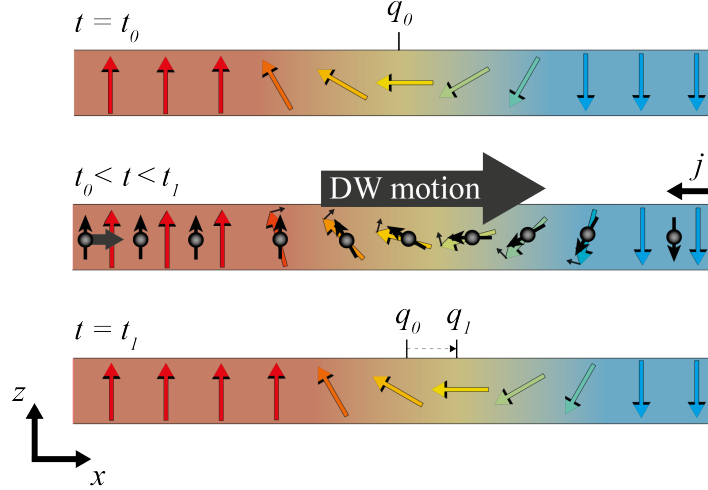


Figure 2.9.: Illustration of spin transfer torque driven domain wall motion.

At time $t = t_0$, DW at position q_0 . At $t_0 < t < t_1$ electrical current flowing in $-x$ direction applied. Due to the spin polarized electron flow, DW can be moved in the same direction as electron flow by STT. At $t = t_1$ DW has moved to position q_1 . Note that motion into electron flow direction is independent on $\uparrow\downarrow$ or $\downarrow\uparrow$ DW.

where $\mathbf{j}^i = j^i \hat{\mathbf{x}}$ is the electrical current density flowing in the magnetic layer i in x direction and b_j^i is the adiabatic STT coefficient. The latter was determined by BERGER [4] and is given by

$$b_j^i = \frac{\hbar P^i}{2 e A^i} t^i$$

with P^i the conduction electron spin polarization. Note that the b_j^i includes t^i because the STT, discussed here, is an effect inside the volume of layer i .

The adiabatic STT is depicted in Figure 2.9. First ($t = t_0$) the DW is at position q_0 . Then, an electrical current is applied in $-x$ direction. The spin-polarized electrons are moving in x direction and “hit” the DW. Due to the gradient of the localized magnetic moments along x , the spin angular momentum is forced to change too, and will create a torque which rotates the relatively localized moments in $\hat{\boldsymbol{\theta}}$ direction. The DW starts moving in x direction and will stop as soon as the current is turned off ($t = t_1$). The direction of motion is independent of the type of the wall and is always in electron flow direction.

On the other hand, there is a non-adiabatic STT

$$\begin{aligned} \boldsymbol{\tau}_{\text{naSTT}}^i &= -\beta^i b_j^i \hat{\mathbf{m}}^i \times (\mathbf{j}^i \cdot \nabla) \hat{\mathbf{m}}^i \\ &= -\beta^i b_j^i j^i \hat{\mathbf{m}}^i \times \frac{\partial \hat{\mathbf{m}}^i}{\partial x} \\ &= \mp \zeta^i \beta^i b_j^i j^i \frac{\sin \theta}{\Delta} \hat{\boldsymbol{\phi}}. \end{aligned}$$

β^i is the dimensionless non-adiabatic STT coefficient which gives the ratio of the non-adiabatic

2. Theoretical foundations

to the adiabatic STT.

In the reminder of this thesis it is assumed that the current density is uniformly distributed in all layers. Consequently, $j = j^i$. Often the quantity

$$u^i \stackrel{\text{def}}{=} b_j^i j$$

is used. u^i has the unit of a velocity and is equal to the velocity of a DW if only STT was considered.

SLONCZEWSKI showed that both STT terms can be added to the LLG equation (2.20) such that [95]

$$\frac{d\hat{\mathbf{m}}^i}{dt} = -\gamma^i \hat{\mathbf{m}}^i \times \mathbf{H}_{\text{eff}}^i + \frac{\alpha^i}{m^i} \hat{\mathbf{m}}^i \times \dot{\mathbf{m}}^i + \boldsymbol{\tau}_{\text{aSTT}}^i + \boldsymbol{\tau}_{\text{naSTT}}^i. \quad (2.36)$$

In order to derive the equations of motion, the same approach is used as for the damping in equation (2.23). Analogously, equation (2.36) can be rewritten to

$$\frac{d\hat{\mathbf{m}}^i}{dt} = -\gamma^i \hat{\mathbf{m}}^i \times \left(\mathbf{H}_{\text{eff}}^i + \mathbf{H}_{\text{D}}^i \pm \underbrace{\frac{\zeta^i u^i \sin \theta}{\gamma^i} \frac{\sin \theta}{\Delta} \hat{\boldsymbol{\phi}} \pm \frac{\zeta^i \beta^i u^i \sin \theta}{\gamma^i} \frac{\sin \theta}{\Delta} \hat{\boldsymbol{\theta}}}_{\mathbf{H}_{\text{STT}}^i} \right)$$

with an effective STT driving field $\mathbf{H}_{\text{STT}}^i$.

Equivalently to equation (2.24), a dynamic energy can be attributed to this field. This approach analogously follows the derivation of the dissipation potential in [73]. The energy created by the STT acting on the DW is then given by

$$\begin{aligned} P_{\text{STT}} &= \int \mathbf{H}_{\text{STT}}^{\text{L}} d\dot{\mathbf{m}}^{\text{L}} + \int \mathbf{H}_{\text{STT}}^{\text{U}} d\dot{\mathbf{m}}^{\text{U}} \\ &= \mathbf{H}_{\text{STT}}^{\text{L}} \cdot \dot{\mathbf{m}}^{\text{L}} + \mathbf{H}_{\text{STT}}^{\text{U}} \cdot \dot{\mathbf{m}}^{\text{U}} \\ &= \pm u^{\text{L}} A^{\text{L}} \frac{\sin^2 \theta}{\Delta} \dot{\phi}^{\text{L}} \mp u^{\text{U}} A^{\text{U}} \frac{\sin^2 \theta}{\Delta} \dot{\phi}^{\text{U}} \\ &\quad - \beta^{\text{L}} u^{\text{L}} A^{\text{L}} \frac{\sin^2 \theta}{\Delta^2} \dot{q} - \beta^{\text{U}} u^{\text{U}} A^{\text{U}} \frac{\sin^2 \theta}{\Delta^2} \dot{q} \end{aligned} \quad (2.37)$$

using $\dot{\mathbf{m}}^i = \mp m^i \zeta^i \sin \theta \frac{\dot{q}}{\Delta} \hat{\boldsymbol{\theta}} + m^i \sin \theta \dot{\phi} \hat{\boldsymbol{\phi}}$. P_{STT} can be included in F by integrating $F = \int_{-\infty}^{+\infty} P_{\text{D}} + P_{\text{STT}} dx$ like in equation (2.25).

The effect of volume STT is of minor importance for CIDWM in the magnetic multilayers discussed in the present thesis. This is manifested in the DW driving direction which is observed to be into electrical current flow direction instead of electron flow direction, as it would be for STT. The actually more efficient driving mechanism is based on the spin HALL effect which is discussed in the next section.

2.3.5.2. Spin Hall effect

The spin HALL effect (SHE) is an effect which describes a separation of spin-up and spin-down electrons in a paramagnetic metal, like Pt, induced by an electrical current [99]. The separation of the spins is analogous to the HALL voltage where positive and negative charges are separated orthogonal to the current flow and magnetic field. The difference to the HALL effect is that no magnetic field is needed to create the spin separation. Instead effects inside the material are the cause of this behavior. These can be distinguished between intrinsic and extrinsic effects, which lead to an the intrinsic and extrinsic SHE. In general the material needs spin-orbit coupling in order to create any SHE. The intrinsic SHE then arises from a splitting of the band structure due to spin-orbit coupling and an effective magnetic field caused by the BERRY phase [100, 101]. The extrinsic SHE originates from scattering of the conduction electrons at impurities. Due to the electrical potential of the latter, which in turn looks like a magnetic field in the rest frame of the moving electrons, the spins are separated [99, 102].²⁷ An important parameter of the SHE is the spin HALL angle θ_{SH} . It gives the ratio of the spin current, which is created by the current, and the current. Depending on the material it can be positive, like for Pt [103, 104], or negative, like for Ta [104, 105].

In order to include the SHE into the model, consider a setup like it is shown in Figure 2.10. A Co layer is grown on top of a Pt layer in the x - y plane. In the Pt layer the SHE appears due to large spin-orbit coupling [99, 103, 104, 106] and the spin HALL angle is positive [103, 104]. The current density in the Pt underlayer \mathbf{j}^{UL} is for instance flowing in x direction and thus the electron current \mathbf{j}_e^{UL} is flowing in $-x$ direction. The resulting spin current²⁸ which flows in z direction is then given by

$$\mathbf{s} = \frac{\hbar \theta_{\text{SH}}}{2e} (\mathbf{j}^{\text{UL}} \times \hat{\mathbf{z}})$$

with the elementary charge e . E.g. the spin current is polarized in $-y$ direction for positive and $+y$ direction for negative currents for $\theta_{\text{SH}} > 0$ like in Pt. Note that \mathbf{j}^{UL} might differ from the overall \mathbf{j} in the layer stack. However, this was not examined in the context of this thesis. Therefore, $\mathbf{j} = \mathbf{j}^{\text{UL}}$ is used.

The spin polarized electrons defuse into the two magnetic layers of the ferrimagnetic bi-layer. This spin current acts like a SLONCZEWSKI torque on the magnetization in layer i [103, 107]. Therefore, the magnetic moments in both layers cant into the direction of \mathbf{s} . The magnitude of the torque might differ in the two layers. To account for the difference of the two layers, an effective spin Hall angle θ_{SH}^i is used which describes the ratio of the spin current \mathbf{s}^i in magnetic layer i (contributing to the torque) to the conventional current flowing through the Pt underlayer. It is assumed that the effective spin Hall torque in the Gd layer is close to zero ($\theta_{\text{SH}}^{\text{Gd}} \approx 0$) since it is well known that current interacts little with $4f$ magnetic moments [108, 109].

²⁷ For further information see for example [101] or [99].

²⁸ Unit: spin angular momentum per second.

2. Theoretical foundations

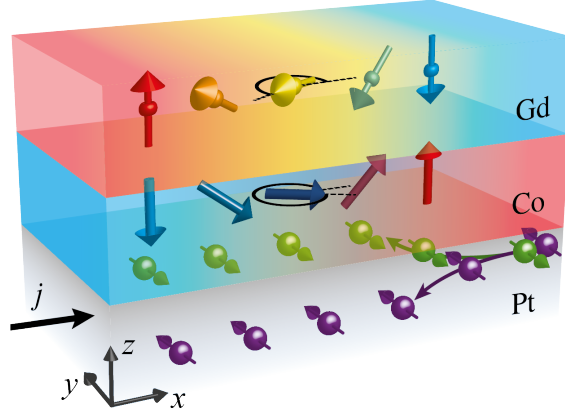


Figure 2.10.: Spin Hall effect creating torque in magnetic moments in bi-layer. An electrical current is applied in x direction which corresponds to an electron flow in $-x$ direction. Due to the SHE in the Pt layer, the spins in $+y$ and $-y$ direction are separated in z direction. This creates a spin current, polarized in \mathbf{s} direction, flowing into the Co layer. \mathbf{s} causes a SLONCZEWSKI torque which acts on the magnetization. A field \mathbf{H}_{SHE} can be associated with this torque which points in $\hat{\mathbf{e}}_M \times \mathbf{s}$ direction.

An effective field \mathbf{H}_{SH}^i can be defined which is given by

$$\mathbf{H}_{\text{SH}}^i = \frac{1}{m^i} (\hat{\mathbf{m}}^i \times \mathbf{s}^i) = H_{\text{SH}}^i \left(\cos \phi^i \hat{\boldsymbol{\theta}} - \zeta^i \cos \theta \sin \phi^i \hat{\boldsymbol{\phi}} \right)$$

where $H_{\text{SH}}^i = \frac{\hbar \theta_{\text{SH}}^i j}{2em^i}$. Note that this field would be zero if a BLOCH DW was assumed. Thus, a motion due to the SHE is only possible for NÉEL DWs which in turn can be created if a strong DMI is taken into account.

The spin HALL torque is then given by

$$\begin{aligned} \boldsymbol{\tau}_{\text{SH}}^i &= -\gamma^i \hat{\mathbf{m}}^i \times \mathbf{H}_{\text{SH}}^i \\ &= -\gamma^i H_{\text{SH}}^i \left(\zeta^i \cos \theta \sin \phi^i \hat{\boldsymbol{\theta}} + \cos \phi^i \hat{\boldsymbol{\phi}} \right). \end{aligned}$$

Analogously to the STT terms, the SHE term can be added to the LLG equation (2.20) such that

$$\begin{aligned} \frac{d\hat{\mathbf{m}}^i}{dt} &= -\gamma^i \hat{\mathbf{m}}^i \times \mathbf{H}_{\text{eff}}^i + \frac{\alpha^i}{m^i} \hat{\mathbf{m}}^i \times \dot{\mathbf{m}}^i + \boldsymbol{\tau}_{\text{aSTT}}^i + \boldsymbol{\tau}_{\text{naSTT}}^i + \boldsymbol{\tau}_{\text{SH}}^i \\ &= -\gamma^i \hat{\mathbf{m}}^i \times \left(\mathbf{H}_{\text{eff}}^i + \mathbf{H}_{\text{D}}^i + \mathbf{H}_{\text{STT}}^i + \mathbf{H}_{\text{SH}}^i \right). \end{aligned}$$

Following the same approach to derive P_{SH} as for STT in equation (2.37), this yields

$$\begin{aligned}
 P_{\text{SH}} &= \int \mathbf{H}_{\text{SH}}^{\text{L}} d\mathbf{m}^{\text{L}} + \int \mathbf{H}_{\text{SH}}^{\text{U}} d\mathbf{m}^{\text{U}} \\
 &= \mathbf{H}_{\text{SH}}^{\text{L}} \cdot \mathbf{m}^{\text{L}} + \mathbf{H}_{\text{SH}}^{\text{U}} \cdot \mathbf{m}^{\text{U}} \\
 &= m^{\text{L}} H_{\text{SH}}^{\text{L}} \left(\mp \cos \phi^{\text{L}} \sin \theta \frac{\dot{q}}{\Delta} - \sin \phi^{\text{L}} \cos \theta \sin \theta \dot{\phi}^{\text{L}} \right) \\
 &\quad + m^{\text{U}} H_{\text{SH}}^{\text{U}} \left(\pm \cos \phi^{\text{U}} \sin \theta \frac{\dot{q}}{\Delta} + \sin \phi^{\text{U}} \cos \theta \sin \theta \dot{\phi}^{\text{U}} \right).
 \end{aligned}$$

P_{SH} can be included in F like for STT by integrating $F = \int_{-\infty}^{+\infty} P_{\text{D}} + P_{\text{STT}} + P_{\text{SH}} dx$.

2.3.5.3. Dynamic solutions

Considering P_{STT} and P_{SH} , F results in

$$\begin{aligned}
 F &= -\frac{\alpha^{\text{L}} m^{\text{L}} \Delta}{\gamma^{\text{L}}} \left[\left(\dot{\phi}^{\text{L}} \right)^2 + \frac{\dot{q}^2}{\Delta^2} \right] - \frac{\alpha^{\text{U}} m^{\text{U}} \Delta}{\gamma^{\text{U}}} \left[\left(\dot{\phi}^{\text{U}} \right)^2 + \frac{\dot{q}^2}{\Delta^2} \right] \\
 &\quad \pm 2 u^{\text{L}} A^{\text{L}} \dot{\phi}^{\text{L}} \mp 2 u^{\text{U}} A^{\text{U}} \dot{\phi}^{\text{U}} - 2 \beta^{\text{L}} u^{\text{L}} A^{\text{L}} \frac{\dot{q}}{\Delta} - 2 \beta^{\text{U}} u^{\text{U}} A^{\text{U}} \frac{\dot{q}}{\Delta} \\
 &\quad \mp \pi m^{\text{L}} H_{\text{SH}}^{\text{L}} \cos \phi^{\text{L}} \dot{q} \pm \pi m^{\text{U}} H_{\text{SH}}^{\text{U}} \cos \phi^{\text{U}} \dot{q}.
 \end{aligned}$$

Solving the RAYLEIGH-LAGRANGE equation (2.22) including the ZEEMAN energy in L then leads to

$X_l = q$:

$$\begin{aligned}
 \dot{q} &= \frac{\Delta}{\alpha^{\text{L}} A^{\text{L}} + \alpha^{\text{U}} A^{\text{U}}} \left[\mp A^{\text{L}} \dot{\phi}^{\text{L}} \pm A^{\text{U}} \dot{\phi}^{\text{U}} \pm (J_{\text{H}_z}^{\text{L}} - J_{\text{H}_z}^{\text{U}}) \right. \\
 &\quad \left. - \beta^{\text{L}} J_{\text{STT}}^{\text{L}} - \beta^{\text{U}} J_{\text{STT}}^{\text{U}} \right. \\
 &\quad \left. \mp (J_{\text{SH}}^{\text{L}} \cos \phi^{\text{L}} - J_{\text{SH}}^{\text{U}} \cos \phi^{\text{U}}) \right]
 \end{aligned} \tag{2.38a}$$

$X_l = \phi^{\text{L}}$:

$$\begin{aligned}
 \dot{q} &= \frac{\Delta}{A^{\text{L}}} \left[\pm \alpha^{\text{L}} A^{\text{L}} \dot{\phi}^{\text{L}} - J_{\text{DMI}}^{\text{L}} \sin \phi^{\text{L}} \pm J_{\text{ex}} \sin (\phi^{\text{L}} - \phi^{\text{U}}) \right. \\
 &\quad \left. \pm (J_{\text{H}_x}^{\text{L}} \sin \phi^{\text{L}} - J_{\text{H}_y}^{\text{L}} \cos \phi^{\text{L}}) - J_{\text{STT}}^{\text{L}} \right]
 \end{aligned} \tag{2.38b}$$

$X_l = \phi^{\text{U}}$:

$$\begin{aligned}
 \dot{q} &= \frac{\Delta}{A^{\text{U}}} \left[\mp \alpha^{\text{U}} A^{\text{U}} \dot{\phi}^{\text{U}} - J_{\text{DMI}}^{\text{U}} \sin \phi^{\text{U}} \pm J_{\text{ex}} \sin (\phi^{\text{L}} - \phi^{\text{U}}) \right. \\
 &\quad \left. \mp (J_{\text{H}_x}^{\text{U}} \sin \phi^{\text{U}} - J_{\text{H}_y}^{\text{U}} \cos \phi^{\text{U}}) - J_{\text{STT}}^{\text{U}} \right]
 \end{aligned} \tag{2.38c}$$

where

$$\begin{aligned}
 J_{\text{SH}}^i &\stackrel{\text{def}}{=} \frac{\pi}{2} s^i = \frac{\pi}{2} m^i H_{\text{SH}}^i = \frac{\pi}{2} \frac{\hbar \theta_{\text{SH}}^i j}{2e} \\
 J_{\text{STT}}^i &\stackrel{\text{def}}{=} u^i \frac{A^i}{\Delta}
 \end{aligned}$$

2. Theoretical foundations

and J_{DMI} , J_{H_x} , J_{H_y} , and J_{H_z} defined in equations (2.28), (2.31), (2.32), and (2.33), respectively. The unit of J^i is $[J^i] = \text{J m}^{-2}$. Note that $J_{\text{SH}} = J_{\text{SH}}^{\text{L}} + J_{\text{SH}}^{\text{U}}$ will be useful in case of the limit of very large J_{ex} where $J_{\text{ex}} \gg J_{\text{DMI}}$ and $J_{\text{ex}} \gg J_{\text{SH}}$.

2.3.5.4. Domain wall mobility

The main driving force in case of CIDWM is the SHE. By using experimental values it can be shown that the contribution of volume STT to CIDWM is about much smaller than the contribution of SHE [72]. Hence, in the following the STT will no longer be considered.

The domain wall mobility ϖ is an important measure to quantify the response of the DW in terms of DW velocity on the applied current density. It can be defined by

$$\varpi(j) \stackrel{\text{def}}{=} \frac{d\langle \dot{q} \rangle}{dj}. \quad (2.41)$$

where $\langle \dot{q} \rangle$ denotes a time-averaged velocity. There are three factors determining ϖ : 1) material parameters, 2) torque efficiency, and 3) dissipation in angular rotation $\dot{\phi}^i$.²⁹ In case of steady state motion, the latter is zero by definition and $\langle \dot{q} \rangle = v$ as discussed in section 2.3.3.2 with v being the steady state velocity (cf. equation (2.29)).³⁰

If the assumption of very large inter-layer exchange coupling is considered, such that $\phi^{\text{U}} \approx \pi - \phi^{\text{L}}$, the steady state velocity of the DW for CIDWM for all ratios of A^{U} to A^{L} is given by³¹

$$v \approx \left\{ \left[\frac{A^{\text{U}} - A^{\text{L}}}{\frac{\pi}{2} (D^{\text{L}} + D^{\text{U}})} \right]^2 + \left[\frac{A^{\text{U}} \alpha^{\text{U}} + A^{\text{L}} \alpha^{\text{L}}}{\Delta (J_{\text{SH}}^{\text{U}} + J_{\text{SH}}^{\text{L}})} \right]^2 \right\}^{-\frac{1}{2}} \text{sgn}(j). \quad (2.42)$$

It is important to note at this point that the approximations of ϕ^{L} and ϕ^{U} used here are too rough to draw conclusions about the velocity dependence on any H_x field. Hence, the H_x dependence of v will be discussed in more depth in section 2.3.7.

Comparing these results to FDDWM [110], it can be found that at angular momentum compensation ($A^{\text{L}} = A^{\text{U}}$) the DW can be driven at the same speed by an external out-of-plane field

$$H_z = \frac{\pi H_{\text{SH,total}}^{\text{L}}}{2 \left(1 - \frac{\gamma^{\text{U}}}{\gamma^{\text{L}}} \right)}$$

with $H_{\text{SH,total}}^{\text{L}} = \frac{\hbar j}{2m^{\text{L}}e} (\theta_{\text{SH}}^{\text{L}} + \theta_{\text{SH}}^{\text{U}})$. This highlights the mobility differences of field-driven DW motion and CIDWM at $A^{\text{L}} = A^{\text{U}}$. Particularly, if γ^{U} is close to γ^{L} , a much larger H_z is required to achieve the same DW velocity as for CIDWM. Especially in case of SAF structures, for which angular momentum compensation is equal to magnetic moment compensation, the DW cannot

²⁹ Dissipation by threshold current leads to $\langle \dot{q} \rangle = 0$. The energy is effectively transferred into $\dot{\phi}^i$ leading to dissipation.

³⁰ In steady state motion, ϖ is zero for currents below the threshold current, discussed in section 2.3.8. In order to describe the effect of threshold current on DW motion, the efficiency ϵ will be used (section 2.3.8.3).

³¹ The same equation can be obtained by an effective quantity approach [23, 24]. This is shown in section A.2 in the appendix.

be moved by any H_z but instead can be very efficiently moved by a spin Hall current.

2.3.6. Exchange coupling torque

Considering the origin of the torque mechanisms is key to understand and improve the efficiency of DW motion. DW motion is efficient if no energy dissipates, for example into $\dot{\phi}$, and the input energy is converted efficiently into kinetic energy of the DW by torques acting on the magnetic moments. The mechanisms of FDDWM and CIDWM are both originating from the combination of two torques. First, a torque creating a rotation of the magnetization in $\hat{\phi}$ direction and second, a torque creating a rotation in $\hat{\theta}$ direction. Only the latter finally leads to the desired motion of the DW. This is because in a material with perpendicular magnetic anisotropy a driving torque needs to turn the magnetic moments inside the DW from an in-plane to an out-of-plane state.

In case of ferromagnetic layers, a $\hat{\phi}$ -torque can be generated, for instance, by an external field H_z , resulting in a torque $\tau_{H_z} = -\gamma \hat{\mathbf{m}} \times \mathbf{H}_z$. The same applies for the torque generated by the spin current \mathbf{s} which is $\tau_{\text{SH}} = -\gamma \hat{\mathbf{m}} \times (\hat{\mathbf{m}} \times \frac{\mathbf{s}}{m})$. Due to the rotation into $\hat{\phi}$, the DMI energy is no longer at minimum. This causes the appearance of an effective DMI field \mathbf{H}_{DMI} which points along x (as discussed in section 2.2.3.3). This DMI field then creates the required $\hat{\theta}$ -torque $\tau_{\text{DMI}} = -\gamma \hat{\mathbf{m}} \times \mathbf{H}_{\text{DMI}}$ which leads to a motion of the DW.³² For CIDWM this driving mechanism is called spin-orbit torque or chiral spin torque (CST) which represents the combination of SHE torque with DMI torque [8, 72, 111].

The exchange coupling torque (ECT) mechanism in antiferromagnetically coupled systems is similar to the CST. For CIDWM, the $\hat{\phi}$ -torque created by the SHE is the same, but the $\hat{\theta}$ -torque originates from the exchange coupling of two magnetic sublattices. This combined mechanism for CIDWM was first described by YANG ET AL. [9]. The ECT is illustrated in Figure 2.11. If $A^L \approx A^U$, the magnetic moments in the upper and lower magnetic layer are canted towards the same direction due to the SHE. Hence, \mathbf{m}^L is no longer antiparallel to \mathbf{m}^U . This, in turn, leads to the creation of an effective exchange field \mathbf{H}_{ex}^i due to the inter-layer exchange interaction. This effective exchange field is given by

$$\mathbf{H}_{\text{ex}}^i = -\zeta^i \frac{J_{\text{ex}}}{m^i} \sin(\phi^L - \phi^U) \hat{\phi}.$$

Consequently, \mathbf{H}_{ex}^i creates the ECT

$$\tau_{\text{ex}}^i = -\gamma^i \hat{\mathbf{m}}^i \times \mathbf{H}_{\text{ex}}^i = -\zeta^i \frac{J_{\text{ex}}}{A^i} \sin(\phi^L - \phi^U) \hat{\theta} \quad (2.43)$$

which acts on the magnetic moment in layer i .

An electrical current in x ($-x$) direction will lead to a spin current in $-y$ (y) direction. Therefore, the magnetic moments will cant such that $\phi^L - \phi^U \gtrless 0$ ($\phi^L - \phi^U \lesseqgtr 0$). Consequently,

³² In case of FDDWM without DMI, a driving torque can also be generated secondarily by the damping term of LLG equation (2.20). However, similarly to STT this has a minor contribution to the final DW velocity.

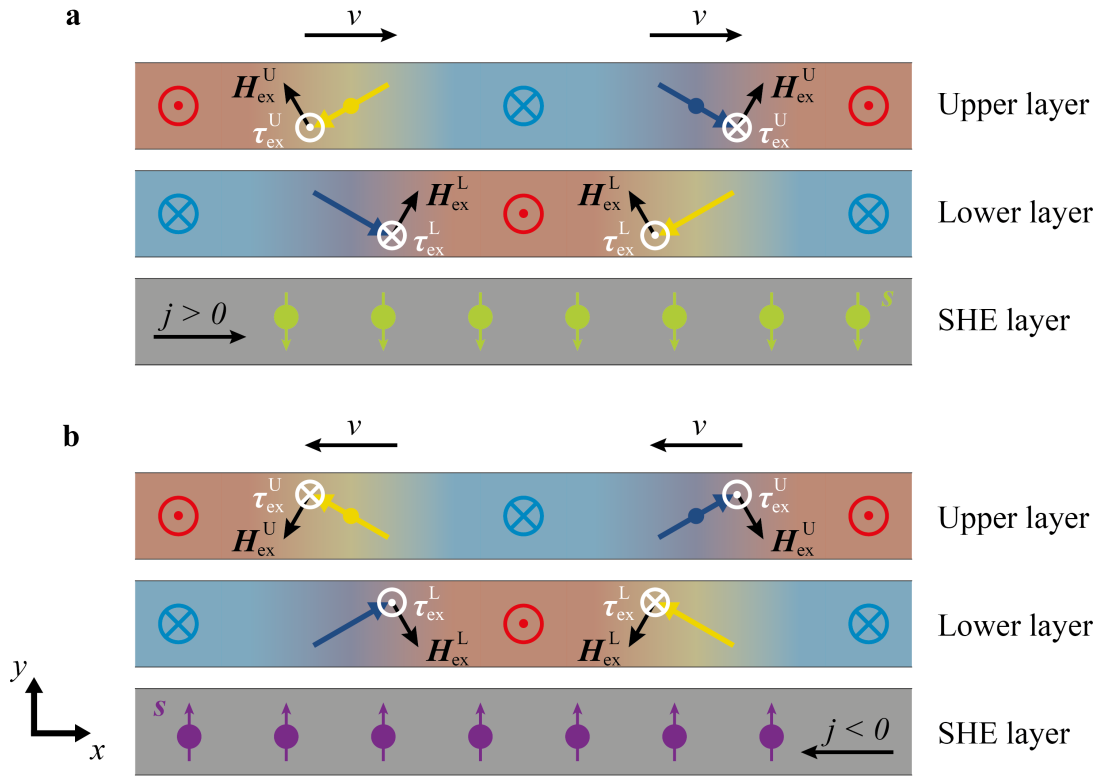


Figure 2.11.: Illustration of exchange coupling torque. Top view onto upper and lower magnetic layer, as well as onto underlayer exhibiting SHE. Spin polarized current s flowing into magnetic layers, creating ECT $\tau_{\text{ex}}^{\text{U}}$ and $\tau_{\text{ex}}^{\text{L}}$ due to exchange field H_{ex}^{L} and H_{ex}^{U} in upper and lower layer, respectively. **a**, Positive current density creating spin current in underlayer with SHE, polarized in $-y$ direction. **b**, Negative current density creating spin current, polarized in $+y$ direction. In both cases, subsequent DWs move into current flow direction.

τ_{ex}^i creates a DW motion in current flow direction in both magnetic layers. The DW motion for positive and negative current densities is shown in Figure 2.11a and b, respectively.

In order to show which torque contributes by which amount to the final DW velocity, $\dot{\phi}^L$ defined by equation (2.38b) and $\dot{\phi}^U$ defined by equation (2.38c) can be plugged into equation (2.38a) which results in

$$\begin{aligned}
 v = \frac{\Delta}{\frac{(1+\alpha^L)^2 A^L}{\alpha^L} + \frac{(1+\alpha^U)^2 A^U}{\alpha^U}} & \left[\pm \left(\frac{J_{\text{ex}}}{\alpha^L} + \frac{J_{\text{ex}}}{\alpha^U} \right) \sin(\phi^L - \phi^U) \right. \\
 & - \left(\frac{J_{\text{DMI}}^L}{\alpha^L} \sin \phi^L + \frac{J_{\text{DMI}}^U}{\alpha^U} \sin \phi^U \right) \\
 & \mp \left(J_{\text{SH}}^L \cos \phi^L - J_{\text{SH}}^U \cos \phi^U \right) \\
 & \pm \left(\frac{J_{\text{H}_x}^L}{\alpha^L} \sin \phi^L - \frac{J_{\text{H}_x}^U}{\alpha^U} \sin \phi^U \right) \\
 & \mp \left(\frac{J_{\text{H}_y}^L}{\alpha^L} \cos \phi^L - \frac{J_{\text{H}_y}^U}{\alpha^U} \cos \phi^U \right) \\
 & \left. \pm \left(J_{\text{H}_z}^L - J_{\text{H}_z}^U \right) \right] \tag{2.44}
 \end{aligned}$$

for given values of ϕ^L and ϕ^U . In this form, each term corresponds to the velocity contribution by the respective $\hat{\theta}$ -torque to the overall DW velocity. Note that in cases where $A^L \gg A^U$ or $A^L \ll A^U$, the CST, implicitly expressed by the terms of J_{DMI}^L and J_{DMI}^U , can become more relevant than the ECT because in these cases the bi-layer rather acts as a single ferromagnetic layer.

2.3.7. Influence of H_x on current-induced domain wall motion

When talking about H_x dependence, the velocity dependence as a function of an field H_x symmetric around $H_x = 0$ is meant. As it was shown in [9], the DW velocity dependence on H_x in SAF structures is very different to that of single magnetic layers, shown in [72]. In the experiment of the thesis at hand it has been measured that at a temperature $T_{\xi=0}$, a linear fit to the v vs. H_x curves results in a slope $\xi = 0$. Thus, in other words, at this certain temperature there is no dependence of the DW velocity on H_x . In the following, it is discussed why v has no dependence on H_x at a certain ratio $\frac{A^U}{A^L} \Big|_{\xi=0}$. It is shown that $\frac{A^U}{A^L} \Big|_{\xi=0}$ is clearly above magnetic moment compensation and instead close to angular momentum compensation.

Many studies presume that the effective DMI diverges at T_M [17–19, 23, 24, 26]. But does this imply an independence of v on H_x at T_M ? That the effective DMI diverges at T_M seems correct if large exchange coupling is assumed: If H_x terms were included in equation (2.42), it would read as (the following approximation is very rough!)

$$v \stackrel{\xi}{\approx} \Delta \left\{ \left[\frac{(A^U - A^L)}{(J_{\text{DMI}} \mp J_{\text{H}_x}^L \pm J_{\text{H}_x}^U)} \right]^2 + \left[\frac{A^U \alpha^U + A^L \alpha^L}{J_{\text{SH}}} \right]^2 \right\}^{-\frac{1}{2}} \text{sgn}(j) \tag{2.45}$$

2. Theoretical foundations

where $J_{\text{DMI}} = J_{\text{DMI}}^{\text{L}} + J_{\text{DMI}}^{\text{U}}$ and $J_{\text{SH}} = J_{\text{SH}}^{\text{L}} + J_{\text{SH}}^{\text{U}}$. Hence, on the one hand, no H_x field could influence v at T_{M} because $J_{\text{H}_x}^{\text{L}} - J_{\text{H}_x}^{\text{U}} = (m^{\text{L}} - m^{\text{U}}) H_x$ would evaluate to zero. Therefore, it could be assumed that the DMI field $H_{\text{DMI}} = \mp D / [\Delta (m^{\text{L}} - m^{\text{U}})]$ diverges at T_{M} .³³ But on the other hand, the first term has also no influence at T_{A} , too. Thus, within these approximations no H_x dependence is expected at angular momentum as well as at magnetic moment compensation. That there are two temperatures at which there is no H_x dependence is contradictory to the experiments performed for the present thesis (shown in section 4.3.3). Here, only one temperature for a given current density is found at which the DW velocity is not influenced by H_x . This temperature is clearly above T_{M} .³⁴ Therefore, the velocity dependence on H_x needs to be discussed more carefully, taking the exchange coupling into account.

2.3.7.1. Upper and lower bound for H_x independence

In order to get an idea about the influence of H_x , an upper and lower bound for $\frac{A^{\text{U}}}{A^{\text{L}}} \Big|_{\xi=0}$ are defined at which no H_x dependence is expected. H_x creates a torque $\tau_{\text{H}_x}^i$ on the magnetization in each layer. If this torque would cancel out in the two layers, such that the DW in the two layers would be driven in opposite directions, the total DW velocity would not increase for positive H_x and decrease for negative H_x or vice versa.³⁵ Figure 2.12 illustrates the situation for different ratios of A^{U} to A^{L} . Due to the ECT, the DW is moved into current flow direction in all depicted cases.

In Figure 2.12a and b, A^{U} is more dominant than A^{L} which could be at $m^{\text{U}} = m^{\text{L}}$ (if $\gamma^{\text{L}} > \gamma^{\text{U}}$ like in the Co/Gd bi-layer). A positive H_x field (Figure 2.12a) creates a torque which drives the DWs in the upper as well as in the lower layer against current flow direction. A negative field (Figure 2.12b) creates a torque in both layers which drives the DW into current flow direction. Hence, the DW velocity is decreased and increased for positive and negative fields, respectively. Therefore, for example at T_{M} , a H_x dependence is expected (!).

As explained for the ECT in section 2.3.6, due to the SHE, the magnetic moments of both layers are tilted towards \mathbf{s} . This makes it possible that the torque created by H_x in the upper and lower layer is into the same direction ($\tau_{\text{H}_x}^{\text{L}} \sim \tau_{\text{H}_x}^{\text{U}}$). Therefore, the DW in the lower layer would move towards the opposite direction than the DW in the upper layer. In Figure 2.12e and f, this case is depicted. ϕ^{U} as well as ϕ^{L} are within $\pi < \phi^i < 2\pi$. For a positive field (Figure 2.12e), the DW velocity in the upper layer is decreased but the DW velocity in the lower layer is increased. Oppositely for a negative field (Figure 2.12f), the DW velocity in the upper layer is increased but the DW in the lower layer is decreased. As a consequence, the resulting DW velocity of the

³³ H_{DMI} is obtained by solving the denominator of the first term in equation (2.45), $J_{\text{DMI}} \mp J_{\text{H}_x}^{\text{L}} \pm J_{\text{H}_x}^{\text{U}}$, for H_x .

³⁴ Also micromagnetic simulations using the LLG simulator confirm that (contrary to the approximated analytical results in equation (2.45)) there is a H_x dependence at $m^{\text{L}} = m^{\text{U}}$. In contrast, at $A^{\text{L}} = A^{\text{U}}$, H_x only slightly affects the DW velocity. These results are shown in Figure C.1 in the appendix. Noteworthy, the DW velocity drops symmetrically to both, positive and negative H_x at angular momentum compensation such that a linear fit to the curve would result in a slope $\xi = 0$. If the ratio of $A^{\text{L}}/A^{\text{U}}$ deviates from angular momentum compensation, the DW velocity increases or decreases to positive H_x and vice versa for negative H_x .

³⁵ Indeed, a slight but symmetric decrease of v to positive and negative H_x is expected.

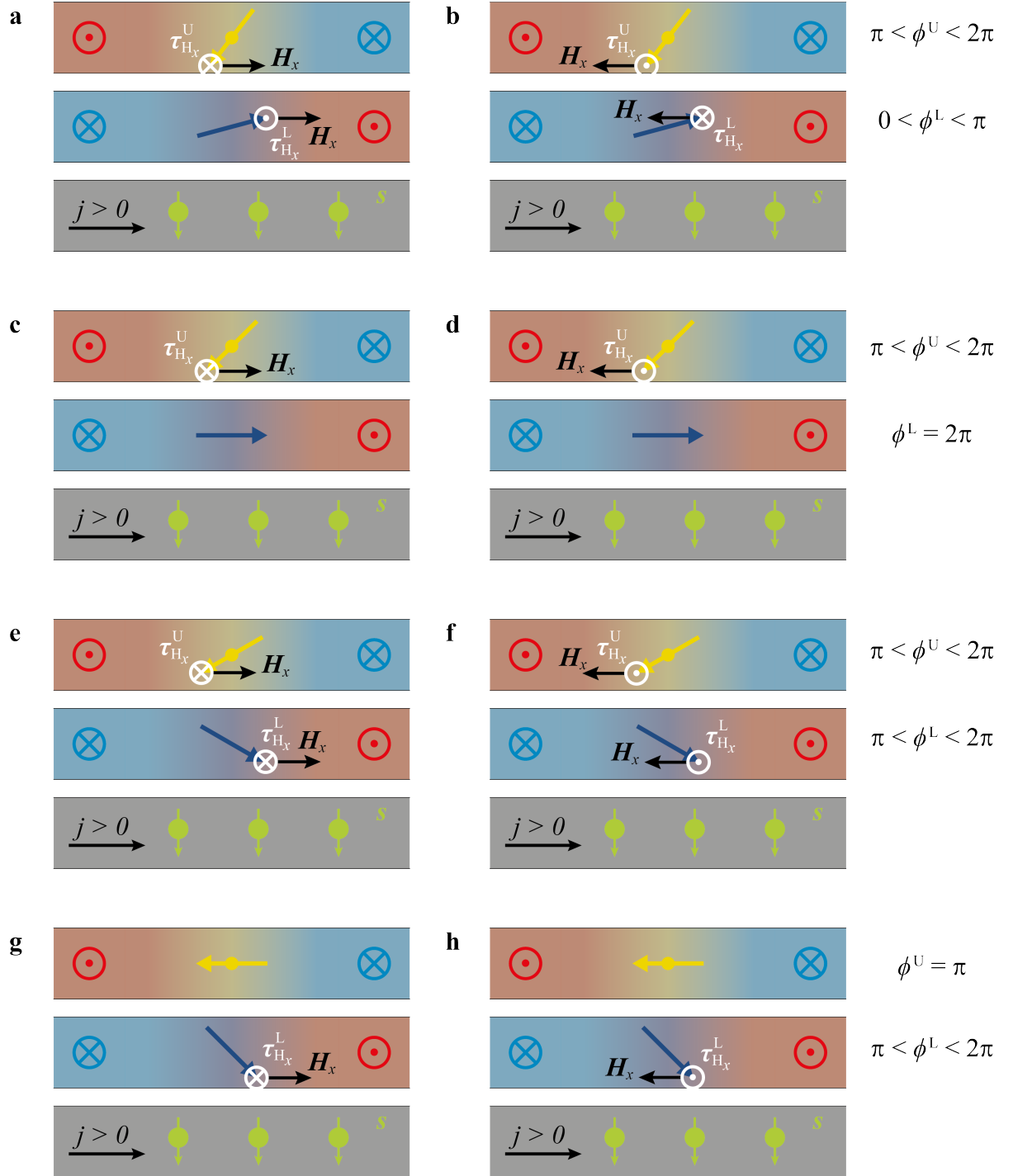


Figure 2.12.: Illustration of torque created by H_x in ferrimagnetic bi-layer.

From up to down, decreasing ratio A^U/A^L . Note that $J_{\text{ex}} < 0$ and J_{DMI}^U and $J_{\text{DMI}}^L > 0$. **a** and **b**, $A^U > A^L \left(1 + \frac{J_{\text{DMI}}^U}{|J_{\text{ex}}|}\right)$. **c** and **d**, $A^U = A^L \left(1 + \frac{J_{\text{DMI}}^U}{|J_{\text{ex}}|}\right)$. **e** and **f**, $A^L \left(1 + \frac{J_{\text{DMI}}^U}{|J_{\text{ex}}|}\right) > A^U > A^L \left(1 + \frac{J_{\text{DMI}}^L}{|J_{\text{ex}}|}\right)^{-1}$. **g** and **h**, $A^U = A^L \left(1 + \frac{J_{\text{DMI}}^L}{|J_{\text{ex}}|}\right)^{-1}$. **a**, **c**, **e**, and **g** for $H_x > 0$. **b**, **d**, **f**, and **h** for $H_x < 0$.

2. Theoretical foundations

combined system is neither decreased nor increased by neither a positive nor a negative H_x field.

For the appearance of this cancellation, the magnetic moments in the upper and lower layer need both to be within the range $\pi \leq \phi^i \leq 2\pi$ for a positive current density or $0 \leq \phi^i \leq \pi$ for a negative current density, or more easily: $\mathbf{m}^i \cdot \mathbf{s} > 0$ for both $i = \text{U}$ and L . Two bounds can be found, between those the ratio of A^{U} to A^{L} leads to the appearance of this situation: There is a lower bound at a certain ratio

$$\frac{A^{\text{U}}}{A^{\text{L}}} \Big|_{A^{\text{L}} \parallel H_x} = \begin{cases} \phi^{\text{L}} = \pi & \text{for a } \uparrow\downarrow \text{ DW or} \\ \phi^{\text{L}} = 0 & \text{for a } \downarrow\uparrow \text{ DW} \end{cases}$$

as shown in Figure 2.12c and d as well as an upper bound at a certain ratio

$$\frac{A^{\text{U}}}{A^{\text{L}}} \Big|_{A^{\text{U}} \parallel H_x} = \begin{cases} \phi^{\text{U}} = 0 & \text{for a } \uparrow\downarrow \text{ DW or} \\ \phi^{\text{U}} = \pi & \text{for a } \downarrow\uparrow \text{ DW} \end{cases}$$

as depicted in Figure 2.12g and h.

$\frac{A^{\text{U}}}{A^{\text{L}}} \Big|_{A^{\text{L}} \parallel H_x}$ can be calculated by solving equations (2.38b) and (2.38c) (in steady state, without STT and H_i) for $\phi^{\text{L}} = \pi$ and $\phi^{\text{L}} = 0$ for a $\uparrow\downarrow$ and $\downarrow\uparrow$ DW, respectively. Analogously, $\frac{A^{\text{U}}}{A^{\text{L}}} \Big|_{A^{\text{U}} \parallel H_x}$ can be found by solving equations (2.38b) and (2.38c) using $\phi^{\text{U}} = 0$ and $\phi^{\text{U}} = \pi$ for a $\uparrow\downarrow$ and $\downarrow\uparrow$ DW, respectively. This then yields (assuming $J_{\text{DMI}}^i > 0$ and $J_{\text{ex}} < 0$)

$$\text{Lower bound: } \frac{A^{\text{U}}}{A^{\text{L}}} \Big|_{A^{\text{L}} \parallel H_x} = 1 - \frac{J_{\text{DMI}}^{\text{U}}}{J_{\text{ex}}} \quad (2.46)$$

$$\text{Upper bound: } \frac{A^{\text{U}}}{A^{\text{L}}} \Big|_{A^{\text{U}} \parallel H_x} = \left(1 - \frac{J_{\text{DMI}}^{\text{L}}}{J_{\text{ex}}} \right)^{-1}. \quad (2.47)$$

Hence, the ratio which is searched for must be in the range $A^{\text{L}} \left(1 + \frac{J_{\text{DMI}}^{\text{U}}}{|J_{\text{ex}}|} \right) > A^{\text{U}} > A^{\text{L}} \left(1 + \frac{J_{\text{DMI}}^{\text{L}}}{|J_{\text{ex}}|} \right)^{-1}$. In order to find the exact value, the SHE needs to be taken into account. This, however, complicates the situation due to the ECT which links the motion of the upper and lower DW by ϕ^{U} and ϕ^{L} .

2.3.7.2. Optimal ratio $A^{\text{U}}/A^{\text{L}}$ for H_x independence

Mathematically, a linear fit to a v vs H_x curve will lead to $\xi = 0$ if $\frac{dv}{dH_x} \approx 0$ within the range of the fit which is symmetric around $H_x = 0$ for small H_x . Thus, the optimal ratio $\frac{A^{\text{U}}}{A^{\text{L}}} \Big|_{\xi=0}$ can be found by solving $\frac{dv}{dH_x} \Big|_{H_x \approx 0} = 0$. In steady state motion ϕ^{L} and ϕ^{U} are determined by J_{SH}^i , J_{ex} , J_{DMI}^i , and $J_{H_x}^i$. Hence, ϕ^{L} and ϕ^{U} are a function of H_x : $\phi^{\text{L}}(H_x)$ and $\phi^{\text{U}}(H_x)$. Equation (2.38a) shows that the changes of ϕ^{L} and ϕ^{U} directly influence the DW velocity v ($\phi^{\text{L}}, \phi^{\text{U}}$). Thus, it can be written that $\frac{dv(H_x)}{dH_x} = \frac{\partial v}{\partial \phi^{\text{L}}} \frac{\partial \phi^{\text{L}}}{\partial H_x} + \frac{\partial v}{\partial \phi^{\text{U}}} \frac{\partial \phi^{\text{U}}}{\partial H_x}$. The angle between ϕ^{U} and ϕ^{L} can be expressed by

$$\delta\phi \stackrel{\text{def}}{=} \phi^{\text{L}} - \phi^{\text{U}} - \pi. \quad (2.48)$$

Consequently, the following two cases need to equal

$$\frac{dv(H_x)}{dH_x} = \begin{cases} \frac{\partial v}{\partial \phi^L} \frac{\partial \phi^L}{\partial H_x} + \frac{\partial v}{\partial \phi^L} \frac{\partial \phi^L}{\partial \phi^U} \frac{\partial \phi^U}{\partial H_x} = \frac{\partial v}{\partial \phi^L} \left(\frac{\partial \phi^L}{\partial H_x} + \frac{\partial \phi^L}{\partial \phi^U} \frac{\partial \phi^U}{\partial H_x} \right) \\ \frac{\partial v}{\partial \phi^U} \frac{\partial \phi^U}{\partial H_x} + \frac{\partial v}{\partial \phi^U} \frac{\partial \phi^U}{\partial \phi^L} \frac{\partial \phi^L}{\partial H_x} = \frac{\partial v}{\partial \phi^U} \left(\frac{\partial \phi^U}{\partial H_x} + \frac{\partial \phi^U}{\partial \phi^L} \frac{\partial \phi^L}{\partial H_x} \right). \end{cases}$$

Thus, finding

$$\frac{\partial v}{\partial \phi^U} = 0$$

will lead to $\frac{dv(H_x)}{dH_x} = 0$. The here used notation ϕ^U means that the upper symbol (which is U here) stands for the $\uparrow\downarrow$ and the lower symbol (which is L here) stands for the $\downarrow\uparrow$ DW. This is consistent with \pm and \mp signs for $\uparrow\downarrow$ and $\downarrow\uparrow$ DWs.

ϕ^U or ϕ^L in equation (2.38a) can be substituted by using equation (2.48). Then, $\cos \phi^U$ can be approximated by $\cos \phi^U|_{\phi^U=0} \approx 1 - \frac{\phi^{U2}}{2}$ because $\phi^L \approx \pi$ and $\phi^U \approx 0$ in case of a $\uparrow\downarrow$ DW as well as $\phi^L \approx 0$ and $\phi^U \approx \pi$ in case of a $\downarrow\uparrow$ DW. Hence,

$$v \approx \begin{cases} \left[\frac{\Delta}{\alpha^L A^L + \alpha^U A^U} \left[J_{\text{SH}}^L \left(1 - \frac{(\phi^U + \delta\phi)^2}{2} \right) + J_{\text{SH}}^U \left(1 - \frac{\phi^{U2}}{2} \right) \right] \right] & \text{for a } \uparrow\downarrow \text{ DW and} \\ \left[\frac{\Delta}{\alpha^L A^L + \alpha^U A^U} \left[J_{\text{SH}}^L \left(1 - \frac{\phi^{L2}}{2} \right) + J_{\text{SH}}^U \left(1 - \frac{(\phi^L - \delta\phi)^2}{2} \right) \right] \right] & \text{for } \downarrow\uparrow \text{ DW.} \end{cases}$$

By solving $\frac{dv}{d\phi^U} = 0$, the optimal orientations ϕ^{L*} and ϕ^{U*} can be calculated which are

$$\frac{dv}{d\phi^U} = 0 \Rightarrow \begin{cases} \phi^{L*} = \frac{J_{\text{SH}}^U}{J_{\text{SH}}^L + J_{\text{SH}}^U} \delta\phi + \pi, & \phi^{U*} = \frac{-J_{\text{SH}}^L}{J_{\text{SH}}^L + J_{\text{SH}}^U} \delta\phi & \text{for } \uparrow\downarrow \text{ DW and} \\ \phi^{L*} = \frac{J_{\text{SH}}^U}{J_{\text{SH}}^L + J_{\text{SH}}^U} \delta\phi, & \phi^{U*} = \frac{-J_{\text{SH}}^L}{J_{\text{SH}}^L + J_{\text{SH}}^U} \delta\phi - \pi & \text{for } \downarrow\uparrow \text{ DW.} \end{cases}$$

To determine $\frac{A^U}{A^L} \Big|_{\xi=0}$, ϕ^{L*} and ϕ^{U*} are inserted into equations (2.38b) and (2.38c), respectively, which yields

$$v \Big|_{\xi=0} = \frac{\Delta}{A^L} \left(\pm J_{\text{DMI}}^L \frac{J_{\text{SH}}^U}{J_{\text{SH}}^L + J_{\text{SH}}^U} \delta\phi \mp J_{\text{ex}} \delta\phi \right) \quad (2.49b)$$

$$v \Big|_{\xi=0} = \frac{\Delta}{A^U} \left(\pm J_{\text{DMI}}^U \frac{J_{\text{SH}}^L}{J_{\text{SH}}^L + J_{\text{SH}}^U} \delta\phi \mp J_{\text{ex}} \delta\phi \right) \quad (2.49c)$$

Since both equations of motion (2.49b) and (2.49c), need to be fulfilled, these two can be equated. This finally leads to the desired ratio

$$\frac{A^U}{A^L} \Big|_{\xi=0} = \frac{J_{\text{DMI}}^U J_{\text{SH}}^L - (J_{\text{SH}}^L + J_{\text{SH}}^U) J_{\text{ex}}}{J_{\text{DMI}}^L J_{\text{SH}}^U - (J_{\text{SH}}^L + J_{\text{SH}}^U) J_{\text{ex}}} = \frac{J_{\text{DMI}}^U - (1 + \eta) J_{\text{ex}}}{\eta J_{\text{DMI}}^L - (1 + \eta) J_{\text{ex}}} \quad (2.50)$$

with $\eta \stackrel{\text{def}}{=} \frac{J_{\text{SH}}^U}{J_{\text{SH}}^L} = \frac{\theta_{\text{SH}}^U}{\theta_{\text{SH}}^L}$. Hence, beside the dependence on J_{DMI}^i and J_{ex} as discussed in equation (2.46) and equation (2.47), also η influences $\frac{A^U}{A^L} \Big|_{\xi=0}$. This can be attributed to the strong interplay between ECT and the torques generated by the DMI and H_x field. In the limit $\eta \rightarrow 0$ (if $\theta_{\text{SH}}^U \ll \theta_{\text{SH}}^L$), equation (2.50) converges to the lower bound (2.46) and for $\eta \rightarrow \infty$ (if $\theta_{\text{SH}}^L \ll \theta_{\text{SH}}^U$),

2. Theoretical foundations

equation (2.50) converges to the upper bound (2.47).³⁶

Note that the j dependence in equation (2.50) cancels out. There is only a dependence on the ratio of spin HALL angles of the lower and upper layer. One crucial factor of the experiments is the JOULE heating produced by the current pulses applied to move the DWs. The circumstance that $\frac{A^U}{A^L} \Big|_{\xi=0}$ is independent on j can be used to determine this heat. Hence, the DW velocity dependence on an external field H_x at a given current density is measured. In section 3.2.4 this method is explained in more detail.

2.3.8. Dry friction

In the experiments of this thesis it is found that a threshold current is needed to initiate DW motion which can be attributed to pinning of the DW at extrinsic defects. To account for this pinning a dry friction model is used as discussed in [93]. This kind of friction is analogous to the dynamic friction in classical mechanics. The dry friction can be associated with the torque term [112, 113]

$$\boldsymbol{\tau}_{\text{df}}^i = \gamma H_{\text{df}}^i \left(\hat{\mathbf{m}}^i \times \frac{\dot{\mathbf{m}}^i}{|\dot{\mathbf{m}}^i|} \right)$$

with H_{df}^i an effective pinning field which is described by $H_{\text{df}}^i = K_{\text{df}}^i m^i$ where K_{df}^i is a constant which accounts for the intensity of the dry friction. As it will be discussed in section 5.3, K_{df}^i might scale proportionally with K_{cryst}^i as it reflects the inhomogeneities of the anisotropy. Compared to GILBERT damping, which acts like a viscous drag, the dry friction does not depend on the magnitude of $\dot{\mathbf{m}}^i$ but only on its direction.

Including the dry friction torque into the LLG equation like for STT and SHE yields

$$\begin{aligned} \frac{d\hat{\mathbf{m}}^i}{dt} &= -\gamma^i \hat{\mathbf{m}}^i \times \mathbf{H}_{\text{eff}}^i + \frac{\alpha^i}{m^i} \hat{\mathbf{m}}^i \times \dot{\mathbf{m}}^i + \boldsymbol{\tau}_{\text{aSTT}}^i + \boldsymbol{\tau}_{\text{naSTT}}^i + \boldsymbol{\tau}_{\text{SH}}^i + \boldsymbol{\tau}_{\text{df}}^i \\ &= -\gamma^i \hat{\mathbf{m}}^i \times \left(\mathbf{H}_{\text{eff}}^i + \mathbf{H}_{\text{D}}^i + \mathbf{H}_{\text{STT}}^i + \mathbf{H}_{\text{SH}}^i - \underbrace{H_{\text{df}}^i \frac{d\hat{\mathbf{m}}^i}{dt}}_{\mathbf{H}_{\text{df}}^i} \right). \end{aligned}$$

Following analogously the procedure as for the GILBERT damping to derive the equations of motion, the dissipation energy due to dry friction P_{df} is given by

$$\begin{aligned} P_{\text{df}} &= \int \mathbf{H}_{\text{df}}^L d\dot{\mathbf{m}}^L + \int \mathbf{H}_{\text{df}}^U d\dot{\mathbf{m}}^U \\ &= -H_{\text{df}}^L \frac{d\hat{\mathbf{m}}^L}{dt} \cdot \dot{\mathbf{m}}^L - H_{\text{df}}^U \frac{d\hat{\mathbf{m}}^U}{dt} \cdot \dot{\mathbf{m}}^U \\ &= -m^L H_{\text{df}}^L \sin \theta \sqrt{(\dot{\phi}^L)^2 + \left(\frac{\dot{q}}{\Delta}\right)^2} - m^U H_{\text{df}}^U \sin \theta \sqrt{(\dot{\phi}^U)^2 + \left(\frac{\dot{q}}{\Delta}\right)^2}. \end{aligned}$$

³⁶ As discussed in section 5.1.1, $J_{\text{DMI}}^{\text{Gd}} \approx 0$ and $\theta_{\text{SH}}^{\text{Gd}} \approx 0$. Hence, $\frac{A^{\text{Gd}}}{A^{\text{Co}}} \Big|_{\xi=0} \approx 1$, meaning $\xi = 0$ at $m^{\text{Gd}}/m^{\text{Co}} \approx \gamma^{\text{Gd}}/\gamma^{\text{Co}}$.

Including P_{df} in F yields

$$\begin{aligned}
 F = & -\alpha^{\text{L}} A^{\text{L}} \Delta \left[\left(\dot{\phi}^{\text{L}} \right)^2 + \frac{\dot{q}^2}{\Delta^2} \right] - \alpha^{\text{U}} A^{\text{U}} \Delta \left[\left(\dot{\phi}^{\text{U}} \right)^2 + \frac{\dot{q}^2}{\Delta^2} \right] \\
 & \mp \pi m^{\text{L}} H_{\text{SH}}^{\text{L}} \cos \phi^{\text{L}} \dot{q} \pm \pi m^{\text{U}} H_{\text{SH}}^{\text{U}} \cos \phi^{\text{U}} \dot{q} \\
 & - \pi m^{\text{L}} H_{\text{df}}^{\text{L}} \Delta \sqrt{\left(\dot{\phi}^{\text{L}} \right)^2 + \left(\frac{\dot{q}}{\Delta} \right)^2} - \pi m^{\text{U}} H_{\text{df}}^{\text{U}} \Delta \sqrt{\left(\dot{\phi}^{\text{U}} \right)^2 + \left(\frac{\dot{q}}{\Delta} \right)^2}.
 \end{aligned}$$

Inserting F in to the RAYLEIGH-LAGRANGE equation (2.22) then results in the following equations of motion:

$X_l = q$:

$$\begin{aligned}
 \dot{q} = & \frac{\Delta}{\alpha^{\text{L}} A^{\text{L}} + \alpha^{\text{U}} A^{\text{U}}} \left[\mp \left(A^{\text{L}} \dot{\phi}^{\text{L}} - A^{\text{U}} \dot{\phi}^{\text{U}} \right) \pm \left(J_{\text{H}_z}^{\text{L}} - J_{\text{H}_z}^{\text{U}} \right) \right. \\
 & - J_{\text{df}}^{\text{L}} \frac{\frac{\dot{q}}{\Delta}}{\sqrt{\left(\dot{\phi}^{\text{L}} \right)^2 + \left(\frac{\dot{q}}{\Delta} \right)^2}} - J_{\text{df}}^{\text{U}} \frac{\frac{\dot{q}}{\Delta}}{\sqrt{\left(\dot{\phi}^{\text{U}} \right)^2 + \left(\frac{\dot{q}}{\Delta} \right)^2}} \\
 & \left. \mp \left(J_{\text{SH}}^{\text{L}} \cos \phi^{\text{L}} - J_{\text{SH}}^{\text{U}} \cos \phi^{\text{U}} \right) \right]
 \end{aligned} \tag{2.51a}$$

$X_l = \phi^{\text{L}}$:

$$\begin{aligned}
 \dot{q} = & \frac{\Delta}{A^{\text{L}}} \left[\pm \alpha^{\text{L}} A^{\text{L}} \dot{\phi}^{\text{L}} - J_{\text{DMI}}^{\text{L}} \sin \phi^{\text{L}} \pm J_{\text{ex}} \sin \left(\phi^{\text{L}} - \phi^{\text{U}} \right) \right. \\
 & \left. \pm J_{\text{df}}^{\text{L}} \frac{\dot{\phi}^{\text{L}}}{\sqrt{\left(\dot{\phi}^{\text{L}} \right)^2 + \left(\frac{\dot{q}}{\Delta} \right)^2}} \pm \left(J_{\text{H}_x}^{\text{L}} \sin \phi^{\text{L}} - J_{\text{H}_y}^{\text{L}} \cos \phi^{\text{L}} \right) \right]
 \end{aligned} \tag{2.51b}$$

$X_l = \phi^{\text{U}}$:

$$\begin{aligned}
 \dot{q} = & \frac{\Delta}{A^{\text{U}}} \left[\mp \alpha^{\text{U}} A^{\text{U}} \dot{\phi}^{\text{U}} - J_{\text{DMI}}^{\text{U}} \sin \phi^{\text{U}} \pm J_{\text{ex}} \sin \left(\phi^{\text{L}} - \phi^{\text{U}} \right) \right. \\
 & \left. \mp J_{\text{df}}^{\text{U}} \frac{\dot{\phi}^{\text{U}}}{\sqrt{\left(\dot{\phi}^{\text{U}} \right)^2 + \left(\frac{\dot{q}}{\Delta} \right)^2}} \mp \left(J_{\text{H}_x}^{\text{U}} \sin \phi^{\text{U}} - J_{\text{H}_y}^{\text{U}} \cos \phi^{\text{U}} \right) \right].
 \end{aligned} \tag{2.51c}$$

with

$$J_{\text{df}}^i \stackrel{\text{def}}{=} \frac{\pi}{2} K_{\text{df}}^i m^{i2}.$$

In case of steady state motion where $\dot{\phi}^{\text{L}} = \dot{\phi}^{\text{U}} = 0$, equations (2.51b) and (2.51c) are not affected by the dry friction whereas equation (2.51a) can be rewritten as

$$\begin{aligned}
 v = & \frac{\Delta}{\alpha^{\text{L}} A^{\text{L}} + \alpha^{\text{U}} A^{\text{U}}} \left[\pm \left(m^{\text{L}} - m^{\text{U}} \right) H_z \mp \frac{\pi \hbar}{2 e} \left(\theta_{\text{SH}}^{\text{L}} \cos \phi^{\text{L}} - \theta_{\text{SH}}^{\text{U}} \cos \phi^{\text{U}} \right) j \right. \\
 & \left. - \frac{\pi}{2} \left(K_{\text{df}}^{\text{L}} m^{\text{L}2} + K_{\text{df}}^{\text{U}} m^{\text{U}2} \right) \text{sgn}(v) \right]
 \end{aligned} \tag{2.52a}$$

where $\text{sgn}(v) = \frac{v}{|v|}$

2. Theoretical foundations

2.3.8.1. Threshold field

MALOZEMOFF and SLONCZEWSKI equated the pinning field H_{df} with the coercive field H_c [93]. Although this is correct for single magnetic layers, there is a difference for antiferromagnetically coupled systems if H_c is meant to be the minimum field to move a DW in any direction.³⁷ Instead of the coercive field, a threshold field H_{th} could be defined which is the minimum out-of-plane field to drive the DW in positive x direction by just overcoming dry friction. Solving equation (2.52a) yields

$$H_{\text{th}} = \pm \frac{1}{m^{\text{L}} - m^{\text{U}}} \left(\frac{\pi}{2} K_{\text{df}}^{\text{L}} m^{\text{L}2} + \frac{\pi}{2} K_{\text{df}}^{\text{U}} m^{\text{U}2} \right). \quad (2.53)$$

Note that H_{th} is negative for a $\downarrow\uparrow$ DW for $m^{\text{L}} > m^{\text{U}}$ because moving a $\downarrow\uparrow$ DW into positive x direction requires a negative field. For $m^{\text{L}} < m^{\text{U}}$ the threshold field switches sign.

As it has been discussed in section 2.3.4, if $m^{\text{L}} = m^{\text{U}}$, the DW cannot be moved by an out-of-plane field H_z . Hence, H_{th} diverges at magnetic moment compensation but the total dry friction energy is still finite:

$$J_{\text{df}} \stackrel{\text{def}}{=} \frac{\pi}{2} K_{\text{df}}^{\text{L}} m^{\text{L}2} + \frac{\pi}{2} K_{\text{df}}^{\text{U}} m^{\text{U}2}.$$

Extending MALOZEMOFF's and SLONCZEWSKI's approach to ferrimagnetic bi-layers, H_c could be defined by

$$H_c = |H_{\text{th}}| = \frac{J_{\text{df}}}{|m^{\text{L}} - m^{\text{U}}|}. \quad (2.54)$$

2.3.8.2. Threshold current

The dry friction has the same effect on CIDWM like for FDDWM. In order to move the DW, the dry friction needs to be overcome. The spin Hall current needs to be as large so that $J_{\text{SH}} > J_{\text{df}}$. Thus, the threshold current j_{th} can be calculated by

$$j_{\text{th}} = \frac{2e}{\hbar} \frac{1}{\theta_{\text{SH}}^{\text{L}} + \theta_{\text{SH}}^{\text{U}}} \left[K_{\text{df}}^{\text{L}} (m^{\text{L}})^2 + K_{\text{df}}^{\text{U}} (m^{\text{U}})^2 \right] \text{sgn}(j). \quad (2.55)$$

In contrast to H_c , j_{th} does not scale inverse proportionally to $|m^{\text{L}} - m^{\text{U}}|$ but solely with $(m^i)^2$.

From a technological perspective, reducing the threshold current is of major interest. From equation (2.55) it becomes obvious that j_{th} can be reduced if either $\theta_{\text{SH}}^{\text{L}} + \theta_{\text{SH}}^{\text{U}}$ was increased or $K_{\text{df}}^{\text{L}} (m^{\text{L}})^2$ and $K_{\text{df}}^{\text{U}} (m^{\text{U}})^2$ are reduced. The effective spin HALL angles $\theta_{\text{SH}}^{\text{L}}$ and $\theta_{\text{SH}}^{\text{U}}$ can be increased by either finding underlayers which exhibit a larger spin HALL effect, or by using magnetic materials which interact more efficiently with the spin current,³⁸ or by increasing the transparency of the underlayer/magnetic layer interface for the spin current [114]. To reduce the dry friction constants K_{df}^{L} and K_{df}^{U} , the origin of those needs to be identified for the particular sample. Since

³⁷ Since the coercive field is often measured by switching a magnetic film, H_c originates from a combination of nucleation and DW propagation. While propagation of DWs is typically the major factor for macroscopic samples, the nucleation can be absent for defect-free nanomagnets. In this case, H_c is determined by the anisotropy and ZEEMAN energy.

³⁸ As discussed in section 2.3.5.2, the $4f$ electrons which carry the magnetization in Gd do not interact much with the $3d$ conduction electrons which carry the spin current [108, 109].

these are a measure of disorder and imperfections in the sample, one straightforward approach is to grow perfectly crystalline samples with as low defect density as possible.

Additional to increasing θ_{SH}^i and reducing K_{df}^i , reducing the magnetic moment of each layer m^i has a large impact due to the quadratic scaling in equation (2.55). This is an interesting aspect as m^i is temperature dependent and decreases with increasing T . Hence, another approach to reduce j_{th} could be to use materials which are close to T_C around room temperature. However, this approach might lead to thermal stability problems. In order to take these into account including a thermal energy term might be needed in the analytical model as proposed in [115] for example.³⁹ Alternatively to reduce m^i , the magnetic material could be diluted such that M_S^i is decreased or simply the layer thickness t^i can be reduced. But be aware that if doing either of these, changes of the magnetic properties (M_S^i and K_{eff}^i) have to be taking account which could again influence the DW mobility (equation (2.41)).

2.3.8.3. Motion efficiency

In order to quantify the dissipation by j_{th} , the efficiency

$$\epsilon(j) \stackrel{\text{def}}{=} \frac{J_{\text{motion}}(j)}{J_{\text{SH}}(j)} \quad (2.56)$$

can be defined where $J_{\text{motion}} = \frac{\alpha^L A^L + \alpha^U A^U}{\Delta} v(j)$ with $v(j)$ denoting the DW velocity at a certain current density j . It gives the ratio of the effective motion energy J_{motion} to the input energy by the SHE. ϵ is a dimensionless measure which can be suitable when it comes to technological applications, although the electrical energy dissipation converted into JOULE heating due to wire resistance needs to be taken into account as well.

Using equation (2.52a) the efficiency can also be written as

$$\epsilon(j) = \frac{|J_{\text{SH}}^L \cos \phi^L - J_{\text{SH}}^U \cos \phi^U| - J_{\text{df}}}{|J_{\text{SH}}|} \quad (2.57)$$

which reflects the influence of the torque mechanism in the cosine terms as well as the influence of the threshold current density in J_{df} . Without $J_{\text{df}} = J_{\text{df}}^L + J_{\text{df}}^U$, the efficiency only depends on the torque efficiency. Due to J_{df} , the efficiency is reduced. At $A^L = A^U$, ϵ increases for increasing j as $|J_{\text{SH}}^L \cos \phi^L - J_{\text{SH}}^U \cos \phi^U| \approx J_{\text{SH}}$ and therefore $\epsilon(j) = 1 - \frac{J_{\text{df}}}{|J_{\text{SH}}|}$. $J_{\text{df}} = 0$ would lead to $\epsilon(j) = 1$ for all current densities at the angular momentum compensation point.

The efficiency $\epsilon(j)$ is linked to the mobility $\varpi(j)$ (given in equation (2.41)) by

$$\epsilon(j) = \frac{\alpha^L A^L + \alpha^U A^U}{\Delta J_{\text{SH}}(j)} \int_0^j \varpi(j') \, dj'.$$

³⁹ Thermal energy is implicitly considered in $M_S^i(T)$ but there is potentially a more direct influence of temperature on the DW. From the experiments performed for this thesis it became clear that the thermal energy can be in the range of J_{df} : For the Co/Gd sample, the DW was not stable as soon as sample's temperature was above 250 K. This led to random displacement of the DW which cannot be reflected by the dry friction model.

2. Theoretical foundations

At low j ($\sim j_{\text{th}}$) the threshold current dominates $\epsilon(j)$ whereas at high j ($\gg j_{\text{th}}$) the torque mechanisms dominate $\epsilon(j)$.

3. Experimental setup and methods

In the racetrack memory concept proposed by STUART PARKIN, the nanowires, in which the information is stored, are thin strips of nanometer thick layers of magnetic materials (cf. Figure 1.1) [1, 2, 116]. For study purposes, exemplary short nanowires were fabricated by etching a certain pattern into the magnetic layers which had been sputtered before on a wafer. The samples were mounted inside a cryostat so that they could be cooled and heated. A window in the cryostat allowed to observe the sample from the top. The sample could be connected to a pulse generator to move DWs by current pulses. The DW motion was then monitored by using a polar KERR microscope which was able to image magnetic domains if the magnetization was perpendicular to the film plane. Additional measurement methods were used to characterize the magnetic properties of the sample.

The main focus of the experiments was on temperature-dependent CIDWM measurements, especially in nanowires consisting of a ferrimagnetic bi-layer. The methods used in the thesis at hand were similar to that of my master thesis [29], although the objective of the experiments was distinct. Section 3.1 focuses on the sample preparation. In section 3.2, the temperature-dependent measurements of CIDWM in the temperature-controllable KERR microscope are explained. Additional measurement techniques to characterize the samples are discussed in section 3.3.

The samples were prepared by Dr. SEE-HUN YANG and CHIRAG GARG at the IBM ALMADEN RESEARCH CENTER in SAN JOSE, CALIFORNIA, USA. All experiments were performed at the MAX-PLANCK-INSTITUTE OF MICROSTRUCTURE PHYSICS in HALLE, GERMANY, except of the XMCD measurements.

3.1. Sample preparation

In order to have a test structure for DW motion in the nanowires, which later on shall be used in the racetrack memory, the layers of interest were sputtered on silicon (Si) wafers, 1-inch in diameter, and afterwards the nanowires were etched into a small area of these layers. Both steps, first sputtering and second lithography, are explained in this section.

3.1.1. Sputtering

The thin films' substrate was Si(100). It was oxidized at the surface to amorphous silicon dioxide (SiO_2). This SiO_2 layer was 25 nm thick and very resistive. On top of the SiO_2 , typically another insulating layer of 10 nm aluminum oxide (Al_2O_3) was sputtered which further function was to form a smooth surface. The next layer was a 2 nm thick tantalum nitride (TaN) layer which was used as an adhesion layer between the Al_2O_3 and the following layers of interest. These

3. Experimental setup and methods

layers included a 20 - 30 Å thick platinum (Pt) underlayer followed by the magnetic layers of interest (unit: Å). These were in the case of the ferromagnetic layer structure a multilayer of cobalt (Co) and nickel (Ni): 3 Co / 7 Ni / 1.5 Co (sample ID: S4324-15). For the SAF structure, two ferromagnetic layers were separated by a ruthenium (Ru) spacer layer which had the right thickness of 8 Å to couple the ferromagnetic layers antiferromagnetically [64]: 3 Co / 7 Ni / 1.5 Co / 8 Ru / 3 Co / 7 Ni / 3 Co (sample ID: S4944-04). For the ferrimagnetic bi-layer, Co and gadolinium (Gd) was used: 5 Co / 18 Gd (sample ID: S4804-09). The ratio of the thicknesses t^{Co} and t^{Gd} was chosen such that the magnetic moment compensation temperature is expected to be within the range between 100 - 300 K [68] to enable the investigation of DW motion around this point. To protect the magnetic layers against oxidation, a 5 nm TaN capping layer was grown on top. After each sputtering process, the growth rate was checked by measuring the height of each material which was additionally sputtered on a calibration film.

3.1.2. Lithography

After sputtering, the samples were patterned using photolithography to develop the nanowires. Therefore the films were covered uniformly by a photoresist using spin coating and were afterwards baked to drive off excess photoresist solvent. Hereafter, the film was exposed to ultraviolet light using a mask which had the pattern of the later devices on it. After another backing process the resist which had been exposed to the ultraviolet light was removed by a developer. Finally, the sputtered layers, which were no longer covered by the resist, were etched away by an ion beam and after that the remaining resist was removed.

An image of the sample after the lithography and an image of the final device is shown in Figure 3.1. As can be seen in the lower image, there was still an area of non-patterned film which could be cut off and used for experiments to obtain magnetic properties of the film. This is explained in more detail in section 3.3. Furthermore, it can be seen in the image of the device that the nanowires were located in the middle between two large pads which were used to connect the nanowire to a pulse generator via wire bonding. The nanowires used for this thesis had a length of 50 μm and a width of 2 μm . The coordinate system is analogous to the coordinates introduced in Figure 2.2. x is pointing along the wire, z is oriented perpendicular to the film plane, and y is in the plane of the film and perpendicular to the wire.

3.2. Measurement of domain wall motion

The measurement of CIDWM in the nanowires is possible in several ways. To see the magnetization of out-of-plane materials, a convenient method is the KERR microscopy.⁴⁰ It yields the advantage that the propagation of a domain is visible in a microscope. Utilizing differential KERR microscopy and image analysis, displacements of a DW can be measured with relative good

⁴⁰ In early studies, for example HALL bars were used as an alternative method frequently. e.g. [116].

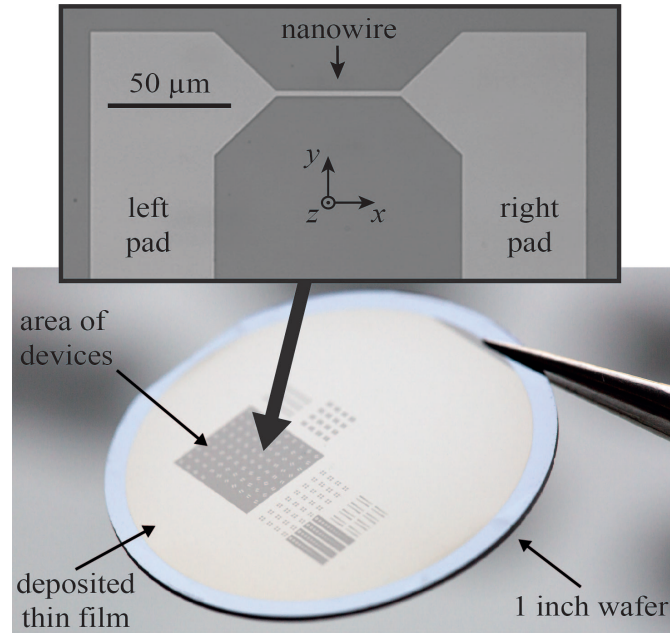


Figure 3.1.: Sample after sputtering and lithography. Lower image: 1 inch wafer with deposited thin film (yellowish colored area). About 84 devices with different wire width etched out by lithography (within dark square). Additional devices for other measurements next to device area (were not used for this thesis). Area which is not patterned was used for additional measurement methods (cf. section 3.3). Upper microscope image: One example device with two connection pads for wire bonding and 2 μm wide nanowire in between.

accuracy and, also very important, unexpected behavior, like the creation of several domains, can be monitored.

3.2.1. Differential Kerr microscopy

The working principle of the KERR microscope is based on the polar magneto-optical KERR effect which can be described as follows (cf. [117]). Linearly polarized light, which is a combination of left and right circularly polarized light, is focused on the sample. The complex FRESNEL reflection coefficients for left and right circularly polarized light are different depending on the direction of the magnetization pointing in- or out-of-plane. This leads to a rotation of the polarization plane of the incident linearly polarized light (KERR rotation) and a change of the ellipticity of the light (KERR ellipticity). Both effects depend on the direction of the local magnetization and the magnitude is determined by the off-diagonal terms in the permittivity tensor which are odd linear functions of the magnetization [118]. By using an analyzer for the reflected light, due to the KERR rotation oppositely magnetized domains become visible in the microscope by seeing a darker or lighter contrast. In case of the ferrimagnetic Co/Gd bi-layer, the KERR rotation is dominated by the Co layer [68]. The analyzer was adjust in a way that a dark or light contrast

3. Experimental setup and methods

corresponds to a \downarrow or \uparrow domain in the Co layer, respectively. This was verified by applying a positive H_z field and looking at the expansion or shrinking of the domains. Above T_M , in the Co dominant regime, the bright (\uparrow) domain expanded. Below T_M , in the Gd dominant regime, the dark (\downarrow) domain expanded. An example of the resulting image is shown in Figure 3.2 where a \downarrow domain was located between two \uparrow domains.

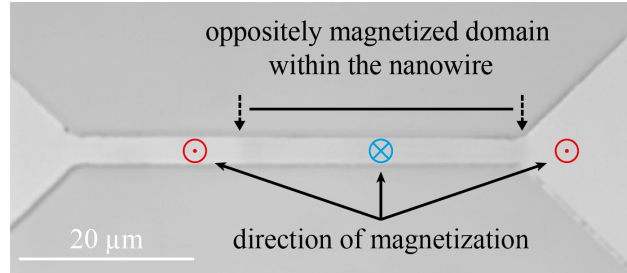


Figure 3.2.: Exemplary Kerr microscope image of magnetic domain inside nanowire. Image taken by camera looking through KERR microscope. \downarrow domain (indicated by \otimes) surrounded by two \uparrow domains (indicated by \odot). In ferrimagnetic Co/Gd bi-layer, KERR rotation is dominated by the Co layer [68].

In order to better visualize displacements of domains, a LABVIEW software called KERRLAB was used. It saved an image (or the mean of a series of images), like the one shown in Figure 3.2, before the motion of a DW and subtracted an image (or the mean of a series of images) after the motion. Due to the subtraction, only changes of the magnetization became visible. The resulting differential image showed a dark/bright contrast in the region where a domain which magnetization points \downarrow or \uparrow was moved into an area where a \uparrow - or \downarrow -pointing domain had been before, respectively. Exemplary differential images are shown in Figure 3.3. The investigation of DW motion by combining the usage of the KERR microscope and this image processing is called differential KERR microscopy.

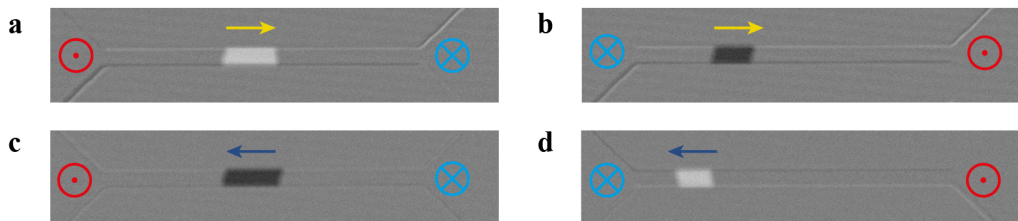


Figure 3.3.: Exemplary differential Kerr microscopy images. In **a** and **b** DW was moved to the right, indicated by the yellow arrow. In **c** and **d** DW was moved to the left, indicated by blue arrow. Region which changed from \uparrow domain to \downarrow domain became white (**a** and **d**). Region which changed from \downarrow domain to \uparrow domain became dark (**b** and **c**).

3.2.2. Experimental setup

An image of the experimental setup is shown in Figure 3.4. The KERR microscope was equipped with a camera to take images of the device as discussed in the last section. The sample was mounted inside a cryostat which had a window on top. Through this window, the polarized light fell onto the sample, was reflected and was captured by the camera. The cryostat was connected via gas lines to either liquid nitrogen or liquid helium. The liquid was pumped through the cryostat, evaporated in a cold finger underneath the sample and flowed out through a pump. A heater, located inside the cold finger, could heat up the cold finger to > 400 K. Two temperature sensors, one close to the gas evaporation point and one close to the sample, allowed to monitor the temperature. In the remainder of this thesis, the reading of the sensor close to the sample is denoted as the cryostat temperature T . The sample was glued or taped with carbon tape on the cold finger and was in vacuum ($\sim 10^{-7}$ hPa). It was connected by wire bonding to RF cables which were fed through the cryostat with two SMA connectors at end. Another RF cable was connected to these and a TEKTRONIX PSPL10300B pulse generator. It was able to produce voltage pulses from 0 - 50 V for time scales between 1 - 100 ns.

Figure 3.5 shows a sketch of the device, located below the KERR microscope. The left pad of the device was connected to the source (labeled by **S**) and the right pad was connected to the ground (labeled by **G**). The resistance of the nanowires was typically a few k Ω . Thus, considering the dimensions of cross section of the conductive layers of the nanowire ($\sim 5 \times 10^{-15}$ m²), the order of magnitude of the current per unit area per pulse was about 1×10^8 A cm⁻² in case of pulses of a few volts. The pulse generator was controlled via another self-written LABVIEW software which also controlled the two different electromagnets. One could apply an in-plane field H_x of -300 - 300 mT. The other could apply an out-of-plane H_z field of -50 - 50 mT.

3.2.3. Method to determine domain wall velocity

Before a DW could be moved by the current pulses, two opposite domains needed to be created, like the ones shown in Figure 3.2. Initially, the whole device had been magnetized in a random direction. By applying a large H_z field, the sample was uniformly magnetized into one direction. A domain inside the nanowire was then created by the combination of an in-plane field H_x and a high current pulse. For that, a small field of a few tens of mT was sufficient which was applied continuously. Then the high current pulse was applied.⁴¹ A domain inside the wire was created which was, depending on the direction of H_x and the current flow, oppositely magnetized to the surrounding as shown in Figure 3.2. Afterwards, by sending more and more pulses, one DW moved into the pad into current flow direction while the other stayed at the other end of the wire. This kind of mechanism can be understood by current-induced switching [103].⁴² Finally, one DW remained at one end in the wire while the second DW was stuck in the pad. Since the

⁴¹ The current pulse needed to be as high as the current needed to achieve nucleation of the DW without H_x .

⁴² Note that due to JOULE heating, the device temperature increased probably close to T_C in the sample.

3. Experimental setup and methods

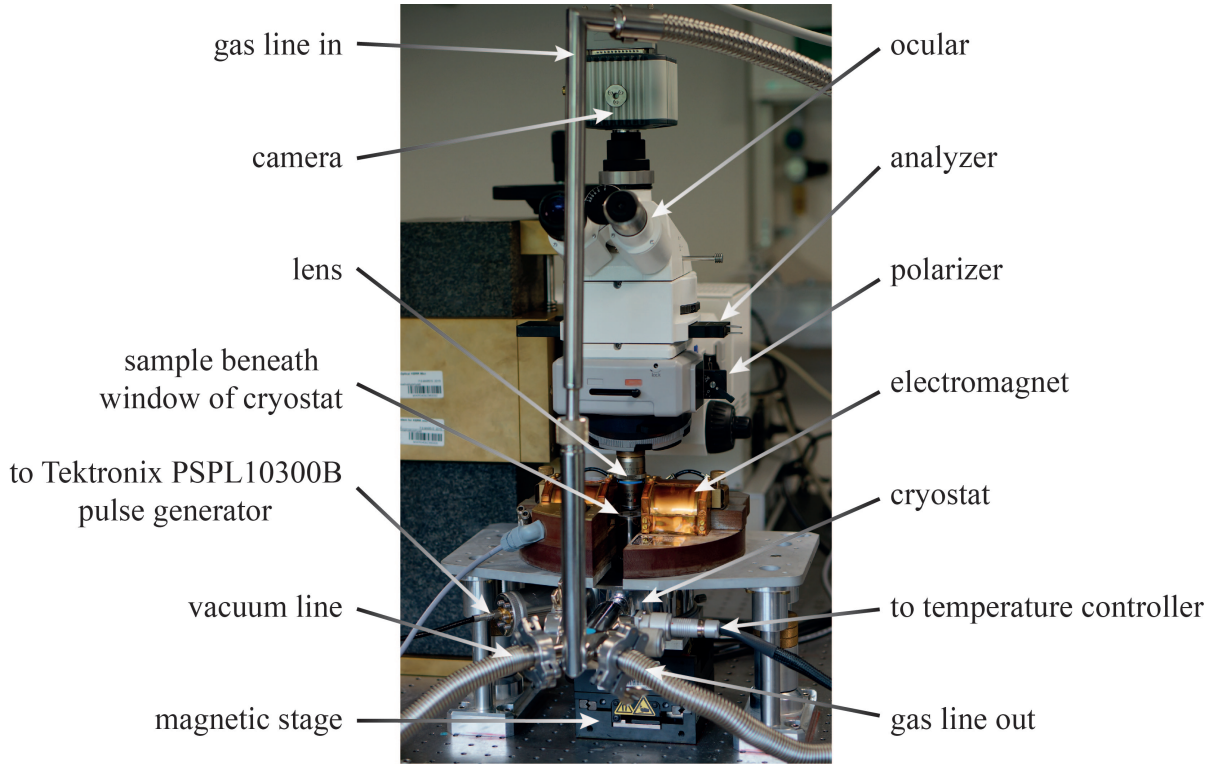


Figure 3.4.: Image of experimental setup. Sample is mounted inside cryostat which sits on magnetic stage to move sample in x - y direction. Sample space is in vacuum. Device sits on cold finger (cf. Figure 3.5) which can be cooled by liquid nitrogen or helium. Gas flow and heater inside cryostat is regulated by temperature controller. Device is connected to voltage pulse generator via high coaxial cable. Domain wall motion can be monitored through KERR microscope. Light is polarized, falls on sample through window in cryostat, is reflected, goes through the analyzer and is captured by camera.

current densities used in the experiment were lower than the current densities used to drive the second DW into the pad, this DW did not move back into the wire.

The DW velocity was then measured as follows. First, a background image was taken. Afterwards, a current pulse of length t_p was sent by the pulse generator and the DW moved by some distance d_1 .⁴³ Using differential KERR microscopy (cf. images in Figure 3.3), the traveled region was now either dark or white. After waiting for a few seconds, the self-written LABVIEW software analyzed the image and calculated the total displacement of the DW d_1 , traveled from the start to the current position. The data point (t_p, d_1) was saved. Afterwards, another pulse was applied. Again, the distance d_2 from the start point to the new position was measured, which was about $2d$ long,⁴⁴ and the data point $(2t_p, d_2)$ was saved. This procedure was repeated, typically for about five times in total. Finally, the DW velocity was calculated by fitting the

⁴³ Sometimes the moving distance of the DW was too short (especially for small current densities). In this case several pulses were applied before measuring d_i .

⁴⁴ Effects like tilting of the DW can lead to $d_1 > d_2/2$ especially in the ferromagnetic sample.

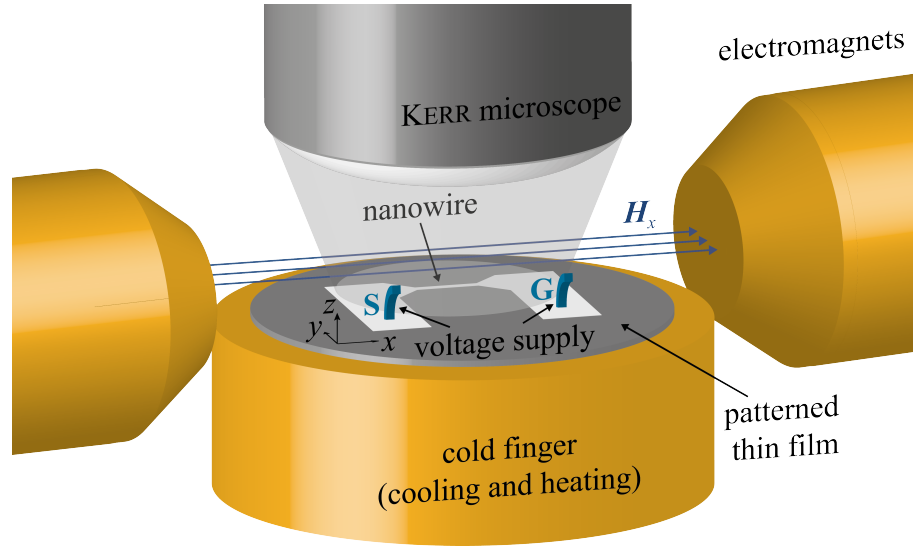


Figure 3.5.: Sketch of experimental setup close to sample. KERR microscope looked at nanowire which was connected by wire bonds (source **S** and ground **G**) to voltage supply. Sample sat on cold finger which could be used for cooling and heating of sample. Electromagnets could supply H_x field from -300 to 300 mT. The setup could also be modified by replacing the electromagnet for H_x field by an electromagnet for H_z field which could supply $-50 - 50$ mT. Note that sample was mounted inside a cryostat (not shown) which was pumped to $\sim 10^{-7}$ hPa.

displacements d_i vs. the pulse lengths it_p . The error by fit was usually less than 5 %.

3.2.4. Method to determine Joule heating

Considering JOULE heating was of crucial importance for the measurement of CIDWM in ferrimagnetic systems. This was because the temperatures T_M and T_A could be only a few tens of Kelvin apart which could be easily exceeded by the current pulses typically applied. It is important to note that several indications led to the conclusion that a reasonable amount of heating appeared in the device: For large current pulses, dependent on the sample, nucleation of several DWs was observed which can be linked to heating up the device close to T_C . This claim is also backed by numerical modeling⁴⁵ and other studies (e.g. [24]). Moreover, if too large currents were applied for a long time, e.g. 3×10^8 A cm⁻² for 100 ns, it could happen that the device started melting at bottlenecks at which the resistance was high. Quantifying the amount of heat by a direct method appeared difficult due to the short pulse lengths of nanoseconds. The method to quantify JOULE heating in this thesis is based on the results of the analytical model.

A short story of the finding of the method might help to understand the principle without looking into the mathematics: In ferromagnetic layers, the DMI field H_{DMI} scales with $1/M_S$. By applying a field H_x , H_{DMI} can be compensated such that the DW velocity drops to zero. Due to

⁴⁵ Confer section B.1 in the appendix.

3. Experimental setup and methods

the change of m_{net} with temperature in the ferrimagnetic Co/Gd bi-layer, a change of the DMI field and the DW velocity dependence on H_x was expected. When the DW velocity dependence on H_x in the ferrimagnetic Co/Gd bi-layer was measured first, indeed at 175 K, no H_x could be observed and the slope ξ of the v vs. H_x curve was zero. Above 175 K, the DW velocity decreased with positive H_x , while below 175 K, the DW velocity increased.⁴⁶ This all satisfied the expectations. However, this measurement was done at a large current density and as soon as a smaller current density was used, this cryostat temperature $T_{\xi=0}$, at which the slope ξ of the H_x dependence was zero, increased. A series of measurements finally led to the findings, presented in the experimental results section 4.3.2.⁴⁷ Based on these findings, the only but very reasonable conclusion was that JOULE heating required that the cryostat temperature needed to be lowered such that no H_x dependence can be observed at this $T_{\xi=0}$. The dependence of $T_{\xi=0}$ on j is approximately $T_{\xi=0} \sim j^2$ such that

$$T_{\xi=0}(j) = -\eta_{\text{heat}} j^2 + T_{\xi=0}(0) \quad (3.1)$$

with η_{heat} being a scaling parameter.

Consequently, in order to quantify the amount of JOULE heating, the slope ξ of the velocity dependence on H_x could be measured at various current densities below a cryostat temperature $T < T_{\xi=0}(0)$. $T_{\xi=0}(0)$ was obtained in the limit of no heating for $j \rightarrow 0$. Then, for a given current density j the temperature $T_{\xi=0}(j)$ at which the slope was flat ($\xi = 0$) had to be found. The temperature difference between $T_{\xi=0}(0)$ and $T_{\xi=0}(j)$ then yielded the temperature increase by JOULE heating $T_{\text{heat}}(j)$:

$$T_{\text{heat}}(j) \stackrel{\text{def}}{=} T_{\xi=0}(0) - T_{\xi=0}(j). \quad (3.2)$$

Finally, the desired device temperature \tilde{T} , which accounted for the JOULE heating, could be calculated by

$$\tilde{T}(j) = T + T_{\text{heat}}(j). \quad (3.3)$$

It shall be noted that this method measured an averaged value of heating reflected in the velocity dependence. Thus, a critical examination of time dependencies of the DW velocity was considered. In section B.2 in the appendix (from [21]), it is shown that with reasonable assumptions the magnetic moments during motion react fast enough on temperature changes. Hence, the DW velocity should have been a good measure to quantify an average effect of heating.

⁴⁶ Cf. Figure 4.11a

⁴⁷ Thorough analytical modeling, discussed in section 2.3.7 in detail, can show that this temperature is supposed to be close to T_A . Also micromagnetic simulations, shown in Figure C.1 in the appendix, confirm that there is an H_x independence at T_A for the given parameters.

3.3. Additional measurement methods

In order to characterize the samples further, additional measurement methods were used. These included the measurement of the threshold field to obtain T_M (section 3.3.1) in the Co/Gd bi-layer, SQUID measurements to obtain $M_S^F(T)$ and $K_{\text{cryst}}^F(T)$ of the Co/Ni/Co sample (section 3.3.2), and X-ray magnetic circular dichroism (XMCD) measurements to show the temperature dependence of m^{Co} and m^{Gd} (section 3.3.3).

3.3.1. Threshold field

As discussed in section 2.3.4, a magnetic field H_z applied in out-of-plane direction can move the DW. Due to dry friction, a threshold field H_{th} as discussed in equation 2.53 hinders the DW to move if $H_z < H_{\text{th}}$. At the same time, the motion depends on m_{net} . If the magnetic moments compensate each other, no field H_z can move the DW.

By measuring H_{th} , the magnetic moment compensation temperature T_M can be obtained. As discussed in section 2.3.8.1, at T_M , H_{th} is expected to diverge. Moreover, the motion direction at $T > T_M$ should be reversed at $T < T_M$ and H_{th} should increase with $1/m_{\text{net}}$ around T_M .

In order to measure the temperature $T_{H_{\text{th}}=\infty}$ at which H_{th} diverges, a domain oppositely magnetized to the surrounding was created inside the nanowire. This domain expanded or shrank depending if $T > T_{H_{\text{th}}=\infty}$ or $T < T_{H_{\text{th}}=\infty}$. In the ferrimagnetic Co/Gd bi-layer, $m^{\text{Gd}}(T)$ was primarily changing within this temperature range (cf. section 2.1.3). Thus, the relation for $H_{\text{th}}^{\text{CoGd}}(T)$ in equation (2.53) can be approximated around T_M by

$$H_{\text{th}}(T) = \pm \frac{h}{T - T_{H_{\text{th}}=\infty}} \quad (3.4)$$

with h as a scaling factor and $T_{H_{\text{th}}=\infty}$ the temperature at which H_{th} diverges.

Using this method, T_M had been determined inside the same setup in which later CIDWM was measured. Therefore, the temperature calibration needed to measure T_M and T_A (cf. last section) was the same, leading to a smaller measurement error caused by the experimental setup. This was a great advantage over other additional measurement methods.

3.3.2. SQUID magnetometer

For the experiments of this thesis, a Magnetic Property Measurement System (MPMS[®]3) of QUANTUM DESIGN was used. The main component of the system is a SQUID magnetometer which is a superconducting quantum interference device (SQUID) to detect the total magnetic moment of a sample. It can detect extremely small changes of magnetic flux ($< 10^{-8}$ emu) within the so-called SQUID “hole” by measuring voltage changes over the SQUID. These changes of the magnetic flux were caused here by the sample. From the voltage changes the magnetization of the sample can be calculated. Furthermore, only changes of the magnetic flux in a certain direction are

3. Experimental setup and methods

relevant which is useful because therefore magnetization-axis dependent measurements (in-plane as well as out-of-plane) can be performed.

The sample which was measured needed to be cut (about $\sim 5 \text{ mm} \times 5 \text{ mm}$) in order to fit through the SQUID “hole”. A piece of the non-patterned area (cf. Figure 3.1) was used. This piece needed to be from the center of the sample because the sputtered layers of the sample could have inhomogeneous at the edges. A motor was then moving the sample piece automatically through the hole. At the same time, a magnetic field was applied to record the hysteresis loop.

As the SQUID measured the magnetic moment of the sample, the magnetization $M_S^F(T)$ and effective anisotropy field $H_{\text{eff,S}}^F(T)$ of the ferromagnetic layer were gained from the hysteresis loop. M_S^F was obtained by dividing the measured magnetic moment (after background subtraction of the signal) by the sample dimensions. $H_{\text{eff,S}}^F(T)$ was the field at which the magnetization curve saturated at high fields. Utilizing equation (2.5), yields K_{eff}^F which then leads to K_{cryst}^F (equation (2.4)).

3.3.3. XMCD

A SQUID measurement could only reveal the magnetic moment of a total layer stack but not the contributions of each layer to the total magnetic moment. However, this information was of interest, particularly in the case of the ferrimagnetic Co/Gd bi-layer. This was because the expected difference in temperature dependence of $m^{\text{Co}}(T)$ and $m^{\text{Gd}}(T)$ led to the appearance of the magnetic moment and angular momentum compensation temperatures T_M and T_A , respectively.

X-ray magnetic circular dichroism (XMCD) can resolve the magnetic moment of each element due to the element specific X-ray absorption. By circularly polarizing the X-ray beam, the absorption is slightly dependent on the direction of the magnetization which can be either parallel or antiparallel to the helicity of the X-ray photon. The subtraction of the spectra obtained by left and right circularly polarized X-rays then reveals the difference in absorption caused by the magnetization.

For the present study, XMCD was used to characterize the temperature dependence of the magnetic moments in the Co/Gd sample. The measurements were performed by Dr. GONG CHEN, ALPHA T. N'DIAYE and PROF. DR. KAI LIU at the ADVANCED LIGHT SOURCE at LAWRENCE BERKELEY NATIONAL LABORATORY in BERKELEY, CALIFORNIA, USA. To measure the magnetic moment of Co, a spectrum around the L_2 and L_3 edge was taken for left and right circularly polarized X-rays. In case of Gd, the M_4 and M_5 edge was measured. The spectra of left and right polarized light were subtracted from each other.⁴⁸ The resulting asymmetry caused by the magnetization was analyzed at different sample temperatures and applied magnetic fields. By comparing the asymmetry of the Co and Gd at different temperatures, the change of m^{Co} and m^{Gd} was measured. Furthermore, hysteresis loops were measured to obtain $H_c^{\text{CoGd}}(T)$ of the Co/Gd sample.⁴⁹

⁴⁸ Exemplary data for Co and Gd is shown in Figure C.7 and C.8 in the appendix, respectively.

⁴⁹ Exemplary hysteresis loops are shown in Figure C.9 in the appendix.

4. Results

This chapter discusses the experimental results of temperature-dependent CIDWM in a ferromagnetic layer system (section 4.1), in a SAF structure (section 4.2), and in a ferrimagnetic bi-layer (section 4.3). The results of the ferrimagnetic bi-layer system are directly compared with the results of the analytical model.

4.1. Ferromagnetic thin film

This section covers the experimental results of temperature-dependent measurements of the magnetic properties (section 4.1.1) of ferromagnetic Pt/Co/Ni/Co thin films as well as CIDWM (section 4.1.2) and threshold current in these films (section 4.1.3).

4.1.1. Temperature dependence of magnetization

In-plane hysteresis loops of a ferromagnetic thin film composed of 15 Pt / 3 Co / 7 Ni / 1.5 Co (units: Å) were measured by SQUID at various temperatures in the range of 50 - 380 K to obtain $M_S^F(T)$ as well as $K_{\text{eff}}^F(T)$ and $K_{\text{cryst}}^F(T)$.⁵⁰ Note that the index F shall indicate the results of the ferromagnetic sample. Figure 4.1a shows the temperature dependence of the saturation magnetization $M_S^F(T)$ of this sample. Within the measured range, the magnetization decreases by approximately 16 % from 485 to 409 kA m⁻¹. The dependence of M_S^F on T appears linear in this regime. To fit the data with equation (2.3), more data at higher T would be required because the error in ε and T_C would be too large. In a very similar Pt/[Co/Ni]₅/Pt system, $\varepsilon = 0.27$ has been measured [119]. Hence, for simplicity, this value is used for fitting the data here. With this, the temperature dependence of magnetization is found to be

$$M_S^F(T) = (492 \pm 5) \text{ kA m}^{-1} \left(1 - \frac{T}{(744 \pm 45) \text{ K}} \right)^{0.27}.$$

Thus, $M_{S,T=0}^F = (492 \pm 5) \text{ kA m}^{-1}$ and $T_C^F = (744 \pm 45) \text{ K}$.

From the in-plane hysteresis loops also the effective field $\mathbf{H}_{\text{eff,S}}^F(T)$ can be determined. By using (2.4) and equation (2.5), $K_{\text{eff}}^F(T)$ and $K_{\text{cryst}}^F(T)$ can be calculated, respectively, which are displayed in Figure 4.1b. $K_{\text{eff}}^F(T)$ decreases approximately linearly with increasing temperature. Since M_S^F is relatively low, it has almost no effect on K_{eff}^F . K_{eff}^F is therefore mainly influenced by K_{cryst}^F . $K_{\text{cryst}}^F(T)$ decreases in the measured temperature range by 41 % from $K_{\text{cryst}}^F(T = 50 \text{ K}) = 0.36 \text{ mJ m}^{-2}$ to $K_{\text{cryst}}^F(T = 380 \text{ K}) = 0.21 \text{ mJ m}^{-2}$.

⁵⁰ Measurement raw data shown in Figure C.3 in the appendix.

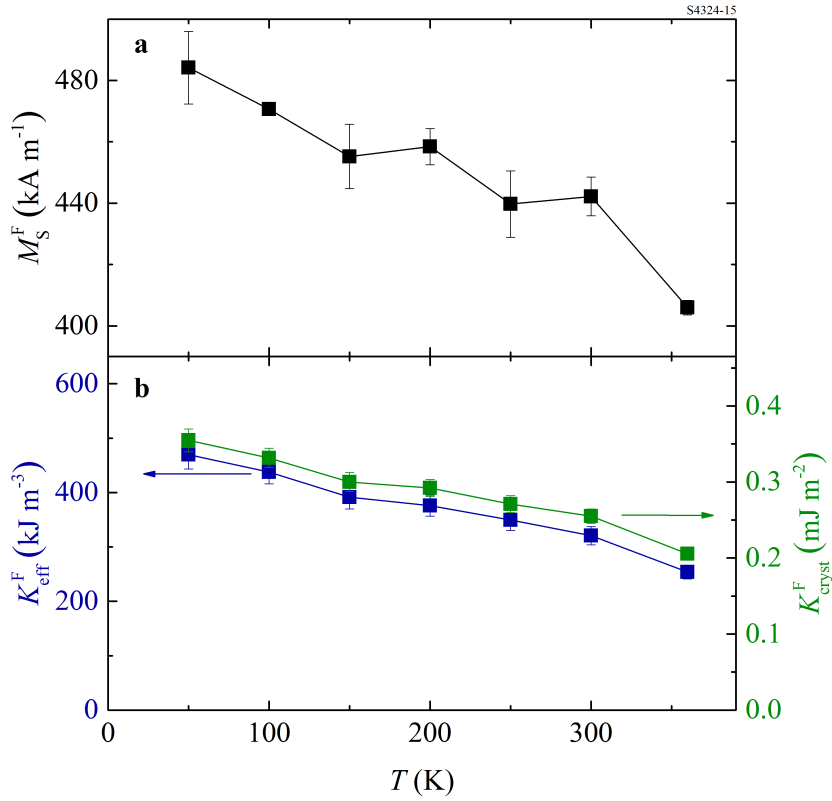


Figure 4.1.: Temperature dependence of magnetic properties of ferromagnetic thin film. **a**, Temperature dependence of saturation magnetization of ferromagnetic thin film M_s^F consisting of 15 Pt / 3 Co / 7 Ni / 1.5 Co (units: \AA). **b**, Effective anisotropy K_{eff}^F and magnetocrystalline surface anisotropy K_{cryst}^F as a function of temperature, respectively. Errors from fit of SQUID data.

4.1.2. Temperature dependence of current-induced domain wall motion

The change of magnetization and anisotropy affects the CIDWM in the ferromagnetic thin film. CIDWM was measured by applying voltage pulses up to 31.5 V of a length of 30 ns at various cryostat temperatures. The resistance of the device was measured in the range $T = 90 - 400$ K. As can be seen in Figure 4.2, the resistance changes by about 4 % in the whole temperature range. As the current density j is the quantity of interest for CIDWM, as discussed in section 2.3.5, the applied voltages are converted into j . Since the change of R is small and a temperature-dependent j would complicate the discussion of the results, R is assumed to be constant. For that, the value of R in the middle of the temperature range, at 250 K, is used which is $R(250 \text{ K}) = 6.84 \text{ k}\Omega$. Hence, the maximum current density of a pulse is of the order $2 \times 10^8 \text{ A cm}^{-2}$. Note that the assumption of constant resistance leads to a slight overestimation/underestimation of the current density at higher/lower temperatures.

Figure 4.3 depicts the DW velocity v^F as a function of j at all measured cryostat temperatures T from 90 K (blue) to 380 K (yellow). The DW does not move if the current is below a certain

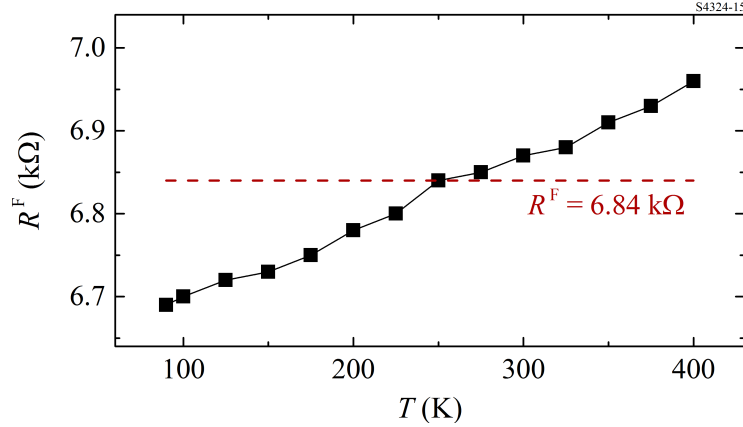


Figure 4.2.: Temperature dependence of resistance of ferromagnetic device.

Device resistance R as a function of temperature T . As the change in the whole temperature range is only 4 %, a constant resistance of $R = 6.84 \text{ k}\Omega$ is assumed.

threshold current, which is the topic of section 4.1.3. Above the threshold current, v^F increases approximately linearly with increasing current density. Due to the threshold current, the curves at lower temperatures are shifted towards higher current densities. The maximum DW velocity of 202 m s^{-1} is measured for a current density of $2.01 \times 10^8 \text{ A cm}^{-2}$ at 380 K. Note that due to the assumption of fixed resistance, v^F is slightly underestimated/overestimated at higher/lower temperatures for a given current density.

In Figure 4.4 the same data is depicted again but v^F is plotted against the cryostat temperature T which highlights how the DW velocity is influenced by the temperature. There is a linear decrease of v^F with decreasing T which appears to be independent of j . This behavior is expected as M_S^F and j_{th}^F increase with decreasing T .

4.1.3. Temperature dependence of threshold current

The threshold current j_{th}^F at the measured cryostat temperatures was obtained by linear fits to the v^F vs. j curves close to $v^F \approx 0$ (Figure 4.3). Additionally, j_{th}^F was measured at values above 380 K up to 440 K. These were obtained by sending a sequence of current pulses to potentially move the DW. The minimum current density, at which a displacement was detected, was considered to be the threshold current density. The problem of measurements at cryostat temperatures above 400 K was that the DW could start moving on its own randomly. This effect can be attributed to thermal excitation of the DW in combination with a low threshold to move the DW. The latter results from a low M_S^F at high T which lowers J_{df}^F as discussed in section 2.3.8.

As can be seen in Figure 4.5, j_{th}^F is at minimum at around 400 K where a plateau is formed. At this cryostat temperature, the threshold current density reaches a minimum of $j_{\text{th,min}}^F = (0.180 \pm 0.002) \times 10^8 \text{ A cm}^{-2}$. Note that above 410 K the threshold current even slightly increases again. As T decreases from 400 K downwards, j_{th}^F increases approximately linearly with

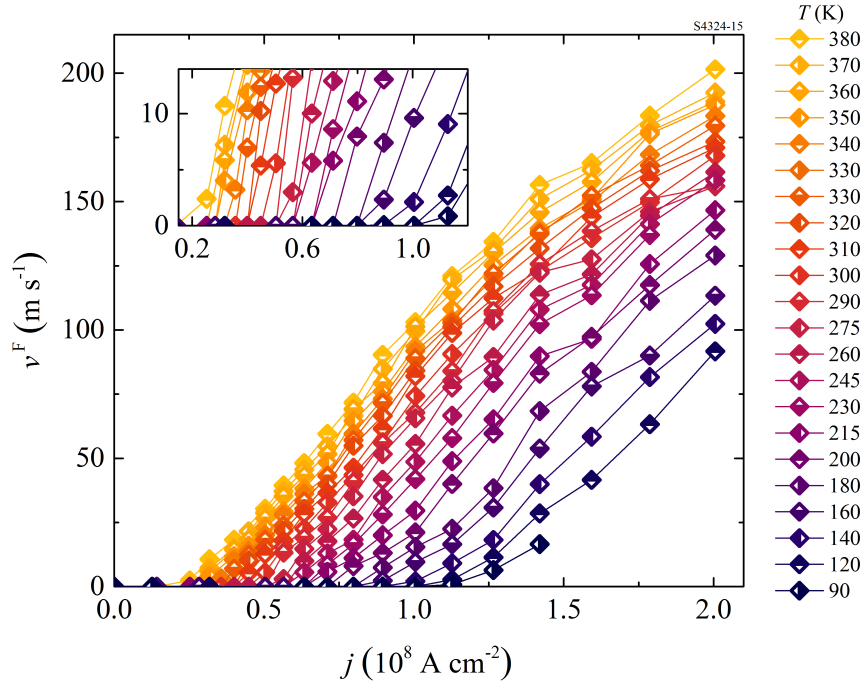


Figure 4.3.: Domain wall velocity dependence on current density at various temperatures in ferromagnetic structure. Constant resistance of $R^F = 6.84 \text{ k}\Omega$ was assumed to convert from voltage to current density. 30 ns-long current pulses used. Error bars ($< 5\%$ for each data point) neglected for clarity. Inset enlarges graph for low velocities to illustrate change of threshold current with temperature. Note that the displayed temperature T is the temperature of the cryostat.

$(0.297 \pm 0.005) \times 10^8 \text{ A cm}^{-2}$ per 100 K. At about 120 K, j_{th}^F exceeds $1 \times 10^8 \text{ A cm}^{-2}$. Note that at such a high current density, JOULE heating becomes relevant. Hence, the actual device temperature \tilde{T} at which $j_{\text{th}}^F(\tilde{T}) = 1 \times 10^8 \text{ A cm}^{-2}$ is much higher than 120 K (probably $> 210 \text{ K}$).⁵¹ \tilde{T} could not be quantified for this ferromagnetic sample but if similar heating is assumed as in the Co/Gd sample, it would become apparent that j_{th}^F actually increases exponentially with decreasing temperature (cf. Figure 5.4).

⁵¹ In section 4.3.3, JOULE heating in the Co/Gd bi-layer is addressed. A current density of $1 \times 10^8 \text{ A cm}^{-2}$ could result in a heating of the device of about 90 K for 10 ns-long pulses.

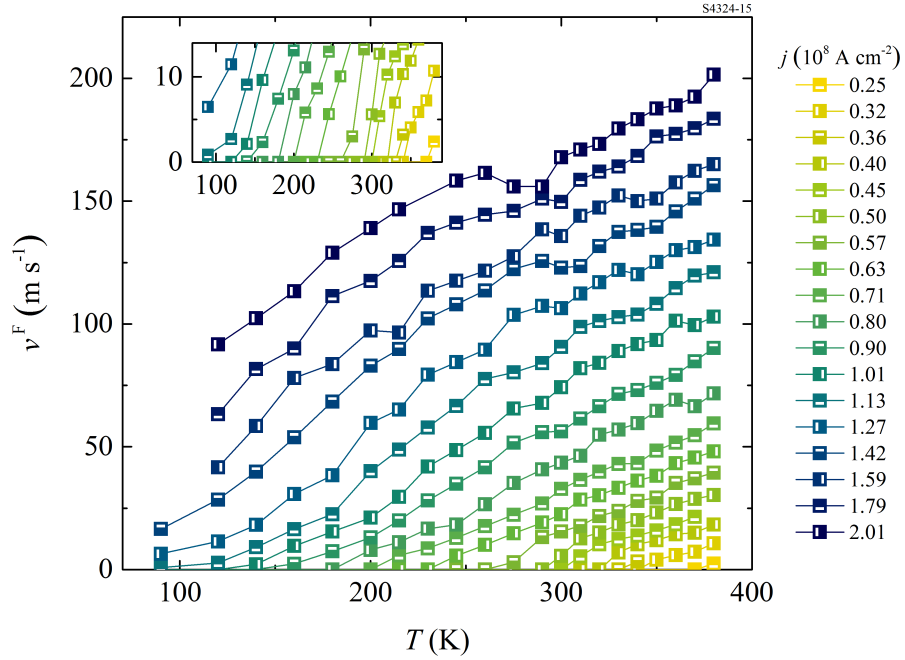


Figure 4.4.: Domain wall velocity dependence on temperature at various current densities in ferromagnetic structure. Heating effects due to current pulses are neglected. Pulse length of 30 ns are used. Note that the displayed temperature T is the temperature of the cryostat.

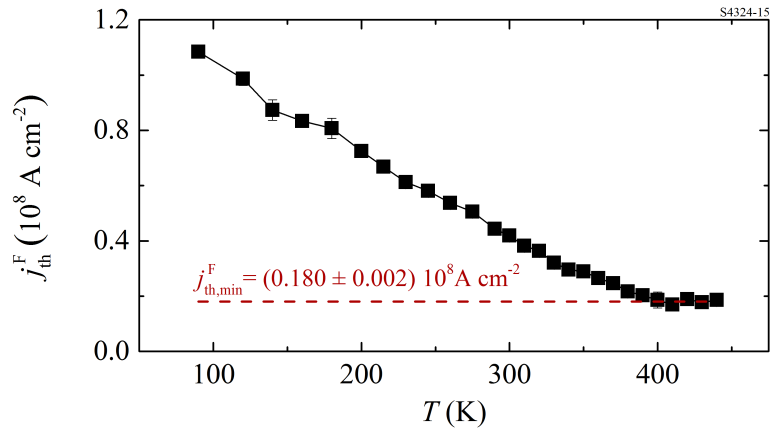


Figure 4.5.: Temperature dependence of threshold current in ferromagnetic structure. Below cryostat temperature $T < 380$ K, the threshold current j_{th}^{F} was obtained by linear fits to data of Figure 4.3. Error bars indicate error of fit. Above 380 K, j_{th}^{F} was solely measured by hand, testing the minimum current density required to move the DW. Errors were obtained by averaging in this range. Data for 30 ns-long pulses.

4.2. Synthetic antiferromagnet

CIDWM in SAF structures has already been studied in [9]. In the present thesis, these results are complemented by taking temperature into account. In section 4.2.1, the effect of temperature on the DW velocity is discussed. Afterwards, section 4.2.2 focuses on the temperature dependence of the threshold current density. Finally, section 4.2.3 covers the influence of H_x on the DW velocity at different temperatures.

4.2.1. Temperature dependence of current-induced domain wall motion

In order to reduce the heating effect, 3 ns-long pulses were used to drive the DWs in this sample. The resistance of the device varied from 3.04 to 3.13 k Ω in the measurement range of $T = 100 - 300$ K. As for the ferromagnetic layer, a constant resistance in the middle of the temperature range is assumed which is 3.08 k Ω . The maximum current density which could be applied was 3×10^8 A cm $^{-2}$ which was limited by the 50 V pulses of the pulse generator.

Figure 4.6 shows the DW velocity v^{SAF} as a function of cryostat temperature T for various current densities. In contrast to the ferromagnetic single layer (Figure 4.4), the DW velocity is almost unaffected by the temperature. On average, v^{SAF} decreases only by (14 ± 5) m s $^{-1}$ per 100 K.⁵² An averaged maximum DW velocity of $v_{\text{max}}^{\text{SAF}} = (657 \pm 40)$ m s $^{-1}$ is measured at 3.01×10^8 A cm $^{-2}$ obtained by fitting the data over the whole temperature range.

4.2.2. Temperature dependence of threshold current

The threshold current density $j_{\text{th}}^{\text{SAF}}$ of the SAF sample for three different pulse lengths $t_p = 3$ ns, 5 ns and 10 ns at temperatures between 100 K and 300 K is shown in Figure 4.7. At room temperature, $j_{\text{th},3\text{ns}}^{\text{SAF}}$ (300 K) in the SAF structure is larger than $j_{\text{th},30\text{ns}}^{\text{F}}$ (300 K) of the ferromagnetic structure. This might be due to the reduced pulse length which is 3 ns in the SAF structure and 30 ns in the Pt/Co/Ni/Co sample. At around 200 K, $j_{\text{th},3\text{ns}}^{\text{SAF}}$ (200 K) and $j_{\text{th},30\text{ns}}^{\text{F}}$ (200 K) are approximately the same. For lower temperatures $j_{\text{th},3\text{ns}}^{\text{SAF}} < j_{\text{th},30\text{ns}}^{\text{F}}$.

By comparing $j_{\text{th}}^{\text{SAF}}$ for different pulse lengths in Figure 4.7, a larger influence can be seen at high temperatures ($\gtrsim 300$ K) but not very much at low temperatures ($\lesssim 200$ K). At 300 K, $j_{\text{th}}^{\text{SAF}}$ increases with decreasing pulse length from $j_{\text{th},10\text{ns}}^{\text{SAF}} = (0.420 \pm 0.001) \times 10^8$ A cm $^{-2}$ to $j_{\text{th},5\text{ns}}^{\text{SAF}} = (0.54 \pm 0.01) \times 10^8$ A cm $^{-2}$ and $j_{\text{th},3\text{ns}}^{\text{SAF}} = (0.63 \pm 0.02) \times 10^8$ A cm $^{-2}$.

By linearly fitting the 3 ns-data, it can be found that $j_{\text{th},3\text{ns}}^{\text{SAF}}(T)$ increases with decreasing T with $(0.07 \pm 0.02) \times 10^8$ A cm $^{-2}$ per 100 K. For a pulse length of 5 ns, $j_{\text{th},5\text{ns}}^{\text{SAF}}(T)$ increases with $(0.12 \pm 0.06) \times 10^8$ A cm $^{-2}$ if the temperature is reduced by 100 K. For a pulse length of 10 ns, $j_{\text{th},10\text{ns}}^{\text{SAF}}(T)$ increases with $(0.18 \pm 0.03) \times 10^8$ A cm $^{-2}$ per 100 K. By extrapolating this trend, these results are in line with results of the ferromagnetic sample in which, for a pulse of 30 ns,

⁵² The slope of v^{SAF} vs T is fitted linearly. The results of the fits at different j is shown in Figure C.6 in the appendix. Around $j \approx 2 \times 10^8$ A cm $^{-2}$, the DW velocity is less affected by T than at higher or lower j . However, there is a large error on these results so that a conclusion is difficult to draw.

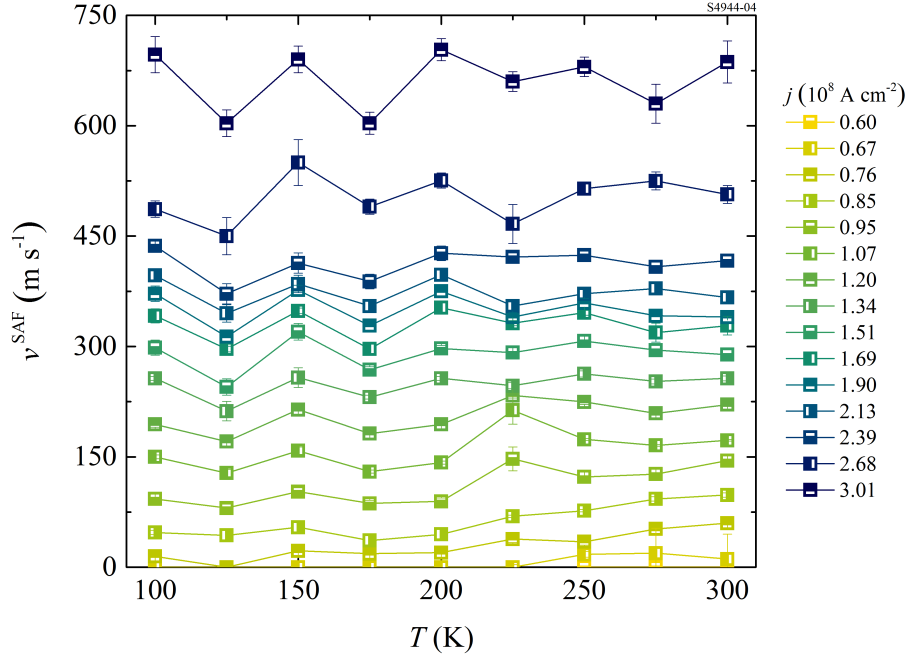


Figure 4.6.: Domain wall velocity dependence on current density at various temperatures in SAF structure. Constant resistance of $3.08 \text{ k}\Omega$ is assumed. Pulse length of 3 ns was used. Errors resulting from averaged measuring of v^{SAF} (section 3.2.3). Note that temperature T denotes the temperature of the cryostat.

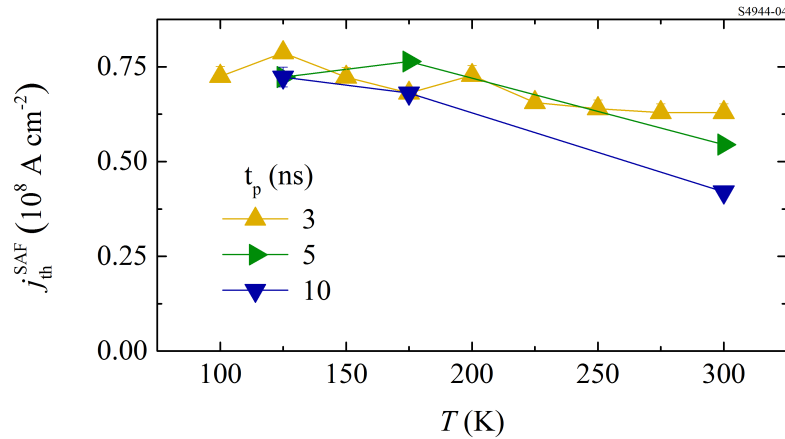


Figure 4.7.: Temperature dependence of threshold current at various pulse lengths in SAF structure. Pulse lengths of 3 ns , 5 ns , and 10 ns measured. Errors below $0.03 \times 10^8 \text{ A cm}^{-2}$ for all data points.

the increase is $(0.297 \pm 0.005) \times 10^8 \text{ A cm}^{-2}$ per temperature reduction of 100 K .

4.2.3. Influence of temperature on H_x dependence of current-induced domain wall motion

The H_x dependence of the DW velocity was measured at $T = 100$ K and at $T = 300$ K. 3 ns-long pulses were used. Due to the discrete scale of the pulse generator and changing resistance $R^{\text{SAF}}(T)$, the current density differed slightly at both temperatures. The current density at $T = 100$ K was higher than at $T = 300$ K resulting in a higher DW velocity. Nevertheless, the interesting behavior to be studied was the response of v^{SAF} to H_x . In Figure 4.8 the measurements result for the DW velocity vs. H_x in the range from -300 mT to 300 mT are depicted.

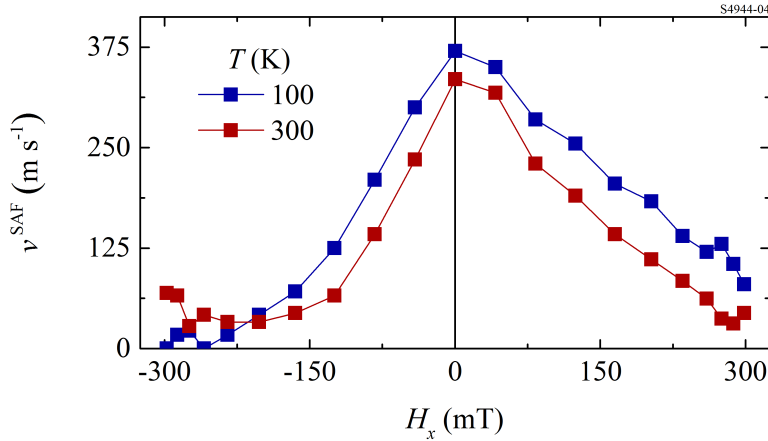


Figure 4.8.: Influence of temperature on H_x dependence of domain wall velocity in SAF structure. $j = 0.94 \times 10^8$ A cm⁻² used for measurement at 100 K and $j = 0.92 \times 10^8$ A cm⁻² used for measurement at 300 K. 3 ns pulse length.

At both temperatures, v^{SAF} drops as $|H_x|$ increases. The curves look like the typical H_x dependence in SAF structures [9]. For the H_x dependence of this DW configuration, towards positive H_x , the drop of v^{SAF} is less steep compared to the drop towards negative H_x which can be attributed to chiral exchange drag effects [28]. The curves at $T = 100$ K and at $T = 300$ K are very similar except that the DW velocity is higher at $T = 100$ K which is due to the higher current density. Consequently, there appears to be no influence of the temperature on the H_x dependence.

4.3. Ferrimagnetic Co/Gd bi-layer

The focus of the study of the Co/Gd bi-layer system is to determine how the DW dynamics differ at certain temperatures which mark different ratios of m^{Gd} to m^{Co} . As discussed theoretically in section 2.1.3, $M_{S,T=0}^{\text{Gd}}$ is expected to be larger than $M_{S,T=0}^{\text{Co}}$ and to exhibit a larger temperature dependence. In case of the right composition determined by t^{Co} and t^{Gd} , the ratio of the magnetic moment of the Gd layer $m^{\text{Gd}}(T)$ and Co layer $m^{\text{Co}}(T)$ changes from a Co dominant regime at high temperatures to a Gd dominant regime at low temperatures. Here, an important focus is on the

difference between magnetic moment compensation at T_M and angular momentum compensation at T_A . The presented results of temperature-dependent CIDWM in the ferrimagnetic Co/Gd bi-layer were published in [21].

4.3.1. Temperature dependence of magnetic properties

In order to investigate the distinct magnetic properties of Co and Gd in the bi-layer, magnetic circular dichroism (XMCD) was used. The Gd $M_{4,5}$ and the Co $L_{2,3}$ peak were measured at various temperatures. Additionally, hysteresis loops were measured at each temperature for both peaks. From these, the coercive field H_c^{CoGd} of the bi-layer (theoretically discussed in section 2.3.8.1) can be obtained. The temperature dependence of H_c^{CoGd} is shown in Figure 4.9a. H_c^{CoGd} increases towards a temperature $T_{H_c=\infty} = 207.5$ K where it is out of measurement range.

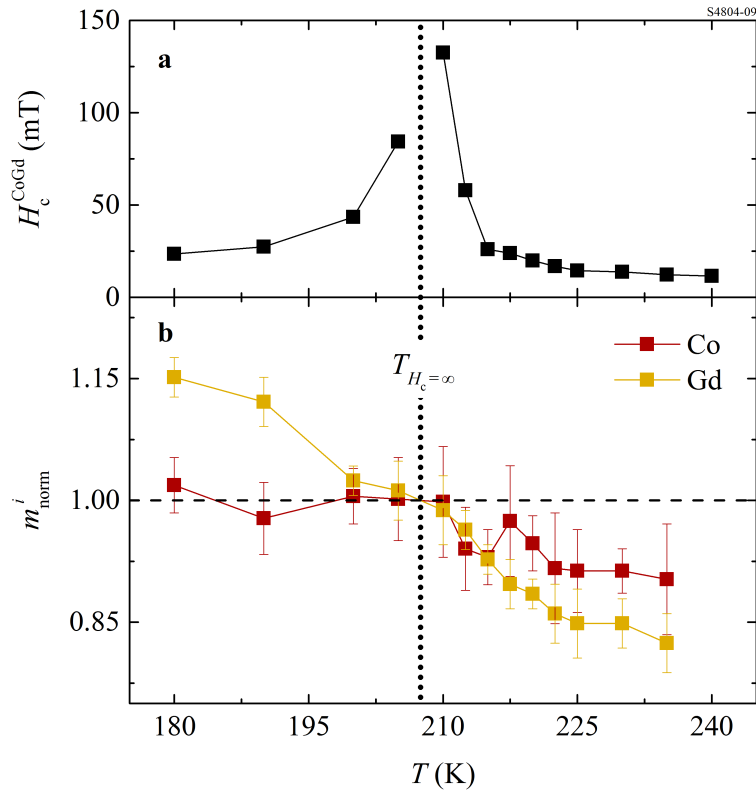


Figure 4.9.: Coercive field and change of magnetic moments in Co and Gd layer with temperature measured by XMCD. Signal intensities measured at Gd $M_{4,5}$ and Co $L_{2,3}$ edges. **a**, Coercive field H_c^{CoGd} obtained by hysteresis loops of Gd layer. H_c^{CoGd} diverges at $T_{H_c=\infty} = 207.5$ K. **b**, Normalized magnetic moments of Co $m^{\text{Co}}(T)$ and Gd $m^{\text{Gd}}(T)$ layer by normalizing peak intensities of XMCD signals to signal at $T_{H_c=\infty} = 207.5$ K (by interpolation between 205 K and 210 K).

4. Results

By comparing the relative change of the measured intensities of the XMCD signal at one peak with temperature, the relative change of the magnetic moments $m^{\text{Co}}(T)$ and $m^{\text{Gd}}(T)$ with temperature was determined.⁵³ The temperature dependence of the individual Co and Gd moments normalized to the moments at $T_{H_c=\infty} = 207.5$ K, denoted as $m_{\text{norm}}^{\text{Gd}}(T)$ and $m_{\text{norm}}^{\text{Co}}(T)$, respectively, is shown in Figure 4.9b. $m_{\text{norm}}^{\text{Gd}}(T)$ exhibits a much larger temperature dependence compared to $m_{\text{norm}}^{\text{Co}}(T)$ in agreement with the theory discussed in section 2.1.3.

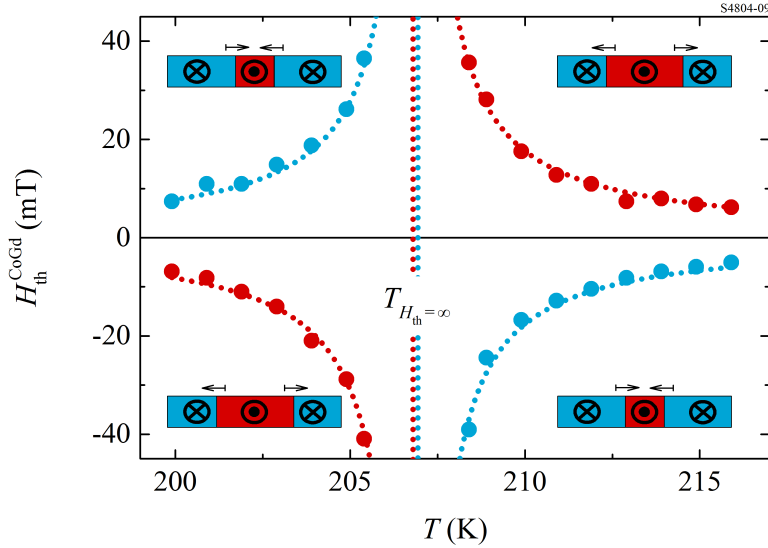


Figure 4.10.: Threshold field as a function of temperature in ferrimagnetic Co/Gd bi-layer. Red and blue symbols indicate threshold field $H_{\text{th}}^{\text{CoGd}}$ (defined in equation (2.53)) for the expansion of a \uparrow domain and \downarrow domain, respectively. Dotted lines are fits to both curves using function (3.4). $T_{H_{\text{th}}=\infty}$ is found to be (206.87 ± 0.06) K by combining both fits.

In order to calibrate the temperature to the measurement setup of CIDWM, the threshold field $H_{\text{th}}^{\text{CoGd}}$ (discussed in section 3.3.1) of the Co/Gd bi-layer was measured inside the setup for CIDWM. The results of the measurement are displayed in Figure 4.10. At a certain temperature $T_{H_{\text{th}}=\infty}$ the threshold field diverges. The DW motion direction of a $\uparrow\downarrow$ and $\downarrow\uparrow$ depends on T : If $T > T_{H_{\text{th}}=\infty}$, a $\uparrow\downarrow$ DW moves towards x while a $\downarrow\uparrow$ DW moves towards $-x$ such that the \uparrow domain expands. If $T < T_{H_{\text{th}}=\infty}$, a $\uparrow\downarrow$ DW moves towards $-x$ while a $\downarrow\uparrow$ DW moves towards x such that the \downarrow domains expands. Note that the notation always refers to the domain and DW configuration of the Co layer here, as discussed in section 2.2.2.

Moreover, $H_{\text{th}}^{\text{CoGd}}$ diverges close to $T_{H_c=\infty}$ measured by XMCD. The measurement for FDDWM was performed with smaller temperature steps so that higher accuracy could be achieved. The data for expansion and shrinking of the domain in Figure 4.10 can be fitted as described in the

⁵³ Also SQUID measurements were performed shown in Figure C.10 in the appendix. However, these do not reveal more information about $m^{\text{Co}}(T)$ and $m^{\text{Gd}}(T)$ as only the net magnetic moment could be measured.

method section 3.3.1 by the function (3.4). Combining the fits to both curves yields

$$T_{H_{\text{th}}=\infty} = (206.87 \pm 0.06) \text{ K}$$

for the temperature at which the threshold field diverges and $h = (55 \pm 1) \text{ T K}$ as a scaling parameter for the fit.

4.3.2. Influence of temperature on H_x dependence of current-induced domain wall motion

Like for the SAF structure (section 4.2.3), the H_x dependence of the DW velocity was measured for the ferrimagnetic Co/Gd bi-layer. In contrast to the SAF structure, the ratios of $m^{\text{Gd}}(T)$ to $m^{\text{Co}}(T)$ change with T as it has been shown in Figure 4.9. Note that a resistance of $R^{\text{CoGd}} = 2.9 \text{ k}\Omega$ is assumed for this device which is the device resistance in the middle of the measurement temperature range.⁵⁴

Figure 4.11a shows an exemplary measurement of the H_x dependence of v^{CoGd} of the ferrimagnetic Co/Gd bi-layer for $j = 0.82 \times 10^8 \text{ A cm}^{-2}$ between $H_x = -300 \text{ mT}$ and 300 mT . The data is shown as circles for $T = 125, 150, 175, 200,$ and 225 K . If the cryostat temperature is as high as $T = 225 \text{ K}$, the velocity of this $\uparrow\downarrow$ DW decreases for positive H_x but increases for negative H_x . As the temperature is reduced, this dependence becomes less. At a certain temperature, which is approximately 175 K in Figure 4.11a, no dependence on H_x can be observed. If the temperature is further lowered, the DW velocity dependence on H_x is reversed compared to the behavior at high temperatures.

Compared to the results of SAF structures in Figure 4.8, v^{CoGd} does not show a decline to both, positive and negative, H_x field directions, even at around $T = 175 \text{ K}$ where no dependence is observed. This could be attributed to the larger interlayer exchange coupling constant J_{ex} in the Co/Gd bi-layer compared to SAF.

Using the parameters summarized in Table 4.1, the same H_x dependence of the DW velocity in a ferrimagnetic bi-layer was simulated by using the analytical model. To fit the experimental data, $\Delta^{\text{CoGd}}, D^{\text{Co}}, K_{\text{df}}^{\text{Co}}, K_{\text{df}}^{\text{Gd}}$ and $\theta_{\text{SH}}^{\text{L}}$ were adjusted.⁵⁵ The resulting H_x dependence of v^{CoGd} for a $\uparrow\downarrow$ DW in the same H_x range as for the experimental data is shown in Figure 4.11b as solid lines. The different ratios of m^{Gd} to m^{Co} shall correspond approximately to the experimental values at the given temperatures in Figure 4.11a.⁵⁶ Here, for $m^{\text{Gd}}/m^{\text{Co}} = 0.47$ and $m^{\text{Gd}}/m^{\text{Co}} = 0.64$, v^{CoGd} decreases with increasing H_x . At $m^{\text{Gd}}/m^{\text{Co}} \approx 0.85$, there is almost no dependence of v^{CoGd} on H_x . As $m^{\text{Gd}}/m^{\text{Co}} = 1.10$ or $m^{\text{Gd}}/m^{\text{Co}} = 1.40$, v^{CoGd} increases with increasing H_x .

⁵⁴ Cf. R^{CoGd} vs. T in Figure C.11 in appendix.

⁵⁵ The fit parameters were also chosen such that the analytical model was in agreement with the experimental data of v^{CoGd} dependence on T , shown in Figure 4.14.

⁵⁶ Based on the results of $m_{\text{norm}}^{\text{Co}}(T)$ and $m_{\text{norm}}^{\text{Gd}}(T)$ by the XMCD measurements, shown in Figure 4.9, and the temperature dependence of the net magnetization of sample measured by SQUID, shown in Figure C.10 in the appendix, the temperature dependence $m^{\text{Gd}}(T)$ and $m^{\text{Co}}(T)$ can be modeled by equation (2.3) (fit results summarized in Table 2.2).

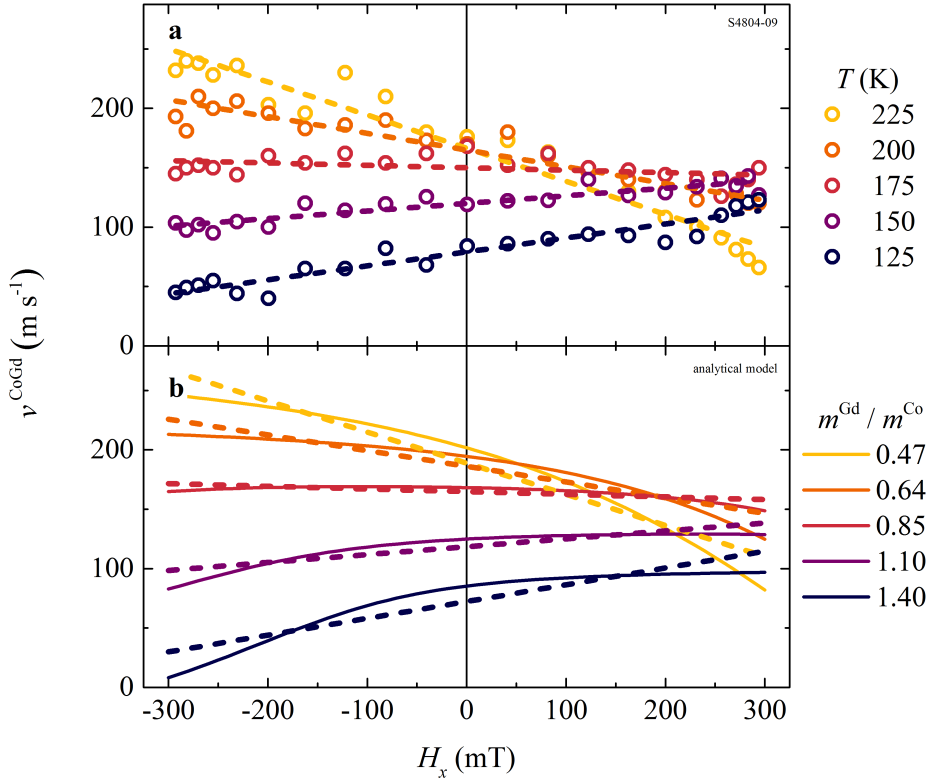


Figure 4.11.: Influence of H_x on current-induced domain wall motion at various temperatures in ferrimagnetic Co/Gd bi-layer. **a**, Experimental results of DW velocity v dependence on H_x at various cryostat temperatures T . Displayed data for 10 ns-long current pulses of $j = 0.82 \times 10^8 \text{ A cm}^{-2}$. Circles: Measured data for DW in $\uparrow\downarrow$ configuration in Co layer. Dashed lines: Linear fits to data. **b**, Results of analytical model for various ratios of the magnetic moment of the Gd layer m^{Gd} to the magnetic moment of the Co layer m^{Co} equivalent to temperatures measured in experiment. Solid lines: Simulation results. Dashed lines: Linear fits to data. Values used for simulation are summarized in Table 4.1.

The H_x dependence of v^{CoGd} can be generally expressed by the slope ξ of the curves at various temperatures. For that, the data was linearly fitted. Figure 4.12 shows the results for the experimental and analytical results. In Figure 4.12a, ξ is plotted against the cryostat temperature T for various applied current densities j . As the current density increases, the temperature $T_{\xi=0}(j)$ where $\xi = 0$ shifts to lower T . At high current densities, there is a larger dependence of ξ on T compared to low current densities.

Figure 4.12b shows the results for ξ at various ratios of the magnetic moment of the Gd to the magnetic moment of the Co layer ($m^{\text{Gd}}/m^{\text{Co}}$) obtained by fitting the simulated data of Figure 4.11b for the same current densities as in the experiment. For the given parameters, $\xi = 0$

Parameter	Value for Co layer	Value for Gd layer
$M_{S,T=0}^i$ (kA m ⁻¹)	1400 ^(a)	1988 ^(a)
T_C^i (K)	600 ^(b)	520 ^(b)
ε^i	1 ^(b)	4 ^(b)
α^i	0.1 ^(c)	0.1 ^(d)
Δ^{CoGd} (nm)	2 ^(e,f)	
D^i (pJ m ⁻¹)	0.2 ^(f)	0 ^(g)
K_{df}^i (T A ⁻¹)	55 ^(f)	0 ^(f,h)
θ_{SH}^i	0.13 ^(f)	0 ⁽ⁱ⁾
J_{ex} (mJ m ⁻²)	-0.9 ^(j)	
g^i	2.2 ^(k)	2.0 ^(k)

Table 4.1.: Values used for analytical model of ferrimagnetic Co/Gd bi-layer. ^(a) From [33]. ^(b) From fit to results of $m^{\text{Co}}(T)$ and $m^{\text{Gd}}(T)$ obtained by XMCD and SQUID. The SQUID data is available in figure C.10 in the appendix. ^(c) From [72]. ^(d) α^{Gd} similar to α^{Co} [120]. ^(e) Obtained by fitting but a magnetocrystalline surface anisotropy of $K_{\text{cryst}} = 0.7 \text{ mJ m}^{-2}$ (comparable to [61]) and an intra-layer exchange coupling constant of $A = 6 \text{ pJ m}^{-1}$ [121] appear reasonable, substantiating this result. ^(f) Obtained by adjusting parameters such that these fit to data in Figure 4.11 and Figure 4.14. ^(g) Assumed no DMI at Gd interface as it has not been reported by any research group. ^(h) Assumed that pinning originates mainly at the Pt/Co interface due to anisotropy defects. ⁽ⁱ⁾ effective spin Hall torque in the Gd layer is very small because current interacts little with $4f$ magnetic moments [108, 109]. ^(j) From [122]. ^(k) Confer Table 2.1.

for any current density exactly at the angular momentum compensation point. In other words, there is no H_x dependence of the DW velocity at $A^{\text{Gd}} = A^{\text{Co}}$ at any current density whatsoever.

This result is in contrast to the experimental data. In the experiment (Figure 4.12a), the temperature $T_{\xi=0}$ at which $\xi = 0$ decreases for increasing j to 131 K for $1.02 \times 10^8 \text{ A cm}^{-2}$. The lowest current density for which $T_{\xi=0}$ can be determined is $0.33 \times 10^8 \text{ A cm}^{-2}$ which is just above the threshold current. For this current density $T_{\xi=0}(0.33 \times 10^8 \text{ A cm}^{-2}) = (210 \pm 1) \text{ K}$ can be obtained by linearly fitting the ξ vs. T curve in Figure 4.12a. Note that this temperature is above $T_{H_{\text{th}}=\infty}$.

4.3.3. Joule heating

In Figure 4.13, $T_{\xi=0}$ is plotted against j . As discussed in the methods section 3.2.4, the shift of $T_{\xi=0}(j)$ to lower temperatures with increasing j is assumed to result from JOULE heating. In this case, it is crucial to determine $T_{\xi=0}(0)$ in order to apply equation (3.1). Since for higher pulse lengths, the threshold current is lower, the pulse length was extended to 100 ns at which $T_{\xi=0}$ was obtained also for j down to $0.13 \times 10^8 \text{ A cm}^{-2}$.

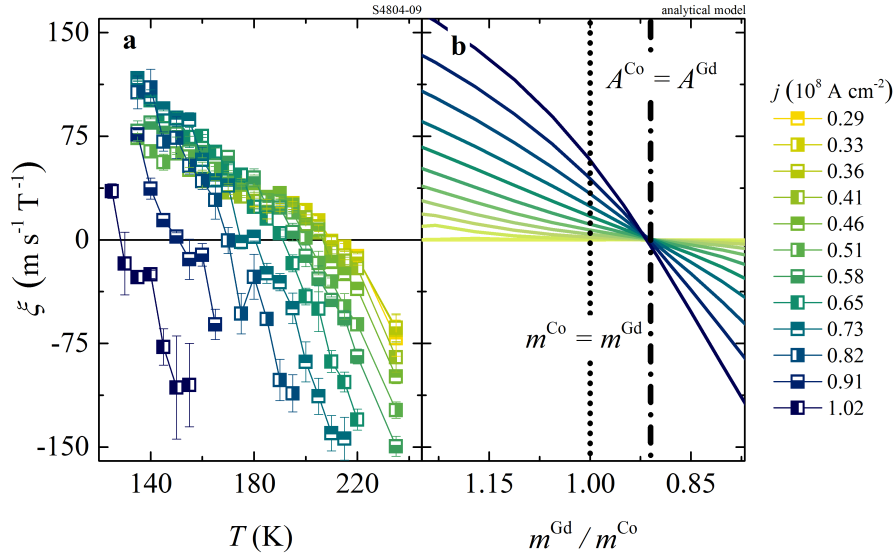


Figure 4.12.: Slope of DW velocity dependence on H_x as a function of temperature of ferrimagnetic Co/Gd bi-layer. Slope ξ obtained by linear fits to DW velocity dependence on H_x like in Figure 4.11. **a**, Experimental data for 10 ns-long pulses. **b**, Slope of simulated data.

At low current densities there is only little difference in $T_{\xi=0}$ for the different pulse lengths. For $j \rightarrow 0$, $T_{\xi=0}$ converges to a temperature $T_{\xi=0}(0)$ which is clearly above $T_{H_{th}=\infty}$, regardless of the pulse length. As the data of the 100 ns-long pulses converges closest to $j = 0$, this data is fitted by the function (3.1). This fit (inset Figure 4.13) yields

$$T_{\xi=0}(0) = (219.1 \pm 0.4) \text{ K}$$

for the temperature at which the slope is zero in the limit of no current and $\eta_{\text{heat},100\text{ns}} = (120 \pm 2) \text{ K}(10^8 \text{ A})^{-2} \text{ cm}^4$ for the scaling parameter of the fit. As described in section 3.2.4, by inserting $T_{\xi=0}(0)$ into equation (3.2) the induced heat T_{heat} can be calculated also for the 10 ns data. $T_{\text{heat}}(j)$ needs to be added to T in order to obtain the actual device temperature \tilde{T} .

It may be noted that as j increases, the difference in $T_{\xi=0}(j)$ becomes more significant for different pulse lengths. This is in line with the interpretation of JOULE heating because a longer pulse leads to additional heat dissipating in the device. This behavior could be verified by numerical modeling canvassed in section B in the appendix.

4.3.4. Temperature dependence of current-induced domain wall motion

The DW velocity was measured at cryostat temperatures between $T = 150 - 250$ K for current densities up to $1.29 \times 10^8 \text{ A cm}^{-2}$ with 10 ns-long pulses. Figure 4.14 shows the measured DW velocity as a function of device temperature \tilde{T} . \tilde{T} was calculated by equation (3.3) in which the

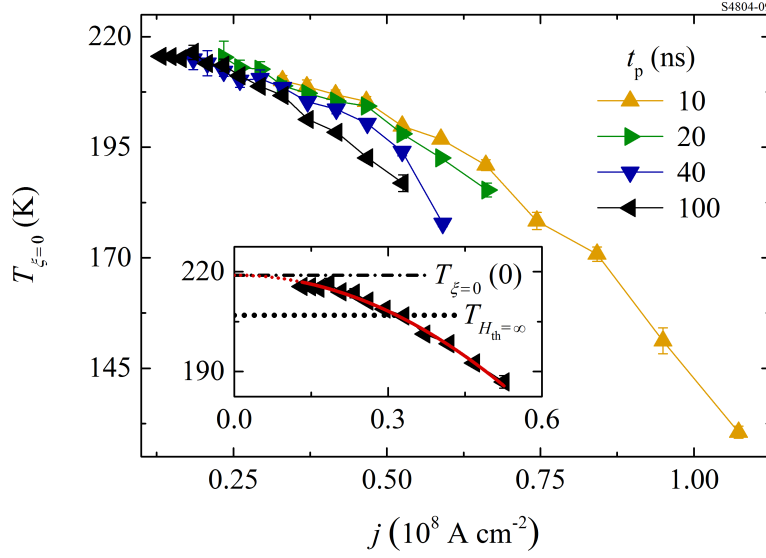


Figure 4.13.: Cryostat temperatures at which no H_x dependence exists as a function of current density of ferrimagnetic Co/Gd bi-layer. Obtained by linearly fitting ξ vs. T data (Figure 4.12 for 10 ns-long pulses) around $\xi = 0$. Error bars indicate fit error. Inset: Quadratic fit (red) to 100 ns data to obtain $T_{\xi=0}(0) = (219.1 \pm 0.4)$ K which is assumed to be T_A . T_A is 12.2 K higher than the temperature $T_{H_{th}=\infty}$ where H_{th}^{CoGd} diverges.

measured values of $T_{\xi=0}(j)$ for the 10 ns data (cf. Figure 4.13) were inserted.

Note that it was observed that just above $T = 250$ K, the DW started to move by itself. Similar observations had appeared for the ferromagnetic Co/Ni/Co sample above 400 K. This might be attributed to thermal fluctuations and low M_S^i of the materials. Below $T = 150$ K pinning of the DWs was very large so that the measurements became more and more unreliable. For $T < 125$ K, the DW scattered into multiple DWs after applying a current pulse. Most probably, $m^{Gd}(T)$ was so large at these temperatures that the demagnetization energy ($-\frac{\mu_0}{2}(m^{Gd})^2$) was larger than the magnetocrystalline surface anisotropy. Consequently, the effective anisotropy became negative, leading to in-plane magnetization.

For low current densities ($j < 0.65 \times 10^8 \text{ A cm}^{-2}$) the DW velocity decreases monotonically as the temperature decreases. This behavior is comparable to that of Co/Ni/Co (Figure 4.4). At higher current densities ($j > 0.65 \times 10^8 \text{ A cm}^{-2}$) the DW velocity exhibits a local maximum at a certain \tilde{T} . This maximum shifts from high temperatures towards lower temperatures as the current density increases. Unfortunately, the heating of the device inherited the complication that the sample had to be cooled further down before sending the current pulse. However, the measurements could not be performed reliably below $T < 150$ K as discussed above. Consequently, the location of the maximum could not be investigated for higher current densities.

The heat adjusted experimental data is compared to the results of the analytical model which

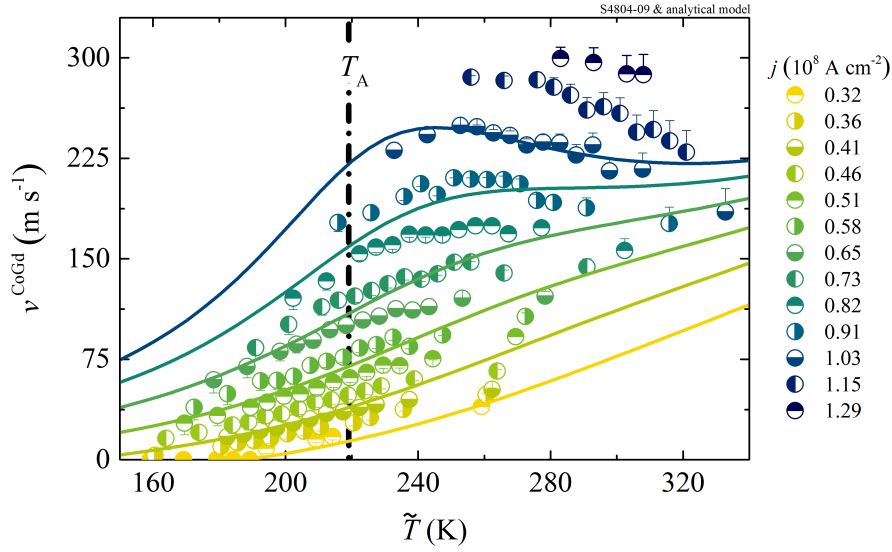


Figure 4.14.: Domain wall velocity dependence on device temperature for various current densities in ferrimagnetic Co/Gd bi-layer. Dots: Experimental data shifted by JOULE heating (equation (3.3)). 10 ns-long pulses used. Constant resistance of $2.9 \text{ k}\Omega$ assumed. Solid lines: Results of analytical model for $j = 0.32, 0.41, 0.51, 0.65, 0.82, \text{ and } 1.03 \times 10^8 \text{ A cm}^{-2}$ (yellow to blue). Values used for simulation are summarized in Table 4.1. $T_{\xi=0}(0)$ is considered to be T_A , here. Temperature dependence of m^{Gd} and m^{Co} was calculated based on values summarized in Table 4.1.

is represented by the solid lines in Figure 4.14. At high \tilde{T} ($\gtrsim 280 \text{ K}$) the DMI-based CST has the major impact as discussed theoretically in section 2.3.6. In order to fit the data, a small J_{DMI} was needed, otherwise the DW velocity in this range would have been overestimated. $D^{\text{Gd}} \approx 0$ was assumed because no DMI has been reported at Co/Gd interfaces so far. $D^{\text{Co}} = 0.2 \text{ pJ m}^{-1}$, which was found by adjusting the curves to the data, seems appropriate.⁵⁷ Note that also the DW width Δ^{CoGd} is a crucial parameter for J_{DMI} but a variation of Δ^{CoGd} has impact on the DW velocity in the whole temperature range.⁵⁸ The value of $\Delta^{\text{CoGd}} = 2 \text{ nm}$ appears small but might be explained by the low saturation magnetization, leading to large K_{eff} . Besides Δ^{CoGd} and D^{Co} , also $K_{\text{df}}^{\text{Co}}$ and $K_{\text{df}}^{\text{Gd}}$ as well as $\theta_{\text{SH}}^{\text{Co}}$ were adjusted which are discussed in the next section.

4.3.5. Temperature dependence of threshold current density

The value of $K_{\text{df}}^{\text{Co}} = 55 \text{ T A}^{-1}$ for the dry friction coefficient in Co was adjusted in a way that it also fits to the experimental results of the ferromagnetic Co/Ni/Co sample (Figure 4.4). As it

⁵⁷ This value is in line with results for a similar system in [18] but differs to the results of [26] by one order of magnitude. In the latter, however, also a larger DW width has been assumed.

⁵⁸ The DW width is assumed not to vary with T as experimentally observed in [24].

was assumed that the pinning majorly arises at the Pt/Co interface, $K_{\text{df}}^{\text{Gd}}$ was assumed to be zero which fitted the data quite well. $\theta_{\text{SH}}^{\text{Co}}$ fitted the data best for 0.13. $\theta_{\text{SH}}^{\text{Gd}}$ was set to zero as discussed in section 2.3.5.2. The combination of J_{df} and J_{SH} , therefore $K_{\text{df}}^{\text{Co}}$ and $\theta_{\text{SH}}^{\text{Co}}$, determines the threshold current.

In the experiment, if the DW velocity v^{CoGd} was plotted against j for various T , the threshold current density in the ferrimagnetic bi-layer $j_{\text{th}}^{\text{CoGd}}$ could be obtained by fitting the data close to $v \approx 0$. In Figure 4.15, $j_{\text{th}}^{\text{CoGd}}$ is plotted against the cryostat temperature T . $j_{\text{th}}^{\text{CoGd}}$ increases from $0.22 \times 10^8 \text{ A cm}^{-2}$ at 250 K to $0.37 \times 10^8 \text{ A cm}^{-2}$ at 150 K. The increase is slightly exponential. Note that at all temperatures, $j_{\text{th}}^{\text{CoGd}}$ is significantly less than $j_{\text{th}}^{\text{SAF}}$ and j_{th}^{F} .

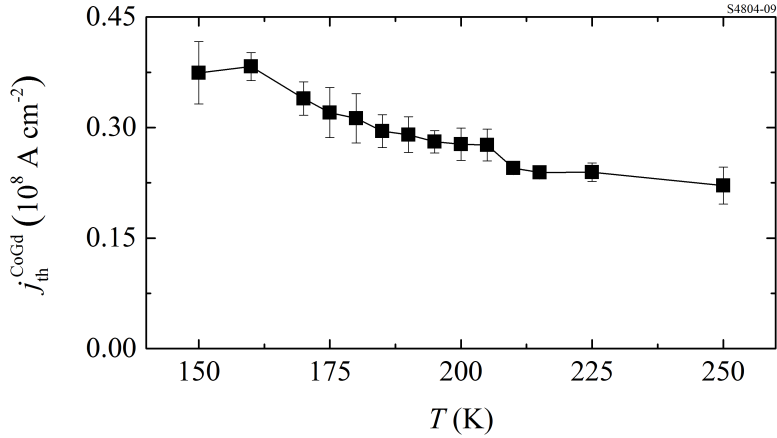


Figure 4.15.: Temperature dependence of threshold current density of ferrimagnetic Co/Gd bi-layer. Threshold current density $j_{\text{th}}^{\text{CoGd}}$ of ferrimagnetic Co/Gd bi-layer as a function of cryostat temperature T for 10 ns-long pulses. Obtained by fitting data of Figure 4.14 close to $v \approx 0$. Error bars from fit. Note that difference between T and \tilde{T} is small (≤ 12 K) for the threshold currents considered here.

5. Discussion

The results of CIDWM at various current densities and temperatures in the Co/Ni/Co ferromagnetic layer system, the SAF layer structure, and Co/Gd ferrimagnetic layer differ considerably. While the domain wall velocity in the Co/Ni/Co (Figure 4.4) and Co/Gd (Figure 4.14) systems exhibits a strong temperature dependence, it is almost unaffected by temperature changes in the SAF structure (Figure 4.6).

The discussion of the experimental results is structured as follows. First, the distinction between T_M and T_A in the ferrimagnetic Co/Gd bi-layer is highlighted in section 5.1. For both quantities, the field dependence of the DW motion plays a key role. The method to obtain T_A has also been used to quantify the effect of JOULE heating as described in section 3.2.4 in the method chapter. These results are examined in section 5.2. Taking the heat effect into account, the temperature dependence of the threshold current density is covered afterwards in section 5.3. The threshold current density affects the efficiency of CIDWM which is the ratio of resulting DW velocity for a given input current density. The temperature dependence of the efficiency is addressed in section 5.4, especially for the ferrimagnetic bi-layer system. The underlying mechanisms for varying efficiency in this bi-layer system are evaluated based on the theoretical model developed in section 2.3.5. The discussion concludes in section 5.5 with the role of the ECT and, particularly, its behavior at the angular momentum compensation point.

5.1. Determination of T_M and T_A

In the ferrimagnetic Co/Gd bi-layer system, $m^{\text{Co}}(T)$ and $m^{\text{Gd}}(T)$ increase with a different rate with decreasing temperature as shown in Figure 4.9b. Hence, two compensation temperatures, the magnetic moment compensation temperature T_M and the angular momentum compensation temperature T_A , exist as described in the theory section 2.1.5.2. In the present thesis, in order to determine T_M and T_A , the DW velocity dependence on magnetic fields in z and x direction has been used, respectively. This section discusses the determination of T_M by FDDWM and the determination of T_A by investigating the influence of H_x on CIDWM.

5.1.1. Field-driven domain wall motion

In a material with PMA, FDDWM refers to the motion of the DW by a field in H_z direction. This section describes how a small H_z has been experimentally utilized to obtain T_M by $H_{\text{th}}^{\text{CoGd}}$ and how a large H_z could be theoretically used to determine T_A .

5.1.1.1. Temperature dependence of threshold field

In section 4.3.1, the results of the threshold field $H_{\text{th}}^{\text{CoGd}}$ is described. Theoretically, it can be seen from equation (2.53) that $H_{\text{th}}^{\text{CoGd}}$ is supposed to diverge if $m_{\text{net}} = 0$ which is the magnetic moment compensation point. This is reflected in the measurements where $H_{\text{th}}^{\text{CoGd}}$ diverges at $T_{H_{\text{th}}=\infty} = (206.87 \pm 0.06)$ K as shown in Figure 4.10. Consequently, it can be concluded that

$$T_{\text{M}} = (206.87 \pm 0.06) \text{ K}.$$

Note that this result is also in line with the divergence of $H_{\text{c}}^{\text{CoGd}}$ measured by XMCD which is linked to $H_{\text{th}}^{\text{CoGd}}$ by equation (2.54).

The dependence of $H_{\text{th}}^{\text{CoGd}}$ can further be discussed for $T \neq T_{\text{M}}$. If no friction was considered, as in equation (2.35), the results in Figure 4.10 could not be explained at $T \neq T_{\text{M}}$ as there is no threshold field in this equation. Thus, a friction mechanism needs to be taken into account to describe the measurement results. Such a friction mechanism could be the dry friction which results from microscopic pinning within the sample. The model is introduced in section 2.3.8. Within this model, the threshold field $H_{\text{th}} = \frac{J_{\text{df}}}{m_{\text{net}}}$ (defined in equation (2.53)) is not only determined by $\frac{1}{m_{\text{net}}}$ but also by the friction energy J_{df} . Close to T_{M} , due to $H_{\text{th}} \sim \frac{1}{m^{\text{Co}}(T) - m^{\text{Gd}}(T)}$ a strong temperature dependence can be found but J_{df} does not vary much in a small temperature range. Therefore, $H_{\text{th}}^{\text{CoGd}}$ is non-zero also at $T \neq T_{\text{M}}$. The dependence of $H_{\text{th}}^{\text{CoGd}}$ with T is in good agreement with the experimental data.⁵⁹

5.1.1.2. Temperature dependence of Walker breakdown

The DW velocity dependence on H_z could also be used to determine T_{A} which can be explained as follows. Away from magnetic moment compensation, if H_z is getting too large, there are no solutions for ϕ^i and only precessional motion is possible ($\dot{q} \neq 0$, $\dot{\phi}^{\text{L}} \neq 0$, and $\dot{\phi}^{\text{U}} \neq 0$). This breakdown of steady state motion is known as the WALKER breakdown described by H_{W} in equation (2.34). The WALKER breakdown is very dependent on the ratio of A^{L} to A^{U} . By solving equations (2.30a), (2.30b), and (2.30c) it can be found that at $A^{\text{L}} = A^{\text{U}}$, a WALKER breakdown does not appear.

In [110] it was shown that for large H_z , the DW velocity is the fastest at the angular momentum compensation temperature T_{A} . This is because for some ratios $A^{\text{U}}/A^{\text{L}}$, $H_z > H_{\text{W}}$ but around $A^{\text{L}} = A^{\text{U}}$, $H_{\text{W}} \rightarrow \infty$ such that $H_z < H_{\text{W}}$. In [110] it was shown that the DW velocity in the precessional regime is given by

$$\langle \dot{q} \rangle = \pm \frac{\Delta (m^{\text{L}} - m^{\text{U}}) (\alpha^{\text{L}} A^{\text{L}} + \alpha^{\text{U}} A^{\text{U}})}{(\alpha^{\text{L}} A^{\text{L}} + \alpha^{\text{U}} A^{\text{U}})^2 + (A^{\text{L}} - A^{\text{U}})^2} H_z$$

where $\langle \dot{q} \rangle$ denotes a time-averaged velocity of the DW into x direction. By finding the temperature

⁵⁹ The dry friction coefficients $K_{\text{df}}^{\text{Co}}$ and $K_{\text{df}}^{\text{Gd}}$ cannot be determined here as the absolute values of $m^{\text{Co}}(T)$ and $m^{\text{Gd}}(T)$ remained unknown.

of maximum DW velocity, T_A was determined in [110]. In the present thesis, v^{CoGd} as a function of H_z could not be measured because the experimental setup did not provide a magnetic field pulse generator. Hence, a different method to determine T_A has been used.

5.1.2. H_x dependence of current-induced domain wall motion

Measuring the dependence of the CIDWM on H_x can help to reveal many information about the sample properties. This section discusses first the validity of the DMI field in a ferrimagnetic sample and afterwards the determination of T_A by the analysis of the DW motion dynamics influenced by the ECT and H_x .

5.1.2.1. Temperature dependence of Dzyaloshinskii-Moriya interaction field in ferrimagnetic bi-layer

The detailed mathematical explanation of the DW velocity dependence on H_x around T_A is given in section 2.3.7. There it is shown that at a certain ratio $\frac{A^U}{A^L} \Big|_{\xi=0}$, linear fitting of the v^{CoGd} vs. H_x curve leads to a slope $\xi = 0$. Many studies investigated also the domain wall velocity in ferrimagnetic systems in presence of a magnetic field in or opposite to the motion direction [17–19, 23, 24, 26]. These consider a divergence of the effective DMI field $H_{\text{DMI}} = \mp D / (\Delta m_{\text{net}})$ at T_M . An infinite DMI field is equivalent to no influence of H_x on the DW velocity such that $\xi = 0$. However, in the present thesis it has been experimentally shown (Figure 4.13) and theoretically substantiated by the analytical model that $T_{\xi=0} > T_M$. Hence, a conclusion about the effective DMI field cannot be drawn from $\xi = 0$.

The reason why there is an H_x dependence at T_M originates from the complex motion dynamics due to the ECT which is not considered in the aforementioned studies. Figure 5.1 highlights this complex interplay which is caused by the coupling of the angles ϕ^L and ϕ^U due to the inter-layer exchange interaction. It shows how the ECT and CST but also the torque created by the H_x field contribute to the final DW velocity v_{total} of this $\uparrow\downarrow$ DW. These results are obtained from the analytical formula (2.44) using the parameters summarized in Table 4.1. By changing the ratio A^L/A^U , the velocity contribution of the ECT v_{ECT}^i changes as well as the contributions of the CST v_{CST}^i and the torque created by the H_x field $v_{H_x}^i$. As can be seen in Figure 5.1a, v_{total} drops to negative H_x but slightly increases to positive H_x at $m^{\text{Co}} = m^{\text{Gd}}$. At angular momentum compensation, shown in Figure 5.1b, the total DW velocity drops slightly and symmetrically to positive and negative H_x . Here, a linear fit results in $\xi = 0$.

This finding makes important contributions to the general understanding of experimental results in ferrimagnetic samples. The misinterpretation of equation (2.45) due to rough estimations can lead to wrong conclusions about the H_x dependence and especially about the effective DMI field typically (and in this case correctly) used for ferromagnetic structures. Due to the strong interplay of the torques, it is indeed complicated to draw conclusions about D^L or D^U in antiferromagnetically coupled systems by measuring the velocity as a function of H_x .

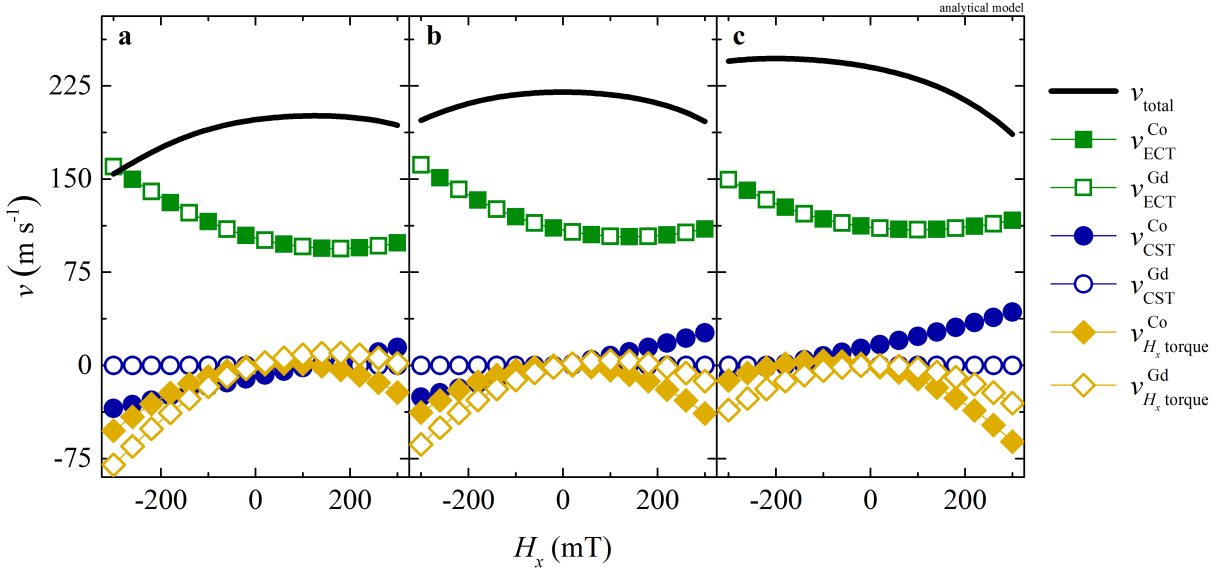


Figure 5.1.: Analytical results of torque contributions to DW velocity depending on H_x . Velocity contributions by equation (2.44) to total DW velocity of a $\uparrow\downarrow$ DW at different ratios m^{Gd} to m^{Co} : **a**, $m^{\text{Gd}} = m^{\text{Co}}$, **b**, $A^{\text{Gd}} = A^{\text{Co}}$, and **c**, $m^{\text{Gd}} = 0.8 m^{\text{Co}}$. Parameters used are summarized in Table 4.1.

5.1.2.2. Temperature dependence of slope

In the present thesis, the H_x dependence of the DW velocity was used to determine the angular momentum compensation temperature T_A as shown in Figure 4.11, 4.12, and 4.13. The temperature $T_{\xi=0}(0)$ at which the H_x independence appears (in the limit of no heating) is found to be (219.1 ± 0.4) K. By assuming that $J_{\text{DMI}}^{\text{Gd}} \ll J_{\text{ex}}$ and $\theta_{\text{SH}}^{\text{Gd}} \ll \theta_{\text{SH}}^{\text{Co}}$ it is shown by equation (2.50) that $\xi = 0$ appears at T_A . Hence,

$$T_A = (219.1 \pm 0.4) \text{ K}$$

is the value obtained for the angular momentum compensation temperature in the studied ferrimagnetic Co/Gd bi-layer sample. This is in line with the temperature dependence of $m^{\text{Co}}(T)$ and $m^{\text{Gd}}(T)$ measured by XMCD (Figure 4.9) where at the same temperature, $m^{\text{Co}}/\gamma^{\text{Co}} \approx m^{\text{Gd}}/\gamma^{\text{Gd}}$.

It is worthwhile noting that the temperature difference between T_M and T_A is only about 12 K. This is relatively small compared to, for example, the temperature difference in a GdFeCo sample for which a difference of T_M and T_A of about 90 K has been reported [110]. The little difference in the Co/Gd bi-layer in the study at hand can be attributed to the relatively rapid change of the Gd moment with temperature (Figure 4.9b). This could potentially originate from the fact that the Gd moments, which are adjacent to the Co layer, experience a proximity induced magnetization. This effect was observed in a similar Co/Gd bi-layer in [26] in which a magnetization of the Gd moments was observed at 300 K although $T_C^{\text{Gd}} = 293$ K for a bulk

sample [54]. The authors of the study [26] approximate that the Gd moments in the first 3 Å adjacent to the Co layer are subject to this proximity induced magnetization at 300 K. As a consequence, for the studied Co/Gd bi-layer in the present thesis, $m^{\text{Gd}}(T)$ is not only dependent on $M_{\text{S}}^{\text{Gd}}(T)$ but also on $m^{\text{Co}}(T)$. Indeed, the critical exponent ε^{Gd} needed to fit the SQUID and XMCD data is about 4 and T_{C}^{Gd} to fit the data is much larger than the bulk value (cf. Table 4.1). Such a high value for ε^{Gd} cannot be found in literature for a pure Gd magnetization dependence on T but could be explained by the proximity induced magnetization in the bi-layer system studied here.

Measuring $T_{\xi=0}(j)$ by the H_x dependence of v was not only used to determine T_{A} in the present thesis but also to quantify the effect of JOULE heating. This is a suitable method because the ratio $\frac{A^{\text{U}}}{A^{\text{L}}}\bigg|_{\xi=0}$ is supposed to be temperature- and current density-independent as shown by equation (2.50). In contrast, in the experiments, a change of $T_{\xi=0}(j)$ with j is observed. A reasonable explanation of the source of this change of $T_{\xi=0}(j)$ could be JOULE heating as discussed in the next section.⁶⁰

5.2. Joule heating

Many studies in the field of CIDWM are interested in the topic of JOULE heating. Its effect in magnetic nanowires has been studied for various pulse lengths and also continuous current.⁶¹ In the nanosecond time regime, JOULE heating was observed, for example in [127] but was not quantified. In [128] it was estimated that a 1 ns-long current pulse of $1 \times 10^8 \text{ A cm}^{-2}$ would heat up the device by about 115 K. The authors also calculated the heat using an analytical model developed in [129] which resulted in a temperature increase of about 68 K for their parameters. Recently, in an experiment, a simplified model to measure the heating in a nanosecond time regime was used [24]. In this study, it was found that the nanowire heats up quickly by about 7 K per nanosecond for a current density of $1 \times 10^8 \text{ A cm}^{-2}$ within the first nanoseconds. For example, for a current density of $1.28 \times 10^8 \text{ A cm}^{-2}$ it was seen that the temperature then saturates at almost 80 K after about 20 ns.

The experimental results of the heat induced by 10, 20, 40, and 100 ns-long current pulses found in the experiments for the thesis at hand are summarized in Figure 5.2. The results here

⁶⁰ The effect of JOULE heating can also be confirmed by measuring the DW velocity dependence on H_z at T_{M} . For that, a constant field H_z is applied which does not move the DW (cf. Figure 4.10). Then a current pulse is sent, the displacement of the DW is measured and the velocity calculated. Due to the insensitivity to H_z at T_{M} , no velocity change by H_z is expected (cf. equation (2.35)). However, Figure C.12 in the appendix shows that the larger the current density, the stronger the dependence on H_z . This result is fully in line with the interpretation of JOULE heating in the device because the larger the current pulse, the more heat is induced into the system, the larger m_{net} and consequently, the stronger the H_z dependence.

⁶¹ For continuous currents a heating of about 5 K at current densities of $0.01 \times 10^8 \text{ A cm}^{-2}$ [123] and 100 K at a current density of $0.6 \times 10^8 \text{ A cm}^{-2}$ is reported [124]. In [125], 10 μs -long current pulses of $2.1 \times 10^8 \text{ A cm}^{-2}$ were applied which resulted in a temperature increase of about 60 K. At low temperatures ($T < 100 \text{ K}$), the heating effect was larger. In this temperature range, the same current pulse led to a temperature increase of 100 K. For 5 μs -long current pulses of $0.67 \times 10^8 \text{ A cm}^{-2}$ and $0.75 \times 10^8 \text{ A cm}^{-2}$ a temperature increase of the device of about 460 K and 540 K, respectively, has been observed [126].

5. Discussion

are in the same temperature range as the theoretical estimations of [128] and [129]. Compared to the experimental results of [24], the results presented here show larger heating which might be due to the difference in the measurement technique. A comparison to the previous studies is additionally complicated as the substrates, underlayers, magnetic materials and thicknesses are different.

The experimental data in Figure 5.2 for each pulse length is fitted by the function

$$T_{\text{heat}} = \eta_{\text{heat}} j^2$$

to obtain the scaling of T_{heat} with j expressed by the scaling parameter η_{heat} .⁶² The inset in Figure 5.2 shows the dependence of η_{heat} on the pulse length t_p . Comparing the 10 ns and 100 ns long pulses, it appears that there is almost twice as much heat induced into the system by the latter. This is an indication that the device continues heating after 10 ns but the main increase of temperature appears within the first 10 ns.

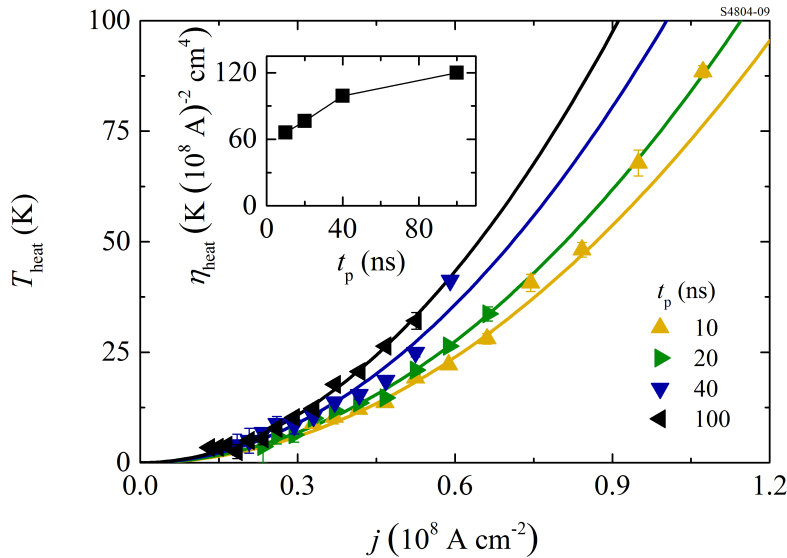


Figure 5.2.: Joule heating as a function of applied current density for 10, 20, 40, and 100 ns-long pulses. Triangles: Experimental data for different pulse lengths. Solid lines: Quadratic fits of the form $T_{\text{heat}} = \eta_{\text{heat}} j^2$ to data where η_{heat} is scaling parameter, plotted against the different pulse lengths t_p in the inset.

To numerically model the JOULE heating for different pulse lengths in the nanowire, COMSOL simulations were performed within the scope of the work for [21] which is linked to this thesis. A detailed discussion about the modeling is given in section B.1 in the appendix. As a result of these simulations, there is a fast increase of temperature within the first two nanoseconds transforming into a slower increase afterwards. The simulation results agree well with the experimental data,

⁶² Note that for high current densities the quadratic fit deviates for the 10 ns. It is possible that reflection of pulses appear at high current densities which could cause an additional heating.

confirming the underlying assumption that solely JOULE heating can explain the shift of $T_{\xi=0}$ to lower temperatures in Figure 4.12.

The η_{heat} dependence on pulse length can be a drawback of the method used here because it means that the measured temperature increase is averaged above the pulse length. Hence, depending on the reaction of the magnetization to temperature changes, the DW motion dynamics could be influenced resulting in complicated dependencies. However, if it is assumed that ϕ^i and $\dot{\phi}^i$ vary slowly with time, averaging the temperature is a valid approximation within the discussed analytical model of chapter 2. A detailed mathematical discussion of this issue can be found in appendix B.2.

Compared to the method used in [24], the method used for the present thesis is indirect. While in [24] the authors try to quantify the heat by measuring the device resistance on very short time scales, here the measurement of \tilde{T} is linked to the measurement of interest - namely to current-induced domain wall motion. Hence, the presented method in the study at hand might be advantageous. By investigating the slope of the DW velocity vs. H_x as a function of temperature even contingent time dependencies are reflected and taken into account.

Overall, quantifying the effect of JOULE heating is crucial for the evaluation of the experimental data as the difference between T_M and T_A is relatively small and could not be evaluated otherwise. Not considering heating might be the reason why other studies find $\xi = 0$ around T_M while their actual device temperature is around T_A . Moreover, a fit of the analytical model to the experimental data as in Figure 4.14 could only be performed when JOULE heating had been taken into account. Since the heat induced by the current is relevant also for small current densities, the nanowire can be subject to heating even at the threshold current density.

5.3. Dependence of threshold current density on temperature

The appearance of a threshold current density is one of the major complications when it comes to the application of devices utilizing CIDWM. The power consumption of such devices would currently be considerably larger than the one of existing technologies. Due to the large dissipation in JOULE heating, the efficiency of converting an electrical current into shifts of magnetic bits is poor. Hence, to understand the origin of the threshold current is of major interest.

5.3.1. Comparison of threshold current in studied samples

Figure 5.3 compares the dependence of j_{th} on T for the ferromagnetic Co/Ni/Co (yellow stars), ferrimagnetic Co/Gd (red diamond) and SAF structure (blue dots). Note that the pulse length is 10 ns for the SAF structure and Co/Gd bi-layer, and 30 ns for the ferromagnetic structure. The threshold current of the Co/Ni/Co sample j_{th}^{F} is close to the threshold current in the SAF structure $j_{\text{th}}^{\text{SAF}}$ at all temperatures. At room temperature, $j_{\text{th}}^{\text{SAF}}$ is equal to j_{th}^{F} . At 175 K and 150 K, the threshold current is about 16 to 24 % lower in the SAF structure, respectively. The threshold current in the ferrimagnetic Co/Gd bi-layer is about half as large as $j_{\text{th}}^{\text{SAF}}$.

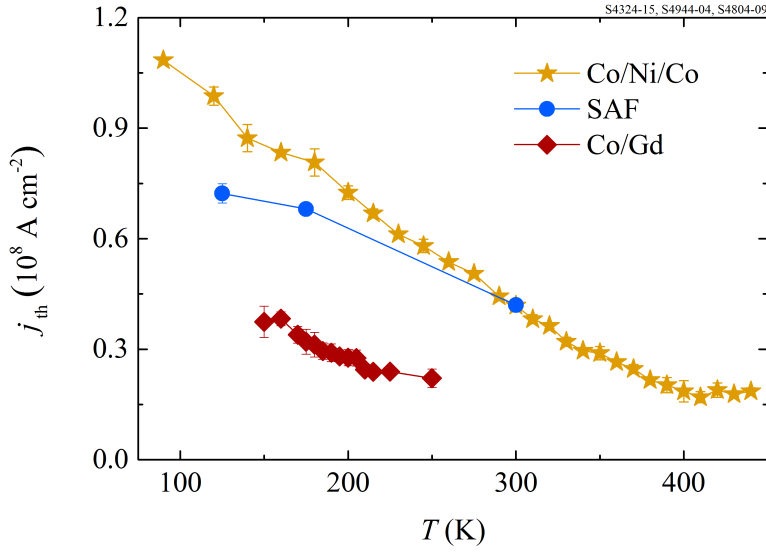


Figure 5.3.: Comparison of threshold current density for ferromagnetic layer, SAF and ferrimagnetic bi-layer structure. Data of SAF structure (blue dots) and ferrimagnetic Co/Gd bi-layer (red diamond) for 10 ns-long pulses. Data for ferromagnetic Co/Ni/Co (yellow stars) for 30 ns-long pulses.

Due to these results it seems as if the temperature dependence of the Co layer adjacent to the Pt layer has a major impact on the threshold current. In the ferrimagnetic Co/Gd bi-layer, the Gd layer leads to a reduced CURIE temperature of the sample which again reduces M_S^{Gd} at a given T compared to M_S^{F} . As j_{th}^{F} is equally low at about 400 K as $j_{\text{th}}^{\text{CoGd}}$ at about 250 K, a similar minimum threshold current for both samples can be observed. The correlation between M_S and j_{th} is further substantiated by the observation that as well at 250 K in the Co/Gd bi-layer as at 400 K in the ferromagnetic structure, the DW starts to move on its own. This might originate from thermal fluctuations which are a manifest of low magnetization. In agreement with this hypothesis, also M_S^{SAF} is slightly less sensitive to T than M_S^{F} which leads to the reduced temperature dependence of $j_{\text{th}}^{\text{SAF}}$. Finally, note that although M_S^{Gd} varies much with temperature (cf. Figure 4.9) this dependence seems to be not reflected in $j_{\text{th}}^{\text{CoGd}}(T)$. Hence, j_{th} could be especially determined by the magnetization in the Co layer at the Pt/Co interface.

5.3.2. Origin of threshold current

While extrinsic pinning of the DW is a likely reason for the origin of the threshold current [113, 130, 131], also intrinsic mechanisms have been theoretically found [132–135]. These intrinsic pinning mechanisms, however, only apply for STT driven domain wall motion which is a minor effect in the present study. Micromagnetic simulations using the LLG SIMULATOR corroborate that extrinsic pinning, such as magnetization and anisotropy defects in the sample, can describe

a similar dependence of the threshold current as observed in the experiment.⁶³ Based on these results, the dry friction model appears to be appropriate to account for extrinsic pinning.⁶⁴

5.3.2.1. Dry friction model

This model dates back to the description of coercive fields by [93]. Based on this model the threshold current j_{th} given by equation (2.55) has been derived. For a single magnetic layer, the equation can be written as

$$j_{\text{th}}^{\text{F}} = \frac{2e}{\hbar} \frac{K_{\text{df}}^{\text{F}} m^{\text{F}2}}{\theta_{\text{SH}}^{\text{F}}}. \quad (5.1)$$

If it is assumed that $\theta_{\text{SH}}^{\text{F}}$ is constant within the measured temperature range, the threshold current density's dependence on T can only come from $K_{\text{df}}^{\text{F}}(T)$ and $m^{\text{F}}(T)$. While $m^{\text{F}}(T)$ was measured by SQUID, shown in Figure 4.1, the temperature dependence of $K_{\text{df}}^{\text{F}}(T)$ is more complex as K_{df}^{F} is attributed to disorder which can dependent again on $m^{\text{F}}(T)$ or on $K_{\text{cryst}}^{\text{F}}(T)$ [113].

As it can be seen in Figure 4.1, $K_{\text{cryst}}^{\text{F}}$ and M_{S}^{F} increase as the temperature decreases. $K_{\text{cryst}}^{\text{F}}$ increases approximately linearly with decreasing T which is a similar behaviour to that found in [119]. $M_{\text{S},T=0}^{\text{F}} = 492 \text{ K}$ is less than the bulk values of Co and Ni shown in Table 2.2. This is typical for magnetic thin films as for example shown in [50]. In the experiments, a CURIE temperature of 744 K was approximated. However, this could be lower as the scaling laws change close to T_{C} (cf. T_{C} of Co and Ni thin films in [50, 136]).

In order to evaluate the scaling of j_{th}^{F} with temperature, JOULE heating has to taken into account because j_{th}^{F} reaches current densities of $1 \times 10^8 \text{ A cm}^{-2}$. The sample thicknesses of the ferromagnetic Co/Ni/Co and ferrimagnetic Co/Gd bi-layer are similar and the conditions of the experiments are equivalent. Hence it can be assumed that approximately the same amount of heat as in the Co/Gd sample (cf. section 5.2) is present in the Co/Ni/Co sample. Since a pulse length of 30 ns was used for the Co/Ni/Co sample for which η_{heat} was not determined, $\eta_{\text{heat},30\text{ns}}$ is interpolated between $\eta_{\text{heat},20\text{ns}}$ and $\eta_{\text{heat},40\text{ns}}$. A value of $\eta_{\text{heat},30\text{ns}} = 87.65 \text{ K}(10^8 \text{ A})^{-2} \text{ cm}^{-4}$ is used and a relative error of 4 % is estimated. By that the curve of Figure 4.5 is adjusted. In Figure 5.4 the threshold current density, normalized to $j_{\text{th}}^{\text{F}}(\tilde{T} = 200 \text{ K})$, is plotted together with $M_{\text{S}}^{\text{F}}(T)^2$, $K_{\text{cryst}}^{\text{F}}(T)$ and $(M_{\text{S}}^{\text{F}}(T)^2 K_{\text{cryst}}^{\text{F}}(T))$, also normalized to $T = 200 \text{ K}$, in order to compare the scaling given by equation (5.1).

If it is assumed that $K_{\text{df}}^{\text{F}}(T) \sim K_{\text{cryst}}^{\text{F}}(T)$, the scaling of threshold current cannot be reproduced as can be seen by comparing $(M_{\text{S}}^{\text{F}}(T)^2 K_{\text{cryst}}^{\text{F}}(T))$ (green curve in Figure 5.4) with $j_{\text{th}}^{\text{F}}(T)$ (black curve). Hence, $K_{\text{df}}^{\text{F}}(T)$ either needs to include a dependence on M_{S}^{F} as well or higher orders of $K_{\text{cryst}}^{\text{F}}$. More detailed studies with varying layer thickness to examine the difference of scaling by M_{S}^{F} and $K_{\text{cryst}}^{\text{F}}$ would be needed. Alternatively, the effect of thermal heat on depinning needs

⁶³ The results are shown in the appendix in Figure C.2.

⁶⁴ Because of the disorder due to the defects, the DW velocity dependence on current density is shifted by j_{th} to higher current densities. In other words, the DW mobility $\varpi(j)$, discussed in section 5.4, is shifted by j_{th} and the efficiency $\epsilon(j)$ is reduced. This differs for example for intrinsic pinning models [133] where the DW velocity with pinning tends to the DW velocity without pinning at high current densities. In this case $\epsilon(j)$ is unaffected by the j_{th} at high j .

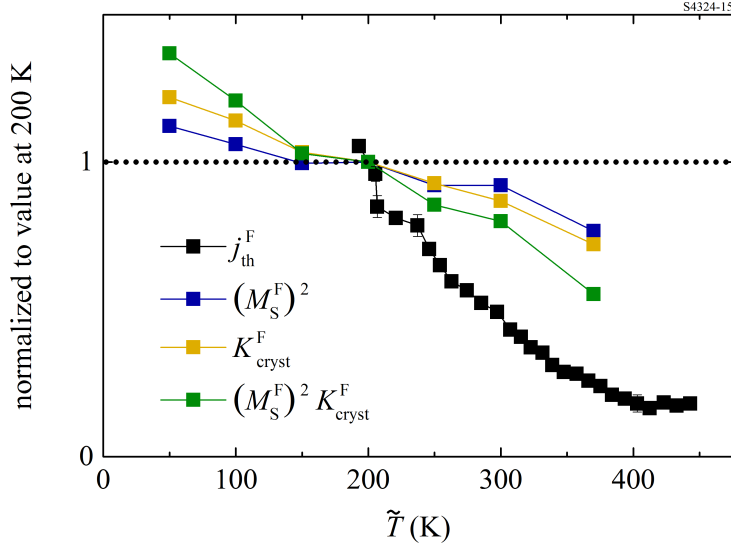


Figure 5.4.: Scaling of threshold current compared with temperature dependence of magnetization and magnetocrystalline surface anisotropy. All curves normalized to value at 200 K. Curve of threshold current j_{th}^{F} is heat adjusted.

to be modeled as it was done by [115]. In fact, in the ferrimagnetic Co/Gd sample it is seen that thermal fluctuations lead to random DW motion above around $T = 250$ K. Interestingly, in the regime $T > 250$ K the threshold current increases again which cannot be explained by the dry friction model. Similar effects are observed for the Co/Ni/Co sample where the threshold current is at minimum around $0.18 \times 10^8 \text{ A cm}^{-2}$ at around 400 K and does not decrease if the temperature is further increased. To account for such a behavior, a random field model, like is was proposed by BROWN [137], could be used to introduce a thermal random motion as well as a kind of fluctuation dissipation [138].

5.3.2.2. Current pulse length dependence

In the SAF structure, the dependence of $j_{\text{th}}^{\text{SAF}}$ on pulse lengths was investigated. As can be seen in Figure 4.7, the pulse length affects the threshold current but only at high temperatures ($T > 175$ K). Although time-dependence of CIDWM was not explicitly investigated in the scope of this thesis, the reason for such a difference could potentially be the relaxation time of $\dot{\phi}$ to reach the equilibrium steady state motion. Also tilting of the DW may be considered [92]. However, the settlement time of both effects scales with M_{S} , which is higher at lower temperatures [92].⁶⁵ Hence, another explanation could be the thermal fluctuations discussed in the last paragraph. It

⁶⁵ The effect of tilting in a ferrimagnetic bi-layer system is described theoretically in section A.3 in the appendix.

In analogy to [92], the settlement time in a ferrimagnetic bi-layer for $\dot{\phi}$ is $t_{\phi} \approx \frac{A_{\text{net}}^2 + (\alpha^{\text{L}} A^{\text{L}} + \alpha^{\text{U}} A^{\text{U}})^2}{(\alpha^{\text{L}} A^{\text{L}} + \alpha^{\text{U}} A^{\text{U}}) J_{\text{DMI}}}$. In contrast, the tilt angle χ settles in a time $t_{\chi} \approx \frac{(\alpha^{\text{L}} A^{\text{L}} + \alpha^{\text{U}} A^{\text{U}}) w^2}{6 \sigma_{\text{DW}} \Delta}$ where w is the wire width and σ the DW energy.

can be assumed that at high temperatures, the DW would move on its own on a small length scale, stopping at a pinning site high enough that thermal fluctuations are not strong enough to overcome it. In the experiments it is observed that for shorter pulse lengths (e.g. 3 ns) the threshold current density is larger than for long pulse lengths (e.g. 10 ns). Since the DW displacement by applying a short pulse is less than for a long pulse, the DW is less distant from the original pinning site where it started if short pulses are applied. Consequently, the probability that the DW falls back into the original pinning site is higher the shorter the pulse length. As a result, it appears that the threshold current density is higher for shorter pulse lengths because only the displacement of the DW (after waiting for a few seconds) is measured.

5.4. Dependence of domain wall mobility on temperature

The observed DW motion efficiency $\epsilon(T, j)$ defined in equation (2.56) is influenced in two ways. Due to the threshold current, ϵ is drastically reduced at low current densities (cf. equation (2.57)). Above the threshold current density, ϵ is primarily influenced by the conversion of current into DW motion by the corresponding torque mechanism. The efficiency of this conversion can be best described by the mobility of the DW ϖ defined in equation (2.41).

The DW mobility of the ferromagnetic Co/Ni/Co, SAF and ferrimagnetic Co/Gd bi-layer structure at a current density of $j = 1 \times 10^8 \text{ A cm}^{-2}$ is displayed in Figure 5.5. It is obtained by linear fits to the v vs. j data around $j = 1 \times 10^8 \text{ A cm}^{-2}$ at the measured temperatures.⁶⁶ Note that the curves are adjusted to JOULE heating.

5.4.1. Comparison of SAF and ferromagnetic Co/Ni/Co structure

The DW mobility in the ferromagnetic sample ϖ^{F} increases slightly with \tilde{T} which can be attributed to reduced M_{S}^{F} at higher temperatures (Figure 4.1). Compared to the mobility ϖ^{SAF} of the SAF structures, the mobility in Co/Ni/Co is almost four times smaller. In order to understand these experimental results, the analytical solutions derived in section 2.3.5.3 are discussed in the following first.

Equation (2.42) is used to describe the steady state DW velocity dependence on j at difference ratios of A^{U} to A^{L} . Note that it assumes large exchange coupling between the upper and lower layers which might be slightly inaccurate for SAF structures. In a single layer, $A^{\text{U}} = 0$ and in SAF, $A^{\text{L}} = A^{\text{U}}$. Note that equation (2.42) does not include the threshold current j_{th} . J_{df} would just lead to an offset for J_{SH} . Hence, the mobility is unaffected by this because it is the derivative of v on j . Furthermore, it is presumed here that α^{Gd} is comparable to α^{Co} [120] which is assumed to be $\alpha^{\text{Co}} \approx 0.1$ [72]. Hence, $\alpha = \alpha^{\text{L}} \approx \alpha^{\text{U}}$ is used. Note that also no temperature dependence of α is assumed as reported for a GdFeCo system around T_{A} [87]. This also holds for

⁶⁶ The v vs j curves of the SAF structure and the ferrimagnetic Co/Gd bi-layer system are shown in Figure C.5 and Figure C.13 in appendix, respectively.

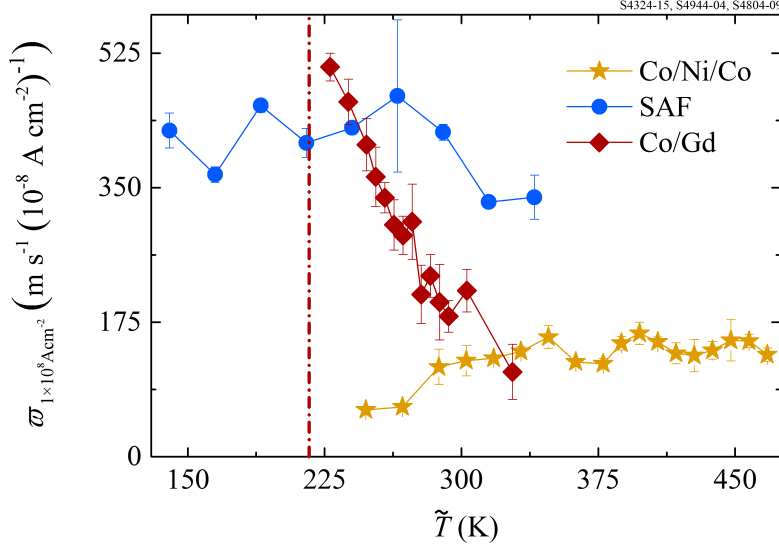


Figure 5.5.: Domain wall mobility as a function of temperature. DW mobility $\varpi(j) = dv(j)/dj$ in Co/Ni/Co (yellow stars), SAF (blue dots) and Co/Gd bi-layer (red diamonds) as a function of device temperature at $j = 1 \times 10^8 \text{ A cm}^{-2}$. DW mobility obtained by linear fits to v vs. j curves (Figure 4.3, and Figure C.5 and Figure C.13 in appendix) around $j = 1 \times 10^8 \text{ A cm}^{-2}$. Error from fit. For Co/Ni/Co sample, only data where $v^F > 0$ was used. Device temperature calculated by $\tilde{T} = T + T_{\text{heat}}$ where $T_{\text{heat}}^F = 88 \text{ K}$, $T_{\text{heat}}^{\text{SAF}} = 40 \text{ K}$ and $T_{\text{heat}}^{\text{CoGd}} = 78 \text{ K}$, which differs due to different pulse length. $T_{\text{heat}}^{\text{CoGd}}$ is obtained from experimental data. T_{heat}^F and $T_{\text{heat}}^{\text{SAF}}$ are estimated by data from Co/Gd sample (Figure 5.2) discussed in section 5.2.

SAF structures since in these both layers consist of the same material. Due to lack of DMI in the upper (Gd) layer, as discussed in section 2.2.3.3, $J_{\text{DMI}}^U \approx 0$.

In case of angular momentum compensation ($A = A^L = A^U$), equation (2.42) then leads to

$$v \Big|_{A^L = A^U} = \frac{\Delta}{2\alpha A} J_{\text{SH}}.$$

The mobility of CIDWM at the angular momentum compensation point is therefore given by

$$\varpi \Big|_{A^L = A^U} = \frac{\Delta \pi \hbar (\theta_{\text{SH}}^L + \theta_{\text{SH}}^U)}{8\alpha A e} \quad (5.2)$$

which is independent of j .

In contrast, in ferromagnetic layers, (or if $A^{\text{Co}} \gg A^{\text{Gd}}$ in the ferrimagnetic Co/Gd bi-layer),

equation (2.42) yields⁶⁷

$$v \Big|_{A^L \gg A^U} = \frac{\Delta}{A^L} \frac{J_{\text{DMI}}^L J_{\text{SH}}}{\sqrt{(\alpha J_{\text{DMI}}^L)^2 + (J_{\text{SH}})^2}}. \quad (5.3)$$

The mobility in the limit $A^L \gg A^U$ is therefore

$$\varpi(j) \Big|_{A^L \gg A^U} = \frac{\Delta \pi \hbar (\theta_{\text{SH}}^L + \theta_{\text{SH}}^U)}{4 \alpha A^L e} \frac{1}{\left[1 + \left(\frac{J_{\text{SH}}(j)}{\alpha J_{\text{DMI}}^L} \right)^2 \right]^{\frac{3}{2}}}. \quad (5.4)$$

Contrary to $\varpi \Big|_{A^L = A^U}$, $\varpi(j) \Big|_{A^L \gg A^U}$ is dependent on j . In the extreme case for $j \rightarrow \infty$ the mobility tends to zero. The reason lies in the decreasing efficiency of the torque created by \mathbf{s} at high current densities. The angle between \mathbf{s} and \mathbf{A}^L is given by

$$\cos(\phi^L) = \frac{\alpha J_{\text{DMI}}^L}{\sqrt{(\alpha J_{\text{DMI}}^L)^2 + (J_{\text{SH}})^2}}.$$

As can be seen, \mathbf{A}^L tends to align along \mathbf{s} as J_{SH} increases, leading to a saturation of DW velocity.

This decrease in mobility with increasing j can be seen in the ferromagnetic sample in Figure 4.3 for high temperatures, for example at $T = 380$ K. By taking the derivative $dv(j)/dj$ at about $0.7 \times 10^8 \text{ A cm}^{-2}$, the mobility is $\varpi^F(380 \text{ K}, 0.7 \times 10^8 \text{ A cm}^{-2}) \approx 144 \text{ m s}^{-1} (10^8 \text{ A cm}^{-2})^{-1}$, while at about $1.6 \times 10^8 \text{ A cm}^{-2}$ the mobility halved to $\varpi^F(380 \text{ K}, 1.6 \times 10^8 \text{ A cm}^{-2}) \approx 73 \text{ m s}^{-1} (10^8 \text{ A cm}^{-2})^{-1}$.

By comparing equation (5.2) and equation (5.4) and using from the experiment (Figure 5.5) that $\varpi^{\text{SAF}} \approx 4 \varpi^F$, the difference of J_{SH}^F to αJ_{DMI}^F can be calculated. If it is assumed that $\Delta^F \approx \Delta^{\text{SAF}}$, $A^F \approx A^L \approx A^U$ (where the latter two are the angular momenta of the lower and upper layer in the SAF structure) and $\theta_{\text{SH}}^U \approx \theta_{\text{SH}}^L \approx \theta_{\text{SH}}^F$, yields that J_{SH}^F in the ferromagnetic thin film must be about 20 % larger than αJ_{DMI}^F . In case of $\theta_{\text{SH}}^U = 0.1 \theta_{\text{SH}}^L$, J_{SH}^F needs to be about 60 % larger than αJ_{DMI}^F . Assuming that $\theta_{\text{SH}}^F \approx 0.13$ and the DW width in the SAF and Co/Ni/Co layer is about 4 - 9 nm, the DMI constant at the Pt/Co interface can be calculated to be approximately $D^F \approx 1 - 3 \text{ pJ m}^{-1}$. This result is one magnetitude larger than the value obtained for D^{Co} in the ferrimagnetic Co/Gd bi-layer system (cf. fit results in Table 4.1). This discrepancy could originate from an additional contribution of the DMI by the Gd layer. This DMI could either effect the DMI in the Co layer or could be created inside the Gd layer. The former case could be explained by the fact that Gd exhibits large spin-orbit coupling like Pt which could induce a DMI at the interface to Co. Unfortunately, such a DMI could not be substantiated in [26]. However, in contrast to the present study, this study neglected the ECT and treated the H_x

⁶⁷ Equation (5.3) can be rewritten to the known form for ferromagnetic layers:

$$v \Big|_{A^L \gg A^U} = \frac{\pi \Delta \gamma^L}{2 \alpha} \frac{H_{\text{DMI}}^L H_{\text{SH,total}}^L}{\sqrt{H_{\text{DMI}}^L{}^2 + \frac{1}{\alpha^2} H_{\text{SH,total}}^L{}^2}}$$

with $H_{\text{DMI}}^L = \frac{D^L}{\Delta m^L}$ and with $H_{\text{SH,total}}^L = \frac{\hbar j}{2 m^L e} (\theta_{\text{SH}}^L + \theta_{\text{SH}}^U)$. Note that in case of a single layer $\theta_{\text{SH}}^U = 0$.

dependence differently. As shown theoretically in section 2.3.7 and discussed in section 5.1.2, this could lead potentially to wrong conclusions about the DMI.

5.4.2. Ferrimagnetic Co/Gd bi-layer

In contrast to the mobility in the SAF and Co/Ni/Co structures, the mobility in the ferrimagnetic Co/Gd bi-layer ϖ^{CoGd} is very temperature dependent. As shown in Figure 5.5, ϖ^{CoGd} increases towards T_A from $\varpi^{\text{CoGd}}(328 \text{ K}) = (110 \pm 36) \text{ m s}^{-1} (10^8 \text{ A cm}^{-2})^{-1}$ to $\varpi^{\text{CoGd}}(228 \text{ K}) = (507 \pm 18) \text{ m s}^{-1} (10^8 \text{ A cm}^{-2})^{-1}$. This dependence is in line with the analytical model. Figure 5.6 shows solutions of the analytical model for the dependence of ϖ^{CoGd} as a function of $m^{\text{Gd}}/m^{\text{Co}}$ for $j = 3 \times 10^8 \text{ A cm}^{-2}$. As can be seen, there is a steep increase of the mobility towards the angular momentum compensation point. This is in line with the experimental data shown in Figure 5.5. The analytical model confirms that the mobility is maximized at angular momentum compensation.

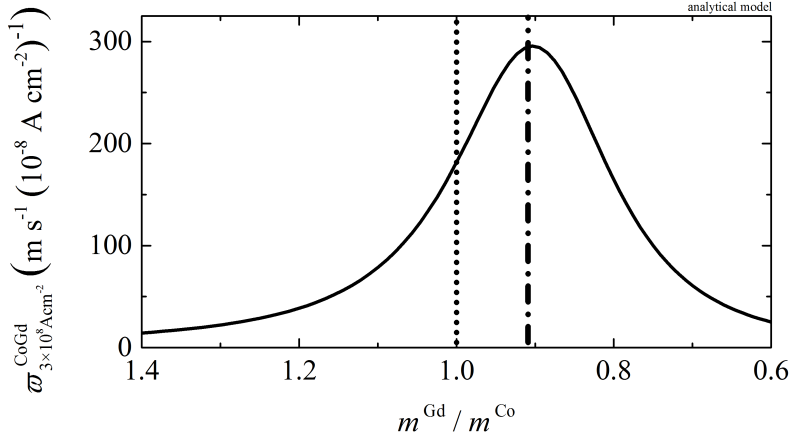


Figure 5.6.: Mobility of DW in ferrimagnetic bi-layer. DW mobility $\varpi = dv/dj$ in ferrimagnetic Co/Gd bi-layer as a function of ratio of magnetic moment of Gd layer m^{Gd} to magnetic moment of Co layer m^{Co} at current density of $j = 3.0 \times 10^8 \text{ A cm}^{-2}$. Dotted line: Magnetic moment compensation where $m^{\text{Gd}} = m^{\text{Co}}$. Dash-dotted line: Angular momentum compensation where $m^{\text{Gd}}/g^{\text{Gd}} = m^{\text{Co}}/g^{\text{Co}}$. Values used for simulation are summarized in Table 4.1.

In the case of $A^{\text{U}} \gg A^{\text{L}}$, the DW velocity is equivalent to the case for $A^{\text{U}} \ll A^{\text{L}}$ only replacing A^{L} by A^{U} , leading to the mobility

$$\varpi(j) \Big|_{A^{\text{L}} \ll A^{\text{U}}} = \frac{\Delta \pi \hbar (\theta_{\text{SH}}^{\text{L}} + \theta_{\text{SH}}^{\text{U}})}{4 \alpha A^{\text{U}} e} \frac{1}{\left[1 + \left(\frac{J_{\text{SH}}(j)}{\alpha J_{\text{DMI}}^{\text{L}}} \right)^2 \right]^{\frac{3}{2}}}.$$

Hence, similar to the case of $A^{\text{U}} \ll A^{\text{L}}$ described by equation (5.4), the DW velocity drops due to decreasing mobility. This is reflected in the decrease of ϖ^{CoGd} in Figure 5.6 for $A^{\text{Co}} < A^{\text{Gd}}$.

Experimentally, the change of mobility with \tilde{T} is also reflected in the DW velocity dependence shown in Figure 4.14. Compared to the Co/Ni/Co sample, the DW velocity does not monotonically decrease with decreasing \tilde{T} in the Co/Gd sample but instead exhibits a maximum of the DW velocity a temperature above T_A for $j > 0.65 \times 10^8 \text{ A cm}^{-2}$. While the decrease of DW velocity with decreasing temperature can be explained by an increase of m^{Co} and m^{Gd} , another mechanism must cause an increase of the velocity at high current densities. This can be explained by the difference in efficiency of the ECT and CST.

5.5. Exchange coupling torque

The mobility dependence on $m^{\text{Gd}}/m^{\text{Co}}$ at large current densities, depicted in Figure 5.6, originates from a change of torque mechanism from CST at $A^{\text{Gd}} \gg A^{\text{Co}}$ or $A^{\text{Gd}} \ll A^{\text{Co}}$ to ECT at $A^{\text{Gd}} = A^{\text{Co}}$. In this last section of the discussion, first the torque contributions of the CST and ECT to the total domain wall velocity are revealed. Afterwards, it is shown how these lead to a maximum of domain wall velocity which shifts from high temperatures towards the angular momentum compensation temperature as the current density increases.

5.5.1. Torque contributions to domain wall velocity

In order to underline that the underlying mechanisms for the increased mobility is indeed the ECT, Figure 5.7 shows how the DW velocity for $j = 3.0 \times 10^8 \text{ A cm}^{-2}$ and $j = 0.4 \times 10^8 \text{ A cm}^{-2}$ is composed at different ratios of m^{Gd} to m^{Co} . These results are obtained analytically from equation (2.44). The total DW velocity (solid lines) is mainly determined by the contributions of the ECT (squares) and CST (circles) - all other contributions are neglected here. The resulting contribution of ECT in the Co (filled symbols) and Gd (open symbols) layer to the total DW velocity is equivalent. This is because the ECT acting on \mathbf{A}^i (defined in equation (2.43)) scales with $1/A^i$ such that the energy available by the exchange coupling to move the DW is independent of A^i . The energy only depends on $J_{\text{ex}} \sin(\phi^{\text{L}} - \phi^{\text{U}})$ which is equal in both layers.⁶⁸

The ECT is only more efficient than the CST at high current densities. This can be seen by comparing Figure 5.7a to Figure 5.7b. The steady decrease of velocity at $j = 0.4 \times 10^8 \text{ A cm}^{-2}$ is due to increasing A^{Co} and A^{Gd} . In contrast, at $j = 3.0 \times 10^8 \text{ A cm}^{-2}$ the ECT becomes especially efficient at $A^{\text{Gd}} = A^{\text{Co}}$ as a result of a maximum in the difference $\phi^{\text{Co}} - \phi^{\text{Gd}}$ at this point. Note that the CST in the bi-layer system is small at any ratio of $m^{\text{Gd}}/m^{\text{Co}}$. This can be attributed to the relatively small energy of J_{DMI} compared to J_{ex} . In the extreme cases $A^{\text{Gd}} \gg A^{\text{Co}}$ and $A^{\text{Gd}} \ll A^{\text{Co}}$ the CST is more relevant. This is because the angle between \mathbf{A}^{Co} and \mathbf{A}^{Gd} becomes smaller making the ECT less efficient. At the same time ϕ^{L} gets larger, resulting in larger CST.

Since the DMI is only assumed to appear at the Pt/Co interface, the contribution of the CST in the Gd layer is always $v_{\text{CST}}^{\text{Gd}} = 0$. The CST in the Co layer highly depends on ϕ^{Co} .

⁶⁸ Note that the DW motion energy is proportional to $A^{\text{L}} + A^{\text{U}}$ such that v decreases with when $m^{\text{Gd}}/m^{\text{Co}}$ increases.

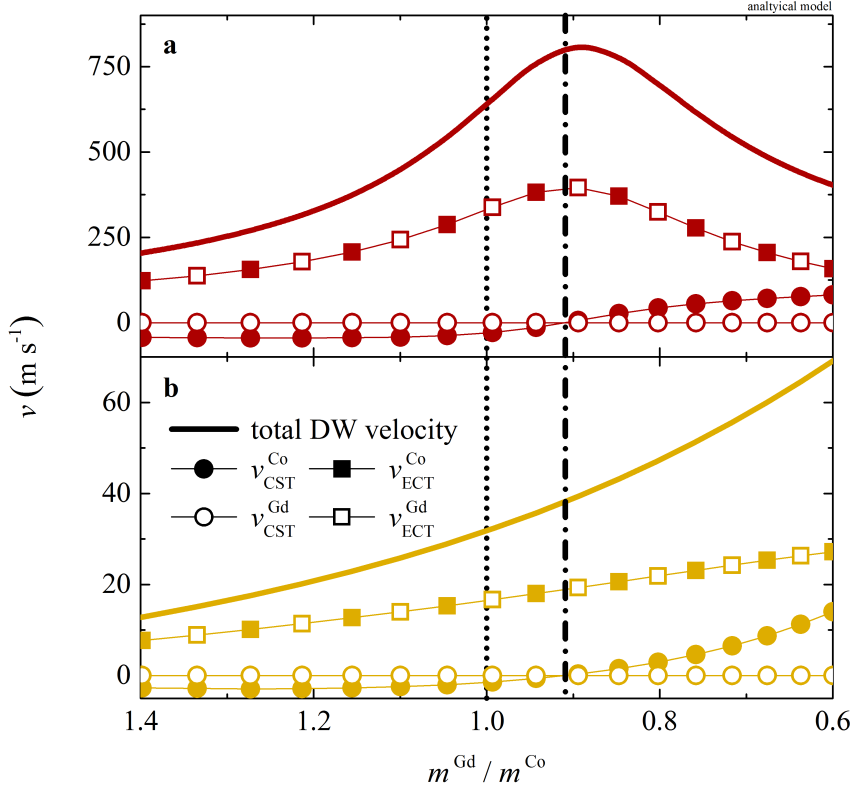


Figure 5.7.: Contributions to total domain wall velocity by CST and ECT as a function of $m^{\text{Gd}}/m^{\text{Co}}$. Total velocity depicted as solid line. Contribution of CST and ECT to total velocity by each layer depicted by symbols. **a** Current density of $j = 3.0 \times 10^8 \text{ A cm}^{-2}$ and **b** $j = 0.4 \times 10^8 \text{ A cm}^{-2}$. Dotted line: Magnetization compensation where $m^{\text{Gd}} = m^{\text{Co}}$. Dash-dotted line: Angular momentum compensation where $m^{\text{Gd}}/g^{\text{Gd}} = m^{\text{Co}}/g^{\text{Co}}$. Values used for simulation are summarized in Table 4.1.

By solving the equations of motion (2.38a), (2.38b) and (2.38c) with $D^{\text{Gd}} = 0$, $\phi^{\text{Co}} = 0$ at the angular momentum compensation point. Hence, the contribution $v_{\text{CST}}^{\text{Co}}$ at $A^{\text{Gd}} = A^{\text{Co}}$ is also zero. Consequently, at $A^{\text{Gd}} = A^{\text{Co}}$ the DW is solely driven by ECT.

5.5.2. Maximum domain wall velocity at angular momentum compensation temperature at high current densities

Theoretically, due to the larger efficiency of the ECT compared to the CST at high current densities, a peak of the DW velocity should appear at T_{A} as it is shown theoretically in Figure 5.7a. In the experiments with the Co/Gd sample used for this thesis, no higher current densities could

be measured to proof the appearance of a peak of the DW velocity exactly at T_A (Figure 4.14).⁶⁹ Because of JOULE heating, a lower initial cryostat temperature ($T < 150$ K) would have been required to measure current densities of $j > 1.3 \times 10^8$ A m⁻². However, at lower temperatures the magnetization of the Gd layer became too large so that the volume shape anisotropy overcomes the magnetocrystalline surface anisotropy (cf. section 2.1.4.3). Consequently, the magnetization started to turned in-plane. In order to demonstrate the expected behavior, Figure 5.8 shows the results of the analytical model, with the given parameters of Table 4.1, also for $j \geq 1.5 \times 10^8$ A m⁻².

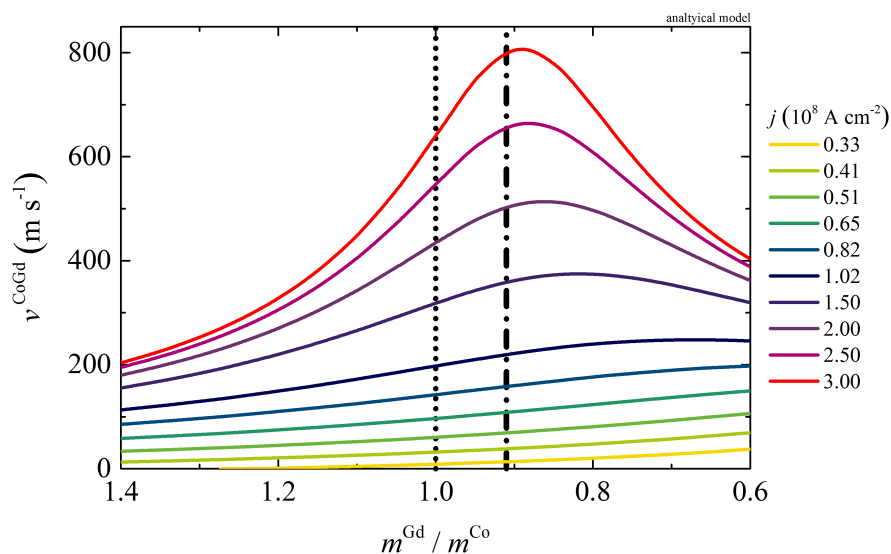


Figure 5.8.: Analytic model results of domain wall velocity as a function of $m^{\text{Gd}}/m^{\text{Co}}$. Dotted line: Magnetic moment compensation where $m^{\text{Gd}} = m^{\text{Co}}$. Dash-dotted line: Angular momentum compensation where $m^{\text{Gd}}/g^{\text{Gd}} = m^{\text{Co}}/g^{\text{Co}}$. Values used for simulation are summarized in Table 4.1.

As can be seen in Figure 5.8, the maximum shifts from a small ratio $m^{\text{U}}/m^{\text{L}}$ towards $A^{\text{U}} = A^{\text{L}}$ as j increases. The same effect is observed in the experiment, shown in Figure 4.14. In order to determine this position of the maximum analytically, equation (2.42) is used. If only changes in A^{U} are considered (substantiated for the experimental results of the Co/Gd bi-layer in Figure 4.9b), equation (2.42) can be differentiated with respect to A^{U} in order to find this local maximum at

⁶⁹ In [24] such a peak of domain wall velocity is shown around T_A where the DW velocity reaches a maximum of about 1.3 km s^{-1} .

5. Discussion

A^{U^*}/A^L .⁷⁰ which then leads to the ratio

$$\frac{A^{U^*}}{A^L} = \frac{J_{\text{SH}}^2 + \alpha^U \alpha^L J_{\text{DMI}}^2}{J_{\text{SH}}^2 - \alpha^U \alpha^L J_{\text{DMI}}^2} \quad (5.5)$$

at which the DW velocity takes a maximum value.

On the one hand, this result shows that as the current density increases the maximum in the DW velocity shifts toward the angular momentum compensation point. On the other hand, if $J_{\text{SH}}^2 < \alpha^U \alpha^L J_{\text{DMI}}^2$ there is no local maximum and the DW velocity monotonically decreases with decreasing temperature.

It is noted that equation (5.5) is derived from equation (2.42) which is an approximation for large exchange coupling. However, if it is assumed that $\theta_{\text{SH}}^U \approx 0$ and $M^L(T)$ is constant, which is valid for the Co/Gd bi-layer to some degree, it can be found that equation (5.5) is the exact solution. In this case it is valid to claim that the DW velocity maximum converges exactly to the angular momentum compensation temperature.

⁷⁰

$$\frac{dq}{dA^U} = - \left\{ \frac{A^{U^*} - A^L}{\left[\frac{\pi}{2} (D^L + D^U)\right]^2} + \alpha^U \frac{A^{U^*} \alpha^U + A^L \alpha^L}{[\Delta (J_{\text{SH}}^U + J_{\text{SH}}^L)]^2} \right\} \times \left\{ \left[\frac{A^{U^*} - A^L}{\frac{\pi}{2} (D^L + D^U)} \right]^2 + \left[\frac{A^{U^*} \alpha^U + A^L \alpha^L}{\Delta (J_{\text{SH}}^U + J_{\text{SH}}^L)} \right]^2 \right\}^{-\frac{3}{2}} = 0$$

which can be solved for A^{U^*} .

6. Conclusion and outlook

The results presented in the thesis at hand highlight the importance of the ECT in the context of CIDWM. It has been experimentally shown and theoretically underlined that at T_A the mobility of DWs in a ferrimagnetic bi-layer is at least as high as in a SAF structure. This can be attributed to the ECT in which a high efficiency persists also at high current densities at T_A in contrast to the CST. The consideration of the ECT is also of major importance for the H_x -dependent CIDWM. Many studies [17–19, 23, 24, 26] presumed that the effective DMI field H_{DMI} diverges at T_M implying that there is no H_x dependence at this temperature. However, it has been experimentally shown in the study at hand that instead there is an H_x dependence at T_M but none at a certain temperature $T_{\xi=0} > T_M$. These findings have been substantiated by the analytical model and $T_{\xi=0}$ is identified to be T_A for the parameters assumed for the ferrimagnetic Co/Gd bi-layer.

In the measured sample, the temperatures T_M and T_A were clearly distinguishable although the difference was only about 12 K. If JOULE heating had not been taken into account, $T_{\xi=0}$ and consequently T_A could have been determined wrongly. This is because a current pulse of a length of $t_p = 10$ ns and current density of $j = 1 \times 10^8$ A cm⁻², which is (to date) a typical current density to move DWs, increases the temperature of the device by about 75 K. The small difference in T_M and T_A compared to other studies (for example 90 K in a GdFeCo alloy [110]) is most likely caused in the present Co/Gd bi-layer by the relatively rapid change of m^{Gd} with T . In order to better distinguish between T_M and T_A in future experiments, alloys or material combinations like Co and Tb with a greater difference in g^i (cf. Table 2.1) could be used in subsequent studies.

JOULE heating is also of major importance for the development of future devices. The energy dissipating into heat shown here is quite large - clearly too high for applications. The need for high current densities to move the bits, represented by the DWs, is majorly driven by the high threshold current density. A minimum threshold current density of around 0.2×10^8 A cm⁻² has been found for the ferrimagnetic Co/Gd bi-layer at 250 K as well as for the ferromagnetic Co/Ni/Co structure at 400 K. Above these temperatures, the threshold current does not further decrease but instead seems to increase again. Future studies should focus on how temperature could lead to some kind of fluctuation friction (cf. e.g. [137, 139]) to explain these results. Moreover, the effect of defects and roughness on j_{th} should be quantified and better understood. The question is whether it was possible to reduce the threshold current without reducing the thermal barrier so that DWs do not move by themselves. It seems that the most straightforward approach to solve this problem is to find materials for underlayers which exhibit a larger spin HALL effect. For real devices of nanometer size, edge roughness will most likely become another issue. Thus, future studies should also investigate the threshold current density at this scale.

6. Conclusion and outlook

In order to better describe the dynamics also in wide wires where the width $w \gg \Delta$, the presented analytical model can be extended by taking the effect of tilting of the DW into account. The effect of tilting by an angle χ could play an important role for the threshold current. This is because the effective DW width is extended and energy is needed for the rotation of the DW by χ . Further investigations of this correlation might also be interesting for future studies. Preliminary measurements have been already performed for this thesis. These show a strong temperature dependence of the DW velocity in a curved wire which can be attributed to tilting of the DW [70]. In order to model this tilt in a ferrimagnetic bi-layer system, an effective quantity approach could be used to extend the DW tilting model of a ferromagnetic layer discussed in [92].⁷¹ Using this model, it can be shown that, in case of extremely large inter-layer exchange coupling, the DW is not supposed to tilt at the angular momentum compensation point. However, the preliminary measurements show that this seems not to be the case.⁷² Hence, the results would need to be substantiated by a comprehensive analytical model which also takes the ECT into account. In addition, more detailed experiments need to be performed to quantify the effect of tilting on the threshold current density.

⁷¹ Cf. section A.3 in the appendix.

⁷² Figure C.14 shows the measurement of the DW velocity in a curved wire for a $\uparrow\downarrow$ and a $\downarrow\uparrow$ DW. The temperature, at which both DWs travel at the same speed through the nanowire, is not T_A .

Bibliography

- [1] S. S. P. Parkin. Shiftable magnetic shift register and method of using the same, December 21 2004. US Patent 6,834,005.
- [2] S. S. P. Parkin, M. Hayashi, and L. Thomas. Magnetic domain-wall racetrack memory. *Science*, 320(5873):190–194, 2008.
- [3] A. A. Khan, F. Hameed, R. Bläsing, S. S. P. Parkin, and J. Castrillon. RTSim: A cycle-accurate simulator for racetrack memories. *IEEE Computer Architecture Letters*, 18(1):43–46, 2019.
- [4] L. Berger. Low-field magnetoresistance and domain drag in ferromagnets. *Journal of Applied Physics*, 49(3):2156–2161, 1978.
- [5] L. Berger. Domain drag effect in the presence of variable magnetic field or variable transport current. *Journal of Applied Physics*, 50(B3):2137–2139, 1979.
- [6] I. Mihai Miron, G. Gaudin, S. Auffret, B. Rodmacq, A. Schuhl, S. Pizzini, J. Vogel, and P. Gambardella. Current-driven spin torque induced by the Rashba effect in a ferromagnetic metal layer. *Nature Materials*, 9(3):230–234, 2010.
- [7] K.-S. Ryu, S.-H. Yang, L. Thomas, and S. S. P. Parkin. Chiral spin torque arising from proximity-induced magnetization. *Nature Communications*, 5:3910, 2014.
- [8] S. Emori, U. Bauer, S. M. Ahn, E. Martinez, and G. S. D. Beach. Current-driven dynamics of chiral ferromagnetic domain walls. *Nature Materials*, 12(7):611–616, 2013.
- [9] S. H. Yang, K. S. Ryu, and S. Parkin. Domain-wall velocities of up to 750 m s^{-1} driven by exchange-coupling torque in synthetic antiferromagnets. *Nature Nanotechnology*, 10(3):221–226, 2015.
- [10] M. A. Ruderman and C. Kittel. Indirect exchange coupling of nuclear magnetic moments by conduction electrons. *Physical Review*, 96(1):99, 1954.
- [11] T. Kasuya. A theory of metallic ferro- and antiferromagnetism on Zener’s model. *Progress of Theoretical Physics*, 16(1):45–57, 1956.
- [12] K. Yosida. Magnetic properties of Cu-Mn alloys. *Physical Review*, 106(5):893, 1957.
- [13] S. H. Yang and S. Parkin. Novel domain wall dynamics in synthetic antiferromagnets. *Journal of Physics-Condensed Matter*, 29(30):303001, 2017.

Bibliography

- [14] S. T. Li, H. Nakamura, T. Kanazawa, X. X. Liu, and A. Morisako. Current-induced domain wall motion in TbFeCo wires with perpendicular magnetic anisotropy. *IEEE Transactions on Magnetics*, 46(6):1695–1698, 2010.
- [15] D. T. Ngo, K. Ikeda, and H. Awano. Direct observation of domain wall motion induced by low-current density in TbFeCo wires. *Applied Physics Express*, 4(9):093002, 2011.
- [16] M. Vanatka, J. C. Rojas-Sanchez, J. Vogel, M. Bonfim, M. Belmeguenai, Y. Roussigne, A. Stashkevich, A. Thiaville, and S. Pizzini. Velocity asymmetry of Dzyaloshinskii domain walls in the creep and flow regimes. *Journal of Physics: Condensed Matter*, 27(32):326002, 2015.
- [17] D. Bang, J. W. Yu, X. P. Qiu, Y. Wang, H. Awano, A. Manchon, and H. Yang. Enhancement of spin Hall effect induced torques for current-driven magnetic domain wall motion: Inner interface effect. *Physical Review B*, 93(17):174424, 2016.
- [18] J. Finley and L. Q. Liu. Spin-orbit-torque efficiency in compensated ferrimagnetic cobalt-terbium alloys. *Physical Review Applied*, 6(5):054001, 2016.
- [19] R. Mishra, J. W. Yu, X. P. Qiu, M. Motapothula, T. Venkatesan, and H. Yang. Anomalous current-induced spin torques in ferrimagnets near compensation. *Physical Review Letters*, 118(16):167201, 2017.
- [20] M. Tanaka, S. Sumitomo, N. Adachi, S. Honda, H. Awano, and K. Mibu. Electric-current-induced dynamics of bubble domains in a ferrimagnetic Tb/Co multilayer wire below and above the magnetic compensation point. *AIP Advances*, 7(5):055916, 2017.
- [21] R. Bläsing, T. Ma, S.-H. Yang, C. Garg, F. K. Dejene, A. T. N’Diaye, G. Chen, K. Liu, and S. S. P. Parkin. Exchange coupling torque in ferrimagnetic Co/Gd bilayer maximized near angular momentum compensation temperature. *Nature Communications*, 9(1):4984, 2018.
- [22] Y. Hirata, D.-H. Kim, T. Okuno, T. Nishimura, D.-Y. Kim, Y. Futakawa, H. Yoshikawa, A. Tsukamoto, K.-J. Kim, S.-B. Choe, and T. Ono. Correlation between compensation temperatures of magnetization and angular momentum in GdFeCo ferrimagnets. *Physical Review B*, 97(22):220403, 2018.
- [23] S. A. Siddiqui, J. Han, J. T. Finley, C. A. Ross, and L. Liu. Current-induced domain wall motion in a compensated ferrimagnet. *Physical Review Letters*, 121(5):057701, 2018.
- [24] L. Caretta, M. Mann, F. Büttner, K. Ueda, B. Pfau, C. M. Günther, P. Helsing, A. Churikova, C. Klose, M. Schneider, D. Engel, C. Marcus, D. Bono, K. Bagschik, S. Eisebitt, and G. S. D. Beach. Fast current-driven domain walls and small skyrmions in a compensated ferrimagnet. *Nature Nanotechnology*, 13(12):1154, 2018.

- [25] M. Vaňatka, J.-C. Rojas-Sánchez, J. Vogel, M. Bonfim, M. Belmeguenai, Y. Roussigné, A. Stashkevich, A. Thiaville, and S. Pizzini. Velocity asymmetry of Dzyaloshinskii domain walls in the creep and flow regimes. *Journal of Physics: Condensed Matter*, 27(32):326002, 2015.
- [26] T. H. Pham, J. Vogel, J. Sampaio, M. Vanatka, J. C. Rojas-Sanchez, M. Bonfim, D. S. Chaves, F. Choueikani, P. Ohresser, E. Otero, A. Thiaville, and S. Pizzini. Very large domain wall velocities in Pt/Co/GdOx and Pt/Co/Gd trilayers with Dzyaloshinskii-Moriya interaction. *Europhysics Letters*, 113(6):67001, 2016.
- [27] K. Ueda, M. Mann, P. W. P. de Brouwer, D. Bono, and G. S. D. Beach. Temperature dependence of spin-orbit torques across the magnetic compensation point in a ferrimagnetic TbCo alloy film. *Physical Review B*, 96(6):064410, 2017.
- [28] S.-H. Yang, C. Garg, and S. S. P. Parkin. Chiral exchange drag and chirality oscillations in synthetic antiferromagnets. *Nature Physics*, 15(6):543, 2019.
- [29] R. Bläsing. Effect of novel exchange-coupling torque and spin-orbit interaction on current-induced domain wall motion in magnetic nanowires. Master’s thesis, Fakultät für Mathematik, Informatik und Naturwissenschaften der Rheinisch-Westfälischen Technischen Hochschule Aachen, 2014. Unpublished.
- [30] A. Thompson and B. N. Taylor. Guide for the use of the international system of units (SI). Technical report, 2008.
- [31] P. A. M. Dirac. On the theory of quantum mechanics. *Proceedings of the Royal Society of London. Series A, Containing Papers of a Mathematical and Physical Character*, pages 661–677, 1926.
- [32] W. Heisenberg. Mehrkörperproblem und Resonanz in der Quantenmechanik. *Zeitschrift für Physik*, 38(6-7):411–426, 1926.
- [33] C. Kittel. *Einführung in die Festkörperphysik*. Oldenbourg Verlag, 2013.
- [34] A. Gangulee and R. J. Kobliska. Mean field analysis of the magnetic properties of amorphous transition-metal–rare-earth alloys. *Journal of Applied Physics*, 49(9):4896–4901, 1978.
- [35] R. Hasegawa, B. E. Argyle, and L.-J. Tao. Temperature dependence of magnetization in amorphous Gd-Co-Mo films. In *AIP Conference Proceedings*, volume 24, pages 110–112. AIP, 1975.
- [36] E. C. Stoner. Collective electron ferromagnetism. II. Energy and specific heat. *Proceedings of the Royal Society of London. Series A, Mathematical and Physical Sciences*, pages 339–371, 1939.

Bibliography

- [37] T. L. Gilbert. A Lagrangian formulation of the gyromagnetic equation of the magnetization field. *Physical Review*, 100:1243, 1955.
- [38] P. J. Mohr, D. B. Newell, and B. N. Taylor. CODATA recommended values of the fundamental physical constants: 2014. *Journal of Physical and Chemical Reference Data*, 45(4):043102, 2016.
- [39] A. Landé. Termstruktur und Zeemaneffekt der Multipletts. *Zeitschrift für Physik*, 15(1-2):189–205, 1923.
- [40] C. Kittel. On the gyromagnetic ratio and spectroscopic splitting factor of ferromagnetic substances. *Physical Review*, 76(6):743–748, 1949.
- [41] M. A. W. Schoen, J. Lucassen, H. T. Nembach, T. J. Silva, B. Koopmans, C. H. Back, and J. M. Shaw. Magnetic properties of ultrathin $3d$ transition-metal binary alloys. I. Spin and orbital moments, anisotropy, and confirmation of Slater-Pauling behavior. *Physical Review B*, 95(13):134410, 2017.
- [42] J. Pelzl, R. Meckenstock, D. Spoddig, F. Schreiber, J. Pflaum, and Z. Frait. Spin-orbit-coupling effects on g -value and damping factor of the ferromagnetic resonance in Co and Fe films. *Journal of Physics: Condensed Matter*, 15(5):S451, 2003.
- [43] J.-M. L. Beaujour, W. Chen, K. Krycka, C.-C. Kao, J. Z. Sun, and A. D. Kent. Ferromagnetic resonance study of sputtered Co/Ni multilayers. *The European Physical Journal B*, 59(4):475–483, 2007.
- [44] A. H. MacDonald. Transition-metal g factor trends. *Journal of Physics F: Metal Physics*, 12(11):2579, 1982.
- [45] W. Low and D. Shaltiel. Paramagnetic-resonance spectrum of gadolinium in single crystals of thorium oxide. *Journal of Physics and Chemistry of Solids*, 6(4):315–323, 1958.
- [46] J. Jensen and A. R. Mackintosh. *Rare earth magnetism*. Clarendon Press Oxford, 1991.
- [47] G. S. Ofelt. Structure of the f^6 configuration with application to rare-earth ions. *The Journal of Chemical Physics*, 38(9):2171–2180, 1963.
- [48] S. J. Yuan, L. Sun, H. Sang, J. Du, and S. M. Zhou. Interfacial effects on magnetic relaxation in Co/Pt multilayers. *Physical Review B*, 68(13):134443, 2003.
- [49] F. Bloch. Zur Theorie des Ferromagnetismus. *Zeitschrift für Physik*, 61(3-4):206–219, 1930.
- [50] C. M. Schneider, P. Bressler, P. Schuster, J. Kirschner, J. J. Demiguel, and R. Miranda. Curie-temperature of ultrathin films of fcc cobalt epitaxially grown on atomically flat Cu(100) surfaces. *Physical Review Letters*, 64(9):1059–1062, 1990.

- [51] B. Legendre and M. Sghaier. Curie temperature of nickel. *Journal of Thermal Analysis and Calorimetry*, 105(1):141–143, 2011.
- [52] L. Ertl, G. Endl, and H. Hoffmann. Structure and magnetic properties of sputtered Tb/Co multilayers. *Journal of Magnetism and Magnetic Materials*, 113(1):227–237, 1992.
- [53] A. F. Holleman. *Lehrbuch der anorganischen Chemie*. Walter de Gruyter, 1995.
- [54] M. Farle, W. A. Lewis, and K. Baberschke. Detailed analysis of the insitu magneto optic Kerr signal of gadolinium films near the Curie-temperature. *Applied Physics Letters*, 62(21):2728–2730, 1993.
- [55] H. Marshak, P. Roman, and W. D. Brewer. Magnetization of single-crystal terbium at very low temperatures by nuclear orientation. *Hyperfine Interactions*, 50(1-4):741–748, 1989.
- [56] E. A. Nesbitt and J. H. Wernick. *Rare earth permanent magnets*. Academic Press, 1973.
- [57] G. H. O. Daalderop, P. J. Kelly, and F. J. A. Den Broeder. Prediction and confirmation of perpendicular magnetic anisotropy in Co/Ni multilayers. *Physical Review Letters*, 68(5):682, 1992.
- [58] A. Hubert and R. Schafer. *Magnetic domains*. Springer, 1998.
- [59] U. Gradmann. Magnetic surface anisotropies. *Journal of Magnetism and Magnetic Materials*, 54:733–736, 1986.
- [60] H. J. G. Draaisma, W. J. M. De Jonge, and F. J. A. Den Broeder. Magnetic interface anisotropy in Pd/Co and Pd/Fe multilayers. *Journal of Magnetism and Magnetic Materials*, 66(3):351–355, 1987.
- [61] F. J. A. Den Broeder, W. Hoving, and P. J. H. Bloemen. Magnetic anisotropy of multilayers. *Journal of Magnetism and Magnetic Materials*, 93:562–570, 1991.
- [62] P. F. Carcia. Perpendicular magnetic anisotropy in Pd/Co and Pt/Co thin-film layered structures. *Journal of Applied Physics*, 63(10):5066–5073, 1988.
- [63] N. Nakajima, T. Koide, T. Shidara, H. Miyauchi, H. Fukutani, A. Fujimori, K. Iio, T. Katayama, M. Nyvlt, and Y. Suzuki. Perpendicular magnetic anisotropy caused by interfacial hybridization via enhanced orbital moment in Co/Pt multilayers: magnetic circular x-ray dichroism study. *Physical Review Letters*, 81(23):5229, 1998.
- [64] S. S. P. Parkin and D. Mauri. Spin engineering: Direct determination of the Ruderman-Kittel-Kasuya-Yosida far-field range function in ruthenium. *Physical Review B*, 44(13):7131, 1991.

- [65] B. Dieny, J. P. Gavigan, and J. P. Rebouillat. Magnetisation processes, hysteresis and finite-size effects in model multilayer systems of cubic or uniaxial anisotropy with antiferromagnetic coupling between adjacent ferromagnetic layers. *Journal of Physics: Condensed Matter*, 2(1):159, 1990.
- [66] W. Folkerts. Calculated magnetic phase diagrams and magnetoresistance curves for an antiferromagnetically coupled multilayer system. *Journal of Magnetism and Magnetic Materials*, 94(3):302–310, 1991.
- [67] C. Zener. Interaction between the d shells in the transition metals. *Physical Review*, 81(3):440, 1951.
- [68] P. Hansen, C. Clausen, G. Much, M. Rosenkranz, and K. Witter. Magnetic and magneto-optical properties of rare-earth transition-metal alloys containing Gd, Tb, Fe, Co. *Journal of Applied Physics*, 66(2):756–767, 1989.
- [69] S. Uchiyama. Magnetic properties of rare earth-cobalt amorphous films. *Materials Chemistry and Physics*, 42(1):38–44, 1995.
- [70] C. Garg, S.-H. Yang, T. Phung, A. Pushp, and S. S. P. Parkin. Dramatic influence of curvature of nanowire on chiral domain wall velocity. *Science Advances*, 3(5):e1602804, 2017.
- [71] A. E. Thiaville, J. M. Garcia, and J. E. A. Miltat. Domain wall dynamics in nanowires. *Journal of Magnetism and Magnetic Materials*, 242:1061–1063, 2002.
- [72] K. S. Ryu, L. Thomas, S. H. Yang, and S. S. P. Parkin. Chiral spin torque at magnetic domain walls. *Nature Nanotechnology*, 8(7):527–533, 2013.
- [73] A. Hubert. *Theorie der Domänenwände in geordneten Medien*. Springer, 1974.
- [74] A. Thiaville, S. Rohart, É. Jué, V. Cros, and A. Fert. Dynamics of Dzyaloshinskii domain walls in ultrathin magnetic films. *Europhysics Letters*, 100(5):57002, 2012.
- [75] G. Chen, T. Ma, A. T. N’Diaye, H. Kwon, C. Won, Y. Wu, and A. K. Schmid. Tailoring the chirality of magnetic domain walls by interface engineering. *Nature Communications*, 4(2671), 2013.
- [76] I. Dzyaloshinsky. A thermodynamic theory of “weak” ferromagnetism of antiferromagnetics. *Journal of Physics and Chemistry of Solids*, 4(4):241–255, 1958.
- [77] T. Moriya. Anisotropic superexchange interaction and weak ferromagnetism. *Physical Review*, 120(1):91, 1960.
- [78] F. Keffer. Moriya interaction and the problem of the spin arrangements in β MnS. *Physical Review*, 126(3):896, 1962.

- [79] S.-W. Cheong and M. Mostovoy. Multiferroics: a magnetic twist for ferroelectricity. *Nature Materials*, 6(1):13–20, 2007.
- [80] A. N. Bogdanov and U. K. Rößler. Chiral symmetry breaking in magnetic thin films and multilayers. *Physical Review Letters*, 87(3):037203, 2001.
- [81] M. Heide, G. Bihlmayer, and S. Blügel. Dzyaloshinskii-Moriya interaction accounting for the orientation of magnetic domains in ultrathin films: Fe/W (110). *Physical Review B*, 78(14):140403, 2008.
- [82] J. M. Luttinger and C. Kittel. A note on the quantum theory of ferromagnetic resonance. *Helvetica Physica Acta*, 21(6):480–489, 1948.
- [83] J. M. Richardson. Quantum theory of ferromagnetic resonance. *Physical Review*, 75:1630–1631, 1949.
- [84] D. Polder. VIII. On the theory of ferromagnetic resonance. *The London, Edinburgh, and Dublin Philosophical Magazine and Journal of Science*, 40(300):99–115, 1949.
- [85] J. H. Van Vleck. Concerning the theory of ferromagnetic resonance absorption. *Physical Review*, 78(3):266, 1950.
- [86] L. D. Landau and E. M. Lifshitz. On the theory of the dispersion of magnetic permeability in ferromagnetic bodies. *Physikalische Zeitschrift der Sowjetunion*, 8:153–169, 1935.
- [87] D.-H. Kim, T. Okuno, S. K. Kim, S.-H. Oh, T. Nishimura, Y. Hirata, Y. Futakawa, H. Yoshikawa, A. Tsukamoto, Y. Tserkovnyak, Y. Shiota, T. Moriyama, K.-J. Kim, K.-J. Lee, and T. Ono. Low magnetic damping of ferrimagnetic GdFeCo alloys. *Physical Review Letters*, 122(12):127203, 2019.
- [88] J. L. Lagrange. *Mécanique analytique*. Mallet-Bachelier, 1853.
- [89] H. Goldstein, C. Poole, and J. Safko. *Classical mechanics*. Addison-Wesley, Reading, MA, 1980.
- [90] T. L. Gilbert. A phenomenological theory of damping in ferromagnetic materials. *IEEE Transactions on Magnetics*, 40(6):3443–3449, 2004.
- [91] D. H. Menzel. *Fundamental formulas of physics*, volume 1. Courier Corporation, 1960.
- [92] O. Boulle, S. Rohart, L. D. Buda-Prejbeanu, E. Jue, I. M. Miron, S. Pizzini, J. Vogel, G. Gaudin, and A. Thiaville. Domain wall tilting in the presence of the Dzyaloshinskii-Moriya interaction in out-of-plane magnetized magnetic nanotracks. *Physical Review Letters*, 111(21):217203, 2013.
- [93] A. P. Malozemoff and J. C. Slonczewski. *Magnetic domain walls in bubble materials*. Academic Press, 1979.

Bibliography

- [94] N. L. Schryer and L. R. Walker. The motion of 180 domain walls in uniform dc magnetic fields. *Journal of Applied Physics*, 45(12):5406–5421, 1974.
- [95] J. C. Slonczewski. Current-driven excitation of magnetic multilayers. *Journal of Magnetism and Magnetic Materials*, 159(1-2):L1–L7, 1996.
- [96] D. C. Ralph and M. D. Stiles. Spin transfer torques. *Journal of Magnetism and Magnetic Materials*, 320(7):1190 – 1216, 2008.
- [97] A. Manchon and S. Zhang. Theory of nonequilibrium intrinsic spin torque in a single nanomagnet. *Physical Review B*, 78(21):212405, 2008.
- [98] A. Manchon and S. Zhang. Theory of spin torque due to spin-orbit coupling. *Physical Review B*, 79(9):094422, 2009.
- [99] J. E. Hirsch. Spin Hall effect. *Physical Review Letters*, 83(9):1834, 1999.
- [100] S. Onoda, N. Sugimoto, and N. Nagaosa. Intrinsic versus extrinsic anomalous Hall effect in ferromagnets. *Physical Review Letters*, 97(12):126602, 2006.
- [101] D. Xiao, M.-C. Chang, and Q. Niu. Berry phase effects on electronic properties. *Reviews of Modern Physics*, 82(3):1959, 2010.
- [102] J. Stöhr and H. C. Siegmann. *Magnetism: From fundamentals to nanoscale dynamics*, volume 152. Springer, 2007.
- [103] L. Liu, O. J. Lee, T. J. Gudmundsen, D. C. Ralph, and R. A. Buhrman. Current-induced switching of perpendicularly magnetized magnetic layers using spin torque from the spin Hall effect. *Physical Review Letters*, 109(9):096602, 2012.
- [104] T. Tanaka, H. Kontani, M. Naito, T. Naito, D. S. Hirashima, K. Yamada, and J. Inoue. Intrinsic spin Hall effect and orbital Hall effect in 4d and 5d transition metals. *Physical Review B*, 77(16):165117, 2008.
- [105] L. Liu, C.-F. Pai, Y. Li, H. W. Tseng, D. C. Ralph, and R. A. Buhrman. Spin-torque switching with the giant spin Hall effect of tantalum. *Science*, 336(6081):555–558, 2012.
- [106] M.-H. Liu, S.-H. Chen, and C.-. Chang. Current-induced spin polarization in spin-orbit-coupled electron systems. *Physical Review B*, 78(16):165316, 2008.
- [107] S.-M. Seo, K.-W. Kim, J. Ryu, H.-W. Lee, and K.-J. Lee. Current-induced motion of a transverse magnetic domain wall in the presence of spin Hall effect. *Applied Physics Letters*, 101(2):022405, 2012.
- [108] X. Jiang, L. Gao, J. Z. Sun, and S. S. P. Parkin. Temperature dependence of current-induced magnetization switching in spin valves with a ferrimagnetic CoGd free layer. *Physical Review Letters*, 97(21):217202, 2006.

- [109] B. Dieny. Giant magnetoresistance in spin-valve multilayers. *Journal of Magnetism and Magnetic Materials*, 136(3):335–359, 1994.
- [110] K. J. Kim, S. K. Kim, Y. Hirata, S. H. Oh, T. Tono, D. H. Kim, T. Okuno, W. S. Ham, S. Kim, G. Go, Y. Tserkovnyak, A. Tsukamoto, T. Moriyama, K. J. Lee, and T. Ono. Fast domain wall motion in the vicinity of the angular momentum compensation temperature of ferrimagnets. *Nature Materials*, 16:1187–1192, 2017.
- [111] S. G. Je, D. H. Kim, S. C. Yoo, B. C. Min, K. J. Lee, and S. B. Choe. Asymmetric magnetic domain-wall motion by the Dzyaloshinskii-Moriya interaction. *Physical Review B*, 88(21):214401, 2013.
- [112] W. Baltensperger and J. S. Helman. Dry friction in micromagnetics. *IEEE Transactions on Magnetics*, 27(6):4772–4774, 1991.
- [113] G. Consolo and E. Martinez. The effect of dry friction on domain wall dynamics: A micromagnetic study. *Journal of Applied Physics*, 111(7):07D312, 2012.
- [114] C.-F. Pai, Y. Ou, L. H. Vilela-Leão, D. C. Ralph, and R. A. Buhrman. Dependence of the efficiency of spin Hall torque on the transparency of Pt/ferromagnetic layer interfaces. *Physical Review B*, 92(6):064426, 2015.
- [115] E. Martinez, L. Lopez-Diaz, L. Torres, C. Tristan, and O. Alejos. Thermal effects in domain wall motion: Micromagnetic simulations and analytical model. *Physical Review B*, 75(17):174409, 2007.
- [116] L. Thomas, S.-H. Yang, K.-S. Ryu, B. Hughes, C. Rettner, D.-S. Wang, C.-H. Tsai, K.-H. Shen, and S. S. P. Parkin. Racetrack Memory: A high-performance, low-cost, non-volatile memory based on magnetic domain walls. In *2011 International Electron Devices Meeting*, pages 24.2.1–24.2.4. IEEE, 2011.
- [117] M. T. Johnson, P. J. H. Bloemen, F. J. A. Den Broeder, and J. J. De Vries. Magnetic anisotropy in metallic multilayers. *Reports on Progress in Physics*, 59(11):1409, 1996.
- [118] R. P. Hunt. Magneto-optic scattering from thin solid films. *Journal of Applied Physics*, 38(4):1652–1671, 1967.
- [119] O. Posth, C. Hassel, M. Spasova, G. Dumpich, J. Lindner, and S. Mangin. Influence of growth parameters on the perpendicular magnetic anisotropy of [Co/Ni] multilayers and its temperature dependence. *Journal of Applied Physics*, 106(2):023919, 2009.
- [120] J. Seib and M. Fähnle. Calculation of the Gilbert damping matrix at low scattering rates in Gd. *Physical Review B*, 82(6):064401, 2010.
- [121] R. Hasegawa. Static bubble-domain properties of amorphous Gd-Co films. *Journal of Applied Physics*, 45(7):3109–3112, 1974.

Bibliography

- [122] O. S. Lutes, J. O. Holmen, R. L. Kooyer, and O. S. Aadland. Inverted and biased loops in amorphous Gd-Co films. *IEEE Transactions on Magnetism*, 13(5):1615–1617, 1977.
- [123] J. Grollier, P. Boulenc, V. Cros, A. Hamzić, A. Vaures, A. Fert, and G. Faini. Switching a spin valve back and forth by current-induced domain wall motion. *Applied Physics Letters*, 83(3):509–511, 2003.
- [124] N. Vernier, D. A. Allwood, D. Atkinson, M. D. Cooke, and R. P. Cowburn. Domain wall propagation in magnetic nanowires by spin-polarized current injection. *Europhysics Letters*, 65(4):526, 2004.
- [125] M. Laufenberg, W. Buhner, D. Bedau, P. E. Melchy, M. Klaui, L. Vila, G. Faini, C. A. F. Vaz, J. A. C. Bland, and U. Rudiger. Temperature dependence of the spin torque effect in current-induced domain wall motion. *Physical Review Letters*, 97(4):046602, 2006.
- [126] A. Yamaguchi, S. Nasu, H. Tanigawa, T. Ono, K. Miyake, K. Mibu, and T. Shinjo. Effect of Joule heating in current-driven domain wall motion. *Applied Physics Letters*, 86(1):012511, 2005.
- [127] L. Thomas, M. Hayashi, X. Jiang, C. Rettner, and S. S. P. Parkin. Perturbation of spin-valve nanowire reference layers during domain wall motion induced by nanosecond-long current pulses. *Applied Physics Letters*, 92(11):112504, 2008.
- [128] G. Meier, M. Bolte, R. Eiselt, B. Krüger, D.-H. Kim, and P. Fischer. Direct imaging of stochastic domain-wall motion driven by nanosecond current pulses. *Physical Review Letters*, 98(18):187202, 2007.
- [129] C.-Y. You, I. M. Sung, and B.-K. Joe. Analytic expression for the temperature of the current-heated nanowire for the current-induced domain wall motion. *Applied Physics Letters*, 89(22):222513, 2006.
- [130] L. Thomas, M. Hayashi, X. Jiang, R. Moriya, C. Rettner, and S. S. P. Parkin. Oscillatory dependence of current-driven magnetic domain wall motion on current pulse length. *Nature*, 443(7108):197–200, 2006.
- [131] I. M. Miron, T. Moore, H. Szambolics, L. D. Buda-Prejbeanu, S. Auffret, B. Rodmacq, S. Pizzini, J. Vogel, M. Bonfim, A. Schuhl, and G. Gaudin. Fast current-induced domain-wall motion controlled by the Rashba effect. *Nature Materials*, 10(6):419–423, 2011.
- [132] G. Tatara and H. Kohno. Theory of current-driven domain wall motion: Spin transfer versus momentum transfer. *Physical Review Letters*, 92(8):086601, 2004.
- [133] A. Thiaville, Y. Nakatani, J. Miltat, and N. Vernier. Domain wall motion by spin-polarized current: A micromagnetic study. *Journal of Applied Physics*, 95(11):7049–7051, 2004.

- [134] S.-M. Seo, K.-J. Lee, W. Kim, and T.-D. Lee. Effect of shape anisotropy on threshold current density for current-induced domain wall motion. *Applied Physics Letters*, 90(25):252508, 2007.
- [135] S. Fukami, T. Suzuki, N. Ohshima, K. Nagahara, and N. Ishiwata. Intrinsic threshold current density of domain wall motion in nanostrips with perpendicular magnetic anisotropy for use in low-write-current MRAMs. *IEEE Transactions on Magnetics*, 44(11):2539–2542, 2008.
- [136] C. Chappert, D. Renard, P. Beauvillain, J. P. Renard, and J. Seiden. Ferromagnetism of very thin films of nickel and cobalt. *Journal of Magnetism and Magnetic Materials*, 54:795–796, 1986.
- [137] W. F. Brown Jr. Thermal fluctuations of a single-domain particle. *Physical Review*, 130(5):1677, 1963.
- [138] J. L. García-Palacios and F. J. Lázaro. Langevin-dynamics study of the dynamical properties of small magnetic particles. *Physical Review B*, 58(22):14937, 1998.
- [139] R. Kubo. The fluctuation-dissipation theorem. *Reports on Progress in Physics*, 29(1):255, 1966.
- [140] D. G. Cahill, W. K. Ford, K. E. Goodson, G. D. Mahan, A. Majumdar, H. J. Maris, R. Merlin, and S. R. Phillpot. Nanoscale thermal transport. *Journal of Applied Physics*, 93(2):793–818, 2003.

Appendix

A. Mathematical supplement

A.1. Properties of domain wall profile

The DW profile including the DW tilt angle χ is given by [92]

$$\theta = 2 \tan^{-1} \left[\exp \left(\pm \frac{x \cos \chi + y \sin \chi - q \cos \chi}{\Delta} \right) \right]. \quad (\text{A.1})$$

This DW profile can be used for a quasi 2D model. Note that in contrast to ϕ , χ is defined as the angle deviating from the \hat{y} axis. For the 1D model, the tilt angle can be set to $\chi = 0$. An often needed form is $\sin \theta$ and $\cos \theta$ which are given by

$$\begin{aligned} \sin \theta &= \operatorname{sech} \left(\pm \frac{x \cos \chi + y \sin \chi - q \cos \chi}{\Delta} \right) \\ \cos \theta &= \mp \tanh \left(\pm \frac{x \cos \chi + y \sin \chi - q \cos \chi}{\Delta} \right). \end{aligned}$$

Furthermore, the derivatives of θ in respect to x , y , q , and time t are needed:

$$\begin{aligned} \frac{d\theta}{dx} &= \pm \frac{1}{\Delta} \sin \theta \cos \chi \\ \frac{d\theta}{dy} &= \pm \frac{1}{\Delta} \sin \theta \sin \chi \\ \frac{d\theta}{dq} &= \mp \frac{1}{\Delta} \sin \theta \cos \chi \\ \frac{d\theta}{dt} &= \pm \frac{1}{\Delta} \sin \theta (-\dot{q} \cos \chi - x \dot{\chi} \sin \chi + y \dot{\chi} \cos \chi + q \dot{\chi} \sin \chi). \end{aligned}$$

To solve the integrals of the Lagrangian function, following solutions of the integrals were used:

$$f(x) \rightarrow \int_{-\infty}^{+\infty} f(x) dx$$

$$\begin{aligned} \cos \theta &\rightarrow \pm 2 (y \tan \chi - q) \\ \cos^2 \theta &\rightarrow -\frac{2 \Delta}{\cos \chi} \\ \sin \theta &\rightarrow \frac{\pi \Delta}{\cos \chi} \\ \cos \theta \sin \theta &\rightarrow 0 \\ x \sin \theta &\rightarrow \frac{\pi \Delta}{\cos \chi} (q - y \tan \chi) \\ \sin^2 \theta &\rightarrow \frac{2 \Delta}{\cos \chi} \\ \cos \theta \sin^2 \theta &\rightarrow 0 \\ \cos^2 \theta \sin^2 \theta &\rightarrow \frac{2 \Delta}{3 \cos \chi} \\ x \sin^2 \theta &\rightarrow \frac{2 \Delta}{\cos \chi} (q - y \tan \chi) \\ \sin^4 \theta &\rightarrow \frac{4 \Delta}{3 \cos \chi} \end{aligned}$$

A.2. Effective quantities approach

For the case of very strong coupling, the usage of effective quantities simplifies the equations of motion as discussed by SIDDIQUI in [23]. The coupling can be considered small if

$$\delta\phi \stackrel{\text{def}}{=} \phi^L - \phi^U - \pi$$

is very small as a large (negative) J_{ex} leads to $\phi^U \approx \phi^L + \pi$. Equations (2.38a), (2.38b) and (2.38c) can then be rewritten using

$$A_{\text{net}} = A^L - A^U$$

and

$$\alpha_{\text{eff}} \stackrel{\text{def}}{=} \frac{\alpha^L A^L + \alpha^U A^U}{A_{\text{net}}}.$$

The equation of motion are then

$$\frac{\alpha_{\text{eff}} A_{\text{net}}}{\Delta} \dot{q} = J_{\text{SH}} \cos \phi^U + A_{\text{net}} \dot{\phi}^U \quad (\text{A.2a})$$

$$\mp \frac{A^L}{\Delta} \dot{q} = -J_{\text{DMI}}^L \sin \phi^U + J_{\text{ex}} \delta\phi \pm \alpha^L A^L \dot{\phi}^U \quad (\text{A.2b})$$

$$\mp \frac{A^U}{\Delta} \dot{q} = J_{\text{DMI}}^U \sin \phi^U + J_{\text{ex}} \delta\phi \pm \alpha^U A^U \dot{\phi}^U. \quad (\text{A.2c})$$

By solving equation (A.2b) or (A.2c) in respect to $J_{\text{ex}} \delta\phi$ and inserting into the other gives

$$\dot{\phi}^{\text{L}} = \mp \frac{1}{\alpha^{\text{L}} A^{\text{L}} + \alpha^{\text{U}} A^{\text{U}}} \left(\pm A_{\text{net}} \frac{\dot{q}}{\Delta} - J_{\text{DMI}} \sin \phi^{\text{L}} \right).$$

This can be inserted into equation (A.2a) which finally results in

$$\dot{q} = \frac{\Delta}{A_{\text{net}} (\alpha_{\text{eff}}^2 + 1)} \left(\alpha_{\text{eff}} J_{\text{SH}} \cos \phi^{\text{U}} \pm J_{\text{DMI}} \sin \phi^{\text{L}} \right). \quad (\text{A.3})$$

This is the same result as in [23] if equations (1) and (2) in the SI of this paper are solved by inserting $\dot{\phi}$ into each other taking the different definition of $\phi = \varphi + \frac{\pi}{2}$ into account and just looking at an $\downarrow\uparrow$ DW which results in

$$\frac{A_{\text{net}} (\alpha_{\text{eff}}^2 + 1)}{\Delta} \dot{q} = \alpha_{\text{eff}} J_{\text{SH}} \sin \varphi - J_{\text{DMI}} \cos \varphi.$$

Note that the approximation of very large inter-layer exchange coupling is not valid for SAF structures. Moreover, equation (A.3) shadows the underlying principle of why the DWs in anti-ferromagnetically coupled systems move so fast. This mechanism is discussed in the section 2.3.6.

A.3. Tilting of DW in ferrimagnetic bi-layer

In the context of the present study, DW velocity in a ferrimagnetic Co/Gd bi-layer was also measured in a sample with curved wires (cf. [70] for details of this measurement). With decreasing temperature, the velocity $v^{\uparrow\downarrow}(T)$ of a $\uparrow\downarrow$ DW increases and the velocity $v^{\downarrow\uparrow}(T)$ of a $\downarrow\uparrow$ decreases. At a certain temperature $T_{v^{\uparrow\downarrow} = v^{\downarrow\uparrow}}(j)$ DW velocity of both DWs is the same. The results are shown in Figure C.14. Like $T_{\xi=0}(j)$, there is a dependence on j which can be attributed to JOULE heating. However, $T_{v^{\uparrow\downarrow} = v^{\downarrow\uparrow}}(0)$ and $T_{\xi=0}(0)$ are distinct. These findings may be linked to a similar relation as equation (2.50) but for a dependence of curvature and DW tilting.

For ferromagnetic thin films, the DW tilt was described by a tilt angle χ [92]. In order to extend this model, the effective quantity approach is used (cf. [23, 24]) which is discussed in section A.2. The underlying assumption for this approach, is a large inter-layer exchange coupling. The choice of ϕ to be ϕ^{L} or ϕ^{U} is dependent of the DW configuration as discussed in section A.2.

The LAGRANGIAN function L including the DW tilt is then given by

$$L = \int_{-\infty}^{+\infty} \int_{-w/2}^{+w/2} A_{\text{ex}} \left[\left(\frac{d\theta}{dx} \right)^2 + \left(\frac{d\theta}{dy} \right)^2 \right] + K_{\text{eff}} \sin^2 \theta \pm \frac{2}{\pi} J_{\text{DMI}} \sin \theta \cos(\phi - \chi) \\ - m_{\text{net}} (H_z \cos \theta + H_x \sin \theta \cos \phi + H_y \sin \theta \sin \phi) + A_{\text{net}} \phi \dot{\theta} \sin \theta \, dy \, dx$$

where the last term is the kinetic energy T of the DW and all terms before represent E . Here, J_{DMI} denotes the total DMI energy in the bi-layer $J_{\text{DMI}} = \frac{\pi}{2} \frac{D^{\text{L}} + D^{\text{U}}}{\Delta}$. Note that the demagnetization

energy of DW has been neglected here. Integration using the DW profile (A.1) yields

$$L = w \left[2 \frac{1}{\Delta} \frac{1}{\cos \chi} A_{\text{ex}} + 2 \Delta \frac{1}{\cos \chi} K_{\text{eff}} \pm \frac{\cos(\phi - \chi)}{\cos \chi} 2 J_{\text{DMI}} - m_{\text{net}} \left(\pm 2 q H_z + \pi \Delta \frac{1}{\cos \chi} H_x \cos \phi + \pi \Delta \frac{1}{\cos \chi} H_y \sin \phi \right) + 2 A_{\text{net}} \phi \dot{\phi} \right].$$

Similarly the dissipation function F is given by

$$F = \int_{-\infty}^{+\infty} \int_{-w/2}^{+w/2} \alpha_{\text{eff}} \frac{1}{2} A_{\text{net}} \left(\sin^2 \theta \dot{\phi}^2 + \dot{\theta}^2 \right) - J_{\text{SH}} \left(-\dot{\theta} \cos \phi + \dot{\theta} \sin \theta \cos \theta \sin \phi \right) dy dx$$

where dry friction and STT are neglected and $J_{\text{SH}} = \frac{\pi}{2} \frac{\hbar(\theta_{\text{SH}}^{\text{L}} + \theta_{\text{SH}}^{\text{U}})j}{2e}$. Plugging in the DW profile (A.1) and integrating yields

$$F = w \left[\frac{\alpha_{\text{eff}} A_{\text{net}}}{\Delta} \dot{\phi} \cos \chi + \frac{\alpha_{\text{eff}} A_{\text{net}}}{12 \Delta} (\pi^2 \Delta^2 \sin^2 \chi + w^2) \dot{\chi}^2 \sec^3 \chi \mp 2 J_{\text{SH}} \dot{\phi} \cos \phi + \alpha_{\text{eff}} A_{\text{net}} \Delta \frac{1}{\cos \chi} \dot{\phi}^2 \right].$$

Plugging L and F into the RAYLEIGH-LAGRANGE equation (2.22) results in the three equations of motion for a tilted DW in a ferrimagnetic bi-layer with strong inter-layer exchange coupling:

$$(\alpha^{\text{L}} A^{\text{L}} + \alpha^{\text{U}} A^{\text{U}}) \frac{\dot{q}}{\Delta} \cos \chi \pm A_{\text{net}} \dot{\phi} = \pm J'_{\text{H}_z} \pm J_{\text{SH}} \cos \phi$$

$$A_{\text{net}} \frac{\dot{q}}{\Delta} \cos \chi \mp (\alpha^{\text{L}} A^{\text{L}} + \alpha^{\text{U}} A^{\text{U}}) \dot{\phi} = -J_{\text{DMI}} \sin(\phi - \chi) \pm (J'_{\text{H}_x} \sin \phi - J'_{\text{H}_y} \cos \phi) \quad (\text{A.4a})$$

$$\dot{\chi} \frac{(\alpha^{\text{L}} A^{\text{L}} + \alpha^{\text{U}} A^{\text{U}}) \pi^2}{12} \left(\tan^2 \chi + \frac{w^2}{\pi^2 \Delta^2} \sec^2 \chi \right) = \pm J_{\text{DMI}} \sin(\phi - \chi) - \tan \chi \left[\frac{\sqrt{4 A_{\text{ex}} K_{\text{eff}}}}{\Delta} \pm J_{\text{DMI}} \cos(\phi - \chi) - J'_{\text{H}_x} \cos \phi + J'_{\text{H}_y} \sin \phi \right] \quad (\text{A.4b})$$

Here, in J'_{H_x} , J'_{H_y} , and J'_{H_z} the ' symbol shall denote that instead of m , m_{net} is used such that $J'_{\text{H}_z} = m_{\text{net}} H_z$, $J'_{\text{H}_x} = \frac{\pi}{2} m_{\text{net}} H_x$, and $J'_{\text{H}_y} = \frac{\pi}{2} m_{\text{net}} H_y$.

At angular momentum compensation, $A_{\text{net}} = 0$, in steady state motion, $\dot{\phi} = \dot{\chi} = 0$, with $H_x = H_y = 0$ it can be found from equation (A.4a) that $\sin(\phi - \chi) \big|_{A_{\text{net}}=0} = 0$. Hence, from equation (A.4b) it follows that $\tan(\chi) \big|_{A_{\text{net}}=0} = 0$ which is fulfilled for

$$\chi \big|_{A_{\text{net}}=0} = 0.$$

Consequently, at angular momentum compensation the DW does not tilt.

Furthermore, it shall be noted that the time scale in which the DW relaxes to a certain angle is dependent on A^{L} and A^{U} . Using the equations for the relaxation times of ϕ and χ derived in

[92] and plugging in the effective quantities yields,

$$t_\phi \approx \frac{A_{\text{net}}^2 + (\alpha^L A^L + \alpha^U A^U)^2}{(\alpha^L A^L + \alpha^U A^U) J_{\text{DMI}}}$$

for the settlement time of $\dot{\phi}$ and

$$t_\chi \approx \frac{(\alpha^L A^L + \alpha^U A^U) w^2}{6 \sigma_{\text{DW}} \Delta}$$

for the settlement time of $\dot{\chi}$. While t_ϕ is approximately in the picosecond time regime, t_χ can reach the nanosecond time regime for micrometer wide wires.

B. Modeling of Joule heating

This chapter is part of the Supplementary Information of [21]. These COMSOL simulations were performed by Dr. FASIL KIDANE DEJENE.

B.1. Numerical modeling of Joule heating in racetrack

In this section, the finite element model used to estimate the overall heating in the device is described. Additionally, a series of simulation data that explains the experimentally observed heating effects in the current-induced domain wall motion of magnetic Co/Gd bi-layers is present. The Joule heating module of the commercial software COMSOL MULTIPHYSICS is used and solved for the temperature increase in the device. As shown in Figure B.1a, a rectangular voltage pulse of amplitude V_0 and pulse-duration of t_p is applied at one leg of the racetrack while keeping the other end at a ground potential. The resulting current density j causes Joule-heating which is mostly concentrated at the narrower section of the device. The aim is to find the time t evolution of the temperature T by numerically solving the transient heat-diffusion equation:

$$\rho C_p \frac{\partial T}{\partial t} = \kappa \nabla^2 T + Q_e,$$

where ρ is the density, C_p is the specific heat capacity, κ is the thermal conductivity, $Q_e = j^2/\sigma$ is the heat generated by Joule-heating which is proportional to the current density j . As the measurements are mostly performed below room temperature and in a vacuum, convective and radiative heat losses are not considered as they contribute only to a maximum of 5 % temperature (confirmed via an independent control simulation) change towards the the heat diffusion processes. It is straightforward to incorporate such losses in the model by setting outward heat flux boundary proportional to the device temperature rise and heat-transfer coefficient of the metal-vacuum interface.

Material properties

This three-dimensional heat diffusion equation is solved (in the time-domain) for a device-geometry shown in Figure B.1a with carefully chosen input parameters, such as the electrical conductivity σ , thermal conductivity κ , specific heat capacity C_p and density ρ . The temperature of the device is initially set to the base temperature of the cryostat and the δT is calculated in the time interval $t = [0, 2 t_p]$, where t_p is the pulse duration, with a time-step of 0.2 ns. How fast the temperature rises depends on the initial temperature of the sample and thermal diffusivity $\alpha = \kappa/(\rho C_p)$ of the materials.

The device modelled here is comprised of a stack sequence of Si / 250 SiO_x / 100 AlO_x / 20 TaN / 30 Pt / 5 Co / 18 Gd / 50 TaN (All thicknesses in Å). The active part of the racetrack (30 Pt / 5 Co / 18 Gd / 50 TaN) was modeled as a single metallic film whose electrical conductivity σ is obtained from a separate measurement of the racetrack resistance as a function of temperature

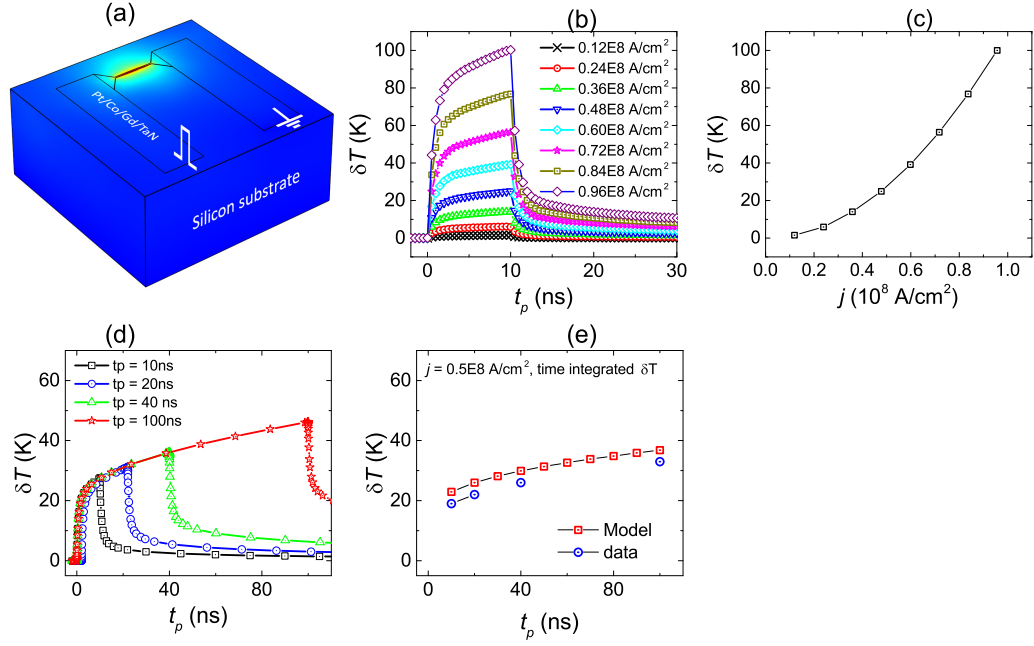


Figure B.1.: COMSOL simulations of Joule heating in nanowire. Data also used in [21]. (a) Three-dimensional temperature profile of the racetrack on a Silicon substrate (Here red (blue) is hot(cold)). A rectangular voltage pulse V_0 with a variable pulse duration t_p is applied to the left leg of the racetrack while the right-leg is kept at the ground potential. Most of the power is dissipated in the narrower-section which shows an elevated temperature. (b) The temperature $\delta T = T - T_{ref}$, where T_{ref} is the surrounding temperature rise as a function of time (in nanoseconds) different current densities j with a pulse duration t_p of 10 ns. (c) The maximum temperature rise as a function of the current density for the data in (b). (d) Pulse duration dependence of the temperature rise and (e) the time-averaged increase for the data in (d).

(c.f. Figure C.11). Because heat transport in metals is largely dominated by the electronic contribution (but not by the phonons), it suffices to estimate the thermal conductivity κ of the racetrack using the well-known Wiedemann-Franz relation as $\kappa = L_0 \sigma T_0$, where $L_0 = 2.44 \times 10^{-8} \text{ V}^2 \text{ K}^{-2}$ is the Lorenz number and T_0 is the reference temperature. The specific heat capacity C_p and densities ρ were set equal to the average of the layers in the racetrack. Because the thermal properties of SiO_2 , TaN and AlO_x are very close to each other, the remaining component of the stack (250 SiO_x / 100 AlO_x / 20 TaN) is modeled as a 370 Å thick SiO_2 substrate with an effective thermal conductivity of 1.5W/(mK) [140]. Heat diffusion to the bottom of the Si substrate is also included by setting the bottom surface of the 500 μm thick Si wafer to the base temperature of the cryostat.

Results

Figure B.1a shows a representative temperature profile of a device obtained from the three-dimensional model. Figure B.1b shows the average volume temperature of the narrow section of the device as a function of time for a 10 ns voltage pulse. Different curves are for various values of j at $T = 210\text{K}$. As shown in Figure B.1c, the temperature-rise δT is quadratic in j where the maximum temperature for each curve in Figure B.1b is plotted as a function of j .

For a similar temperature and j , the pulse duration t_p dependence of δT is shown in Figure B.1d. In the experiment, the estimated temperature rise is obtained after some time-delay and thus does not represent the maximum heating in the device. To make a good comparison with our model, the time-averaged δT of the racetrack microwire is present as shown in red open square symbols, which agree well within 10% of the measurements (shown in blue circle). Given that most of the input-material parameters are obtained from the literature and only the electrical conductivity of the racetrack was measured, an agreement of the simulation data to within 10% of the measured δT indicates that the modeling procedure which was followed here captures the main heat diffusion/transport processes occurring in the current-driven motion of domain walls in racetracks.

B.2. DW dynamics for time-varying moments

In the following section the effect of the time-dependent heating during the current pulses of length t_p on the DW dynamics is considered. From equation (2.38a) with $H_z = 0$ and $\beta_i = 0$ for simplicity it can be found:

$$\dot{q} = \frac{\Delta}{\alpha^L A^L + \alpha^U A^U} \left[\mp A^L \dot{\phi}^L \pm A^U \dot{\phi}^U \mp (J_{\text{SH}}^L \cos \phi^L - J_{\text{SH}}^U \cos \phi^U) \right]$$

The travel distance δq of the DW t_p can be calculated by

$$\delta q = \int_0^{t_p} \dot{q} dt .$$

With

$$\begin{aligned} f(M^L, M^U) &= \frac{\mp J_{\text{SH}}^L}{\frac{M^L t^L \alpha^L}{\gamma^L \Delta^L} + \frac{M^U t^U \alpha^U}{\gamma^U \Delta^U}} \\ g(M^L, M^U) &= \frac{\pm J_{\text{SH}}^U}{\frac{M^L t^L \alpha^L}{\gamma^L \Delta^L} + \frac{M^U t^U \alpha^U}{\gamma^U \Delta^U}} \\ h(M^L, M^U) &= \frac{\frac{M^L t^L}{\gamma^L}}{\frac{M^L t^L \alpha^L}{\gamma^L \Delta^L} + \frac{M^U t^U \alpha^U}{\gamma^U \Delta^U}} \\ k(M^L, M^U) &= \frac{\frac{M^U t^U}{\gamma^U}}{\frac{M^L t^L \alpha^L}{\gamma^L \Delta^L} + \frac{M^U t^U \alpha^U}{\gamma^U \Delta^U}} \end{aligned}$$

it can be rewritten to

$$\delta q = \int_0^{t_p} [f(M^L, M^U) \cos \phi^L + g(M^L, M^U) \cos \phi^U + h(M^L, M^U) \dot{\phi}^L + k(M^L, M^U) \dot{\phi}^U] dt .$$

If $m^i(T)$ was constant over time, the traveled distance can be calculated by

$$\delta q = \left[f(M^L, M^U) \int_0^{t_p} \cos \phi^L dt + g(M^L, M^U) \int_0^{t_p} \cos \phi^U dt + h(M^L, M^U) \int_0^{t_p} \dot{\phi}^L dt + k(M^L, M^U) \int_0^{t_p} \dot{\phi}^U dt \right] . \quad (\text{B.1})$$

In contrast, it can be considered that $m^i(T)$ varies with time. It is assumed that ϕ^i and $\dot{\phi}^i$ vary very slowly during most of time during t_p . Indeed, due to the vary large exchange coupling in Co and Gd, the relaxation times of ϕ^i and $\dot{\phi}^i$ are so fast that this condition is fulfilled (c.f. [9]). In this case δq can be approximated by

$$\delta q \approx \left[\int_0^{t_p} f(M^L, M^U) dt \right] \left[\int_0^{t_p} \cos \phi^L dt \right] + \left[\int_0^{t_p} g(M^L, M^U) dt \right] \left[\int_0^{t_p} \cos \phi^U dt \right] + \left[\int_0^{t_p} h(M^L, M^U) dt \right] \left[\int_0^{t_p} \dot{\phi}^L dt \right] + \left[\int_0^{t_p} k(M^L, M^U) dt \right] \left[\int_0^{t_p} \dot{\phi}^U dt \right]$$

In order to calculate the velocity v for this pulse, δq has to be divided by t_p . Thus,

$$v = \bar{f}(M^L, M^U) \left[\int_0^{t_p} \cos \phi^L dt \right] + \bar{g}(M^L, M^U) \left[\int_0^{t_p} \cos \phi^U dt \right] + \bar{h}(M^L, M^U) \left[\int_0^{t_p} \dot{\phi}^L dt \right] + \bar{k}(M^L, M^U) \left[\int_0^{t_p} \dot{\phi}^U dt \right] \quad (\text{B.2})$$

with $\bar{X}(M^L, M^U) = \frac{1}{t_p} \int_0^{t_p} X(M^L, M^U) dt$. When comparing equations (B.1) and (B.2), it can be seen that the DW displacement over time t_p almost equals in the case of time averaged moments and in case the moments change with time. Therefore, it is valid to calculate the DW velocity at an average temperature and compare these results with the measured DW velocity at the averaged temperature presented in Figure 4.11 and Figure 4.12.

C. Supplementary figures

C.1. Micromagnetic simulations

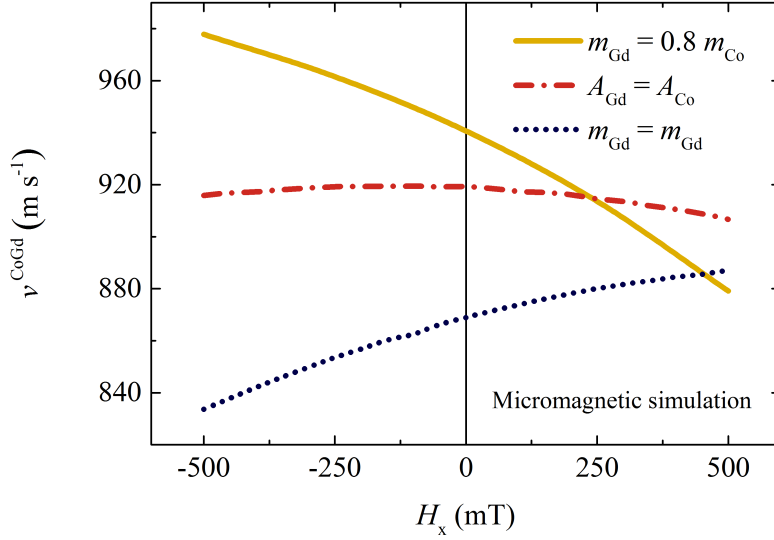


Figure C.1.: Micromagnetic simulations by LLG Simulator of velocity dependence on H_x in ferrimagnetic bi-layer. Used typical parameters for a Co/Gd bi-layer (note that here, these do not exactly correspond to values used in analytical model). Least influence of H_x on v at angular momentum compensation. At magnetic moment compensation v dependence on H_x can be found. Current density of $1.5 \times 10^8 \text{ A cm}^{-2}$ used (note that the behavior is independent of j).

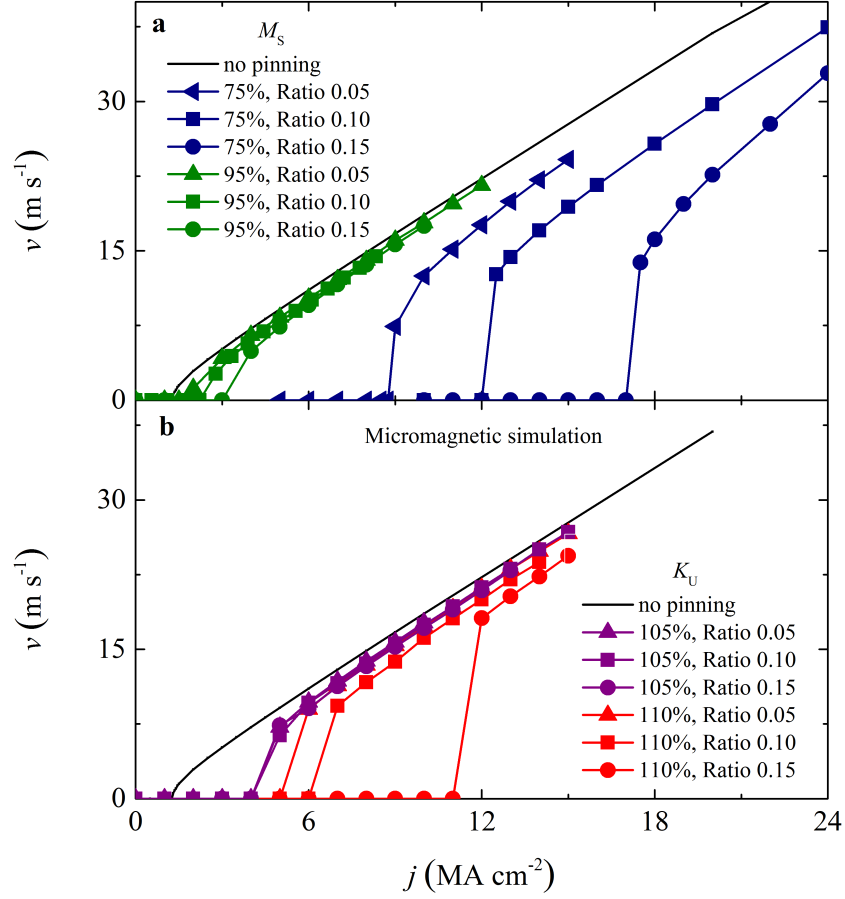


Figure C.2.: Micromagnetic simulations by LLG Simulator modeling magnetic pinning defects in ferromagnetic layer. Parameters of a Pt/Co/Ni/Co sample used. Pinning in sample by introducing randomly distributed pinning defects by **a** variation of magnetization M_s and **b** variation of uniaxial anisotropy K_u . In **a** defects are locally decreased magnetization by 25 % or 5 % compared to original parameter for M_s . In **b** defects are locally increased uniaxial anisotropy by 5 % or 10 % compared to original parameter for K_u . Ratio of pinning defects to original parameters in the sample varied from 5 % to 15 %.

C.2. Ferromagnetic Co/Ni/Co structure

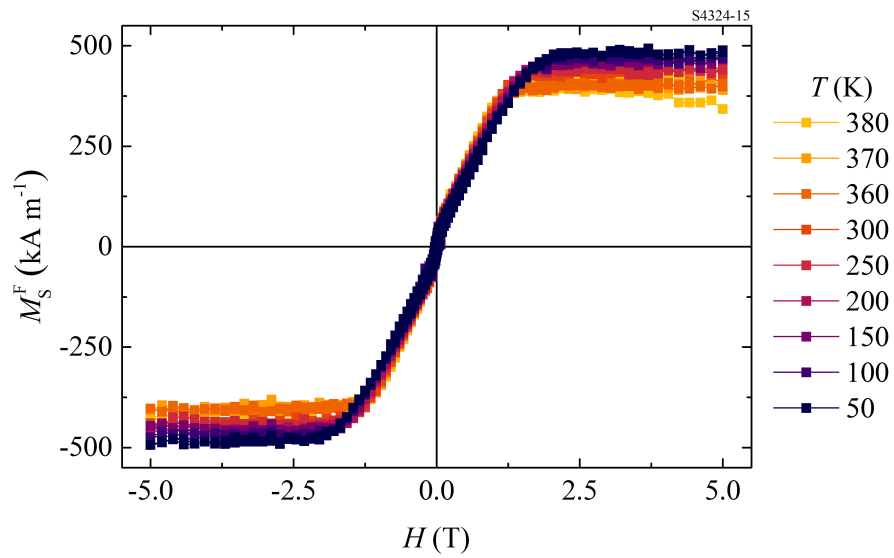


Figure C.3.: In-plane hysteresis loops of ferromagnetic Co/Ni/Co sample measured by SQUID. Sample volume $10.3 \times 10^{-9} \text{ cm}^3$.

C.3. SAF structure

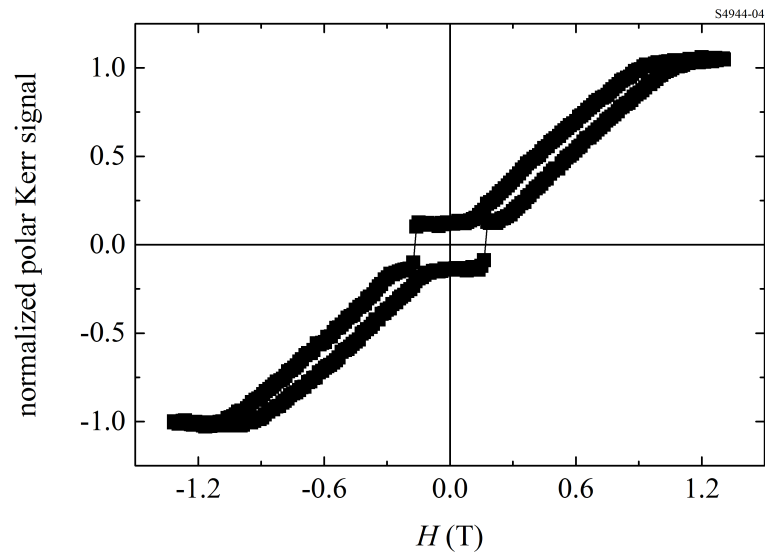


Figure C.4.: Polar Kerr data of SAF structure at room temperature. Data was linearly fitted at plateau regions (> 1 T). Slope of fit was subtracted to subtract background. Signal has then been normalized to plateau region.

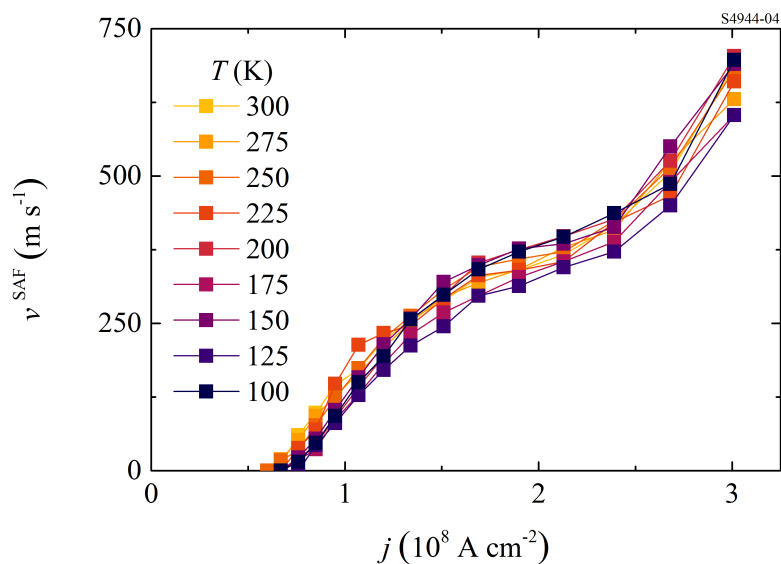


Figure C.5.: Domain wall velocity in SAF structure as a function of current density at various cryostat temperatures. Constant resistance of 3.08 k Ω is assumed.

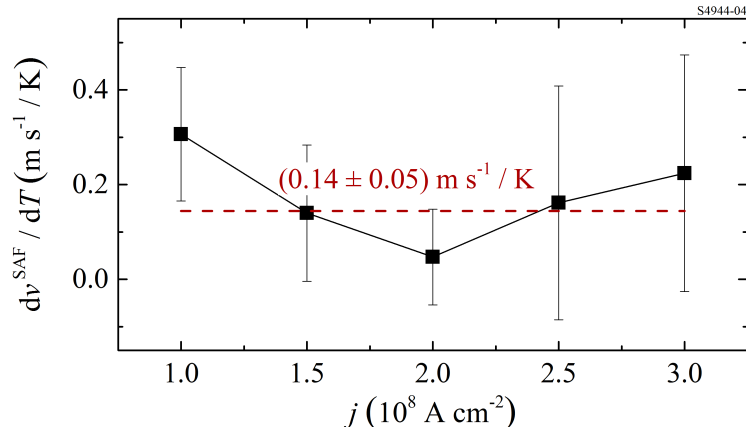


Figure C.6.: Increase of domain wall velocity with temperature as a function of current density in SAF structure. Data of Figure 4.6 is linearly fitted for current densities around $1.0 \times 10^8 \text{ A cm}^{-2}$ (averaging $0.95 \times 10^8 \text{ A cm}^{-2}$ and $1.07 \times 10^8 \text{ A cm}^{-2}$), $1.5 \times 10^8 \text{ A cm}^{-2}$, $2.0 \times 10^8 \text{ A cm}^{-2}$ (averaging $1.90 \times 10^8 \text{ A cm}^{-2}$ and $2.13 \times 10^8 \text{ A cm}^{-2}$), $2.5 \times 10^8 \text{ A cm}^{-2}$ (averaging $2.39 \times 10^8 \text{ A cm}^{-2}$ and $2.68 \times 10^8 \text{ A cm}^{-2}$), and $3.0 \times 10^8 \text{ A cm}^{-2}$.

C.4. Ferrimagnetic Co/Gd bi-layer

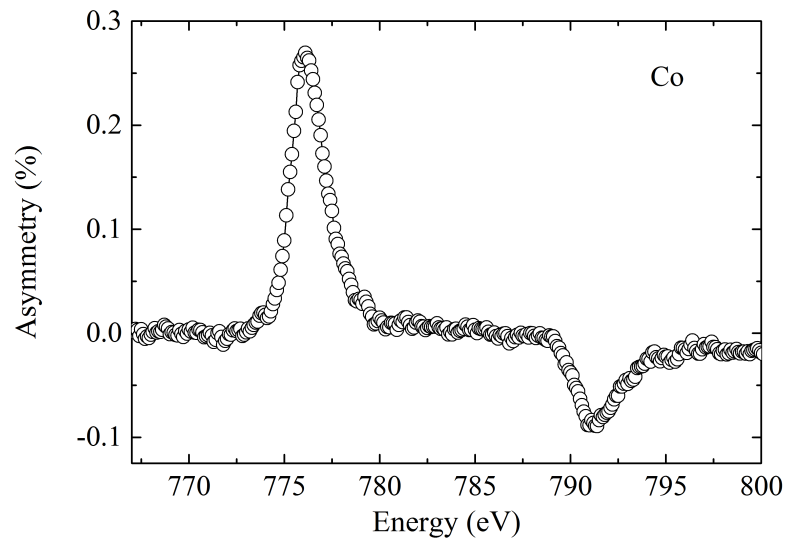


Figure C.7.: Asymmetry in XMCD spectrum of Co at L_2 and L_3 edge. Asymmetry caused by difference between right and left circular polarized light as function of X-ray energy. Measurement temperature $T = 222.5$ K.

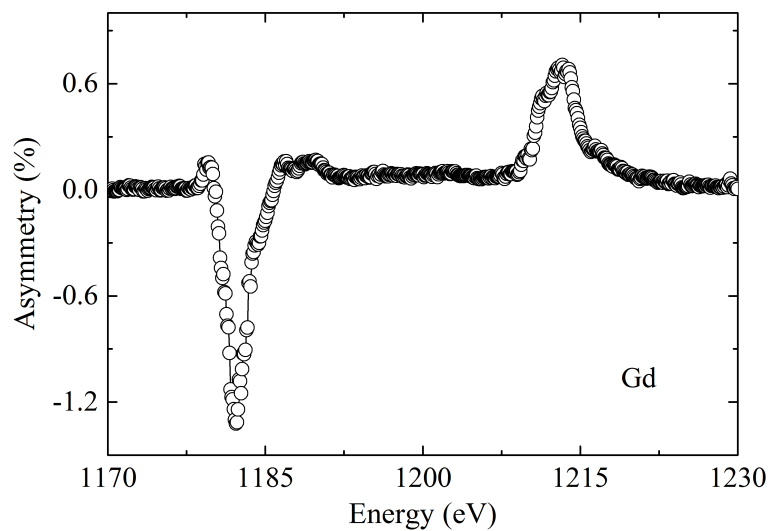


Figure C.8.: Asymmetry in XMCD spectrum of Gd at M_4 and M_5 edge. Asymmetry caused by difference between right and left circular polarized light as function of X-ray energy. Measurement temperature $T = 222.5$ K.

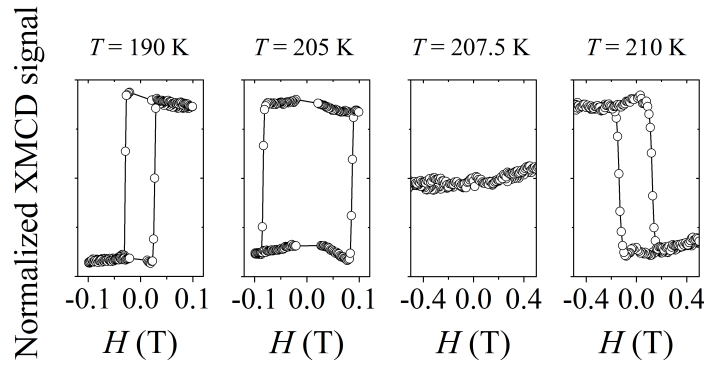


Figure C.9.: Temperature dependent hysteresis loops of Gd measured by XMCD. Normalized signal of XMCD asymmetry at of M_5 edge.

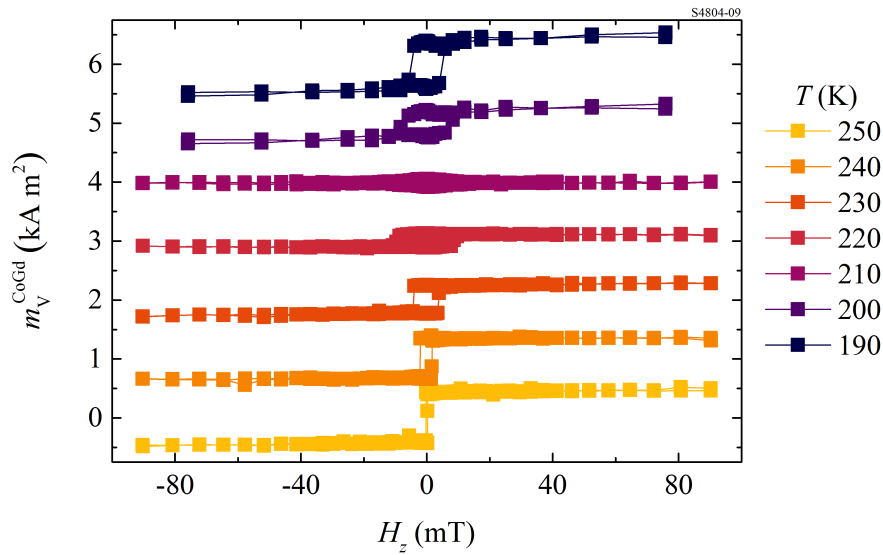


Figure C.10.: Out-of-plane hysteresis loops of ferrimagnetic Co/Gd sample measured by SQUID. Net magnetic moment of Co/Gd sample m_V^{CoGd} . The index V shall indicate that measured magnetic moment is not divided by the volume of sample piece. Loops shifted by 1 kA m^2 each. Baseline for $T = 250 \text{ K}$ curve.

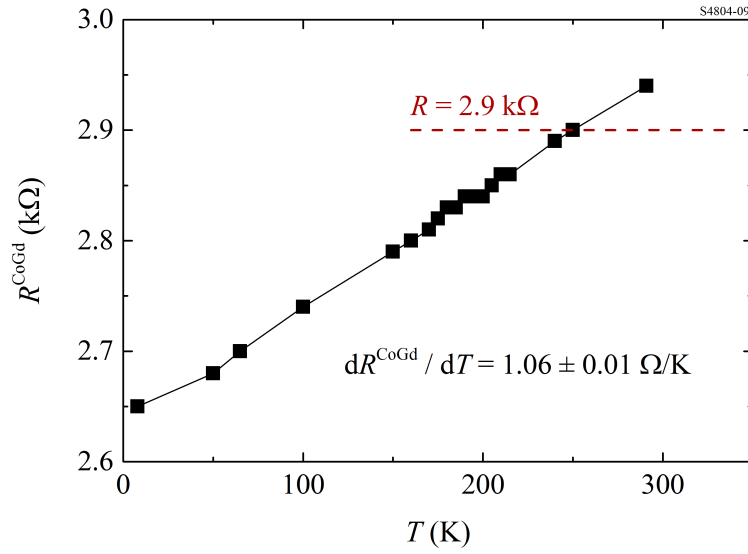


Figure C.11.: Resistance of device of ferrimagnetic sample. Dashed red line indicates regime in which DW velocity was measured when heating is taken into account (from 160 K to 340 K). Resistance of 2.9 kΩ is in middle of this temperature range. For simplicity temperature is assumed to be constant within this measurement range.

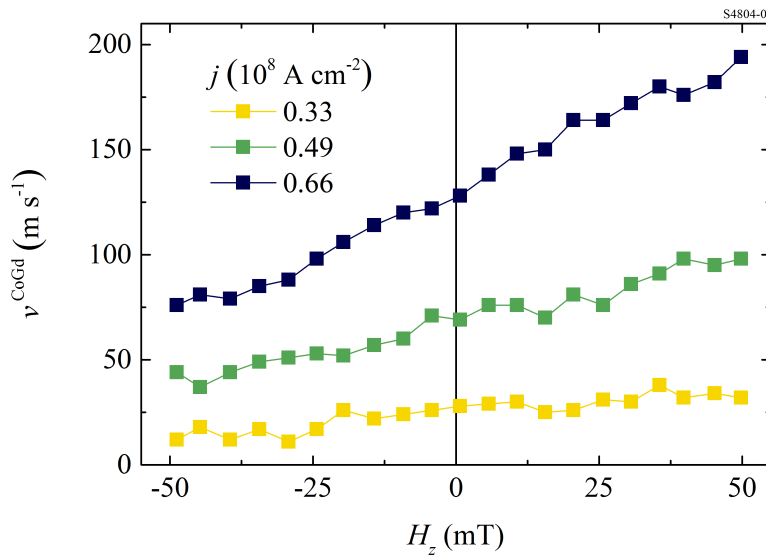


Figure C.12.: Domain velocity dependence of H_z at magnetic moment compensation temperature using current pulses. Cryostat temperature set to T_M so that DW would not move by H_z . Pulses of different pulse strength were applied and DW displacement measured after pulse. Increasing dependence of DW velocity v^{CoGd} on H_z as current density increases. Can be explained by increasing JOULE heating with increasing j .

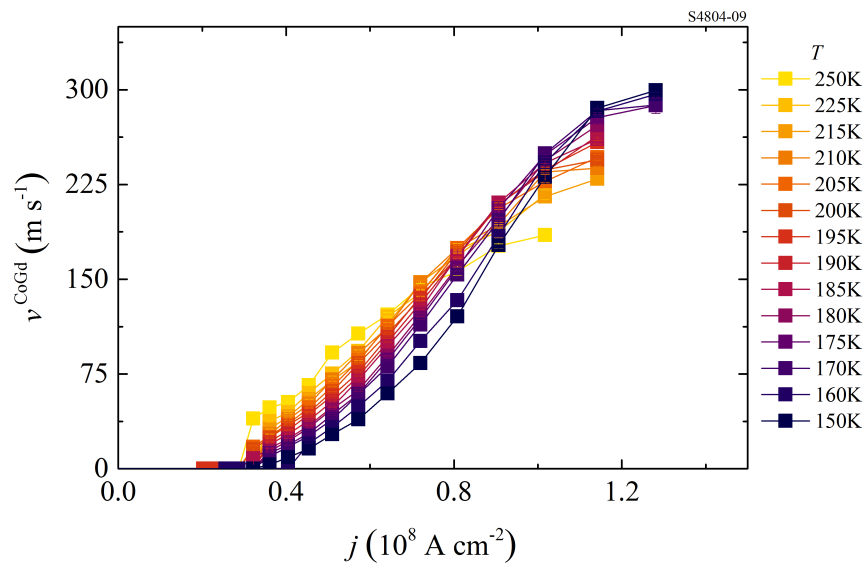


Figure C.13.: Domain wall velocity in ferrimagnetic Co/Gd bi-layer as a function of current density at various cryostat temperatures. Constant resistance of $2.9 \text{ k}\Omega$ is assumed.

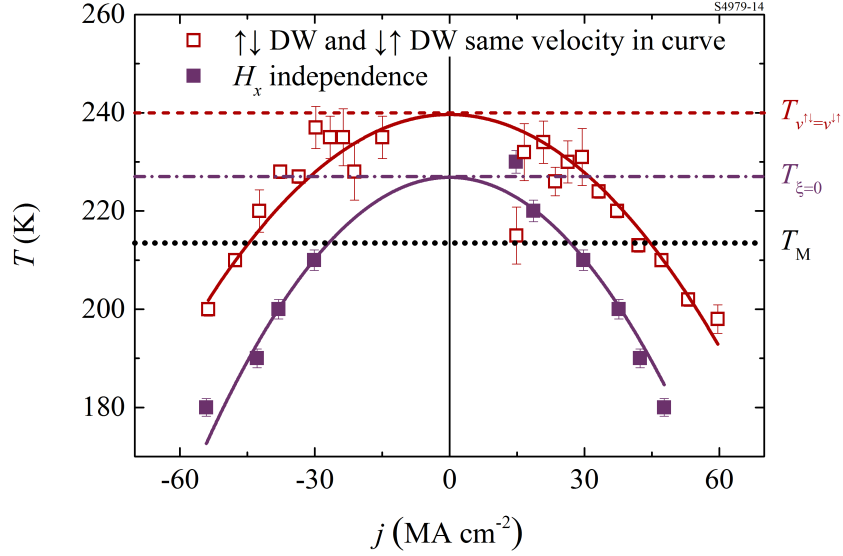


Figure C.14.: Temperature at which $\uparrow\downarrow$ and $\downarrow\uparrow$ DWs move with same velocity in curved wire. Note that the sample is different to the sample presented in the main part. Although the layer thicknesses were supposed to be the same, there might be slight differences in the thicknesses, leading to slightly distinct temperatures of T_M and T_A . Cryostat temperature $T_{v^{\uparrow\downarrow} = v^{\downarrow\uparrow}}(0) = (239 \pm 2)$ K at which $\uparrow\downarrow$ and $\downarrow\uparrow$ DWs move with same velocity in curved wire in the limit of $j \rightarrow 0$. Cryostat temperature $T_{\xi=0}(0) = (226 \pm 3)$ K at which DW velocity shows no dependence on H_x . Magnetic moment compensation temperature $T_M = (213.5 \pm 0.1)$ K at which DW cannot be moved by any H_z field. All temperatures obtained by fitting the data. 100 ns-long pulses used. Wire width: 3 μm . Inner device radius: 10 μm . Sample structure: Si(ox) / 10 Al_2O_3 / 2 TaN / 3 Pt / 0.5 Co / 1.8 Gd / 5 TaN (unit: nm).

Eidesstattliche Erklärung

Ich, Robin Bläsing, erkläre an Eides statt, dass ich die Arbeit selbstständig und ohne fremde Hilfe verfasst, keine anderen als die von mir angegebenen Quellen und Hilfsmittel benutzt und die den benutzten Werken wörtlich oder inhaltlich entnommenen Stellen als solche kenntlich gemacht habe.

Halle (Saale), den 15.08.2019
(Robin Bläsing)

Academic curriculum vitae

Robin Bläsing, M. Sc, M. Sc.

Gustav-Adolf-Straße 47A

04105 Leipzig

Date of birth: January 9th, 1990

Place of birth: Haan, Germany

Gender: Male

Nationality: German

Education

- 10/2015 - 12/2019 **PhD student at Martin Luther University of Halle-Wittenberg and research assistant at Max Planck Institute of Microstructure Physics, Halle (Saale), Germany**
PhD thesis: *Highly efficient domain wall motion in ferrimagnetic bi-layer system at angular momentum compensation temperature*
- 04/2013 – 09/2015 **Master of Science in Management, Business and Economics at RWTH Aachen University, Germany**
Master's thesis: *Solvency-II-Standardformel und Insolvenzrisiken von Versicherungsunternehmen - Eine kritische Analyse*
- 04/2013 – 11/2014 **Master of Science in Physics at RWTH Aachen University, Germany**
Master's thesis **in cooperation with IBM Almaden Research Center in San Jose, California, USA:** *Effect of novel exchange-coupling torque and spin-orbit interaction on current-induced domain wall motion in magnetic nanowires*
- 08/2011 – 01/2012 **Erasmus semester at KTH Stockholm, Sweden**
- 10/2009 – 03/2013 **Bachelor of Science in Physics at RWTH Aachen University, Germany**
Bachelor's thesis: *Drift und Diffusion optisch angeregter Spins in elektrischen Feldern in n-GaAs*
- 08/2000 – 06/2009 **Abitur at Helmholtz Gymnasium in Hilden, Germany**

Halle (Saale), den 15.08.2019

(Robin Bläsing)

Publications and conference contributions

Publications

R. Bläsing, T. Ma, S.-H. Yang, C. Garg, F. K. Dejene, A. T. N'Diaye, G. Chen, K. Liu, and S. S. P. Parkin. Exchange coupling torque in ferrimagnetic Co/Gd bilayer maximized near angular momentum compensation temperature. *Nature Communications*, 9(1):4984, 2018.

A. A. Khan, F. Hameed, R. Bläsing, S. S. P. Parkin, and J. Castrillon. RTSim: A cycle-accurate simulator for racetrack memories. *IEEE Computer Architecture Letters*, 18(1):43–46, 2019.

A. A. Khan, F. Hameed, R. Bläsing, S. S. P. Parkin, and J. Castrillon. ShiftsReduce: Minimizing shifts in Racetrack Memory 4.0. *arXiv preprint arXiv:1903.03597*, 2019.

Conference contributions

R. Bläsing, S.-H. Yang, G. Güntherodt, and S. S. P. Parkin. Effect of novel exchange-coupling torque and spin-orbit interaction on current induced domain wall motion in magnetic nanowires. *DPG-Frühjahrstagung der Sektion Kondensierte Materie*, 2016.

R. Bläsing, T. Ma, C. Garg, T. Lichtenberg, S.-H. Yang, I. Kostanovskiy, and S. S. P. Parkin. Efficient current induced motion of chiral domain walls. *DPG-Frühjahrstagung der Sektion Kondensierte Materie*, 2017

R. Bläsing, T. Ma, S.-H. Yang, C. Garg, and S. S. P. Parkin. Exchange coupling torque in antiferromagnetically coupled Co/Gd bi-layer system. *DPG-Frühjahrstagung der Sektion Kondensierte Materie*, 2018

R. Bläsing, T. Ma, S.-H. Yang, C. Garg, and S. S. P. Parkin. Exchange coupling torque in antiferromagnetically coupled Co/Gd bi-layer system. *Joint European Magnetic Symposia*, 2018